Mixing in buoyancy-driven exchange flows

Tjipto Prastowo

A thesis submitted for the degree of
Doctor of Philosophy
of The Australian National University.

Research School of Earth Sciences

20 January 2008

Except where otherwise indicated in the text,
the research described in this thesis
is my own original work.

Tjipto Prastowo
January 20, 2008

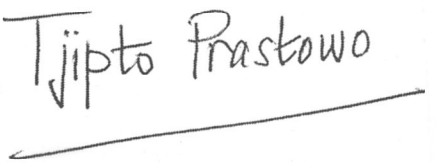

Acknowledgements

My best sincere thanks first go to my supervisor Ross Griffiths and co-supervisor Graham Hughes for their endless patience throughout the project. In particular, their invaluable time and generous guidance have helped me to understand the topics under investigation and the techniques required for academic writing. Without their best support, I would have never been able to get this far. I also would like to thank Andy Hogg for his valuable contributions to this work. His frequent help in the light of personal character and care, particularly during my hard times when I am blue and idle, is really appreciated and unforgettable. The laboratory work in this thesis would not have been possible without the assistance of Tony Beasley. Brad Ferguson has been keen to help and to introduce imaging techniques for documenting experiments and creating clips for practical purposes. Thanks also to Andrew Kiss for his thesis style, as well as for his greetings to have a break for either tea or lunch. This work has also benefited greatly from the Australian Government through the AusAID Scholarship and from Research School of Earth Sciences, the ANU for the necessary funding available for the work to be completed.

The GFD group members have helped to provide a stimulating and amusing environment. In particular, Ross Kerr and Melissa Coman for being good partners in tutoring and preparing laboratory experiments for the ANU third year students. Melissa provides helpful guidance on cultural issues and is great for her effort in trying to understand the difficulties international students face. Melanie O'Byrne is also great for her constant, warm greetings – just to make sure that I am still fine. A good relationship with Kial Stewart has also been built during night hours in the laboratory and the office. Thanks to Marty for friendshipness at this final stage.

Thanks also to many of the staff at the RSES ANU for the helpful assistance and hospitality, as well as to those at the Physics Department ANU and in PEMS-ADFA, the UNSW. Andreea Papuc is remembered as a nice student – make herself ready to help others. Sean O'Byrne is welcomed for his encouragement. Stewart Turner is much appreciated for his kindness to give his best book. Thanks to all friends: Kang Farzan, Teguh, Agung, Agus, Della, Sangeetha, Yin Lu, Lou Chen and others, with whom I share knowledge, good and bad times, and owe some kindness but are not printed here.

Thanks to God for his never-ending blessing to keep me alive to complete the work despite difficulties in some circumstances. Last but not least, a huge thankyou to my parents for their best effort and love, for which I am present and a special one goes to my beloved wife, Nila Kusnul Khotimah for her constant support. Hope this is not the end of my long journey – just thought as the beginning...

Abstract

This thesis presents laboratory work on mixing in buoyancy-driven exchange flows through a constriction that connects two large reservoirs of water with differing densities. In this thesis we focus on exchange flows past a topographic constriction that consists of either a lateral contraction or both a lateral contraction and a bottom sill. The turbulent breakdown of Kelvin-Helmholtz (KH) billows at the sheared density interface within the constriction is the primary mechanism of localised mixing. It is likely that similar mixing processes also occur in density-driven exchange flows through straits or over sills between neighbouring ocean basins, between marginal seas and the open ocean, and in estuaries. It has been suggested that these flows may account for substantial amounts of deep mixing in the oceans. The mixing is, in turn, of potential significance for the global ocean circulation. Thus an understanding of the rates of turbulent mixing in stratified shear flows is important.

The specific aim of the thesis is to determine the bulk (space and time averaged) mixing efficiency in hydraulically-controlled, steady exchange flows. Previous work on mixing in stratified fluids suggests that there is no unique value of mixing efficiency (Linden, 1979), but that there is an upper bound for the mixing efficiency of approximately 0.2 for steady stratified turbulence (Osborn, 1980). It has since been a common assumption that 20% of the total turbulent kinetic energy in the abyssal oceans goes into irreversible vertical mixing, which tends to add to the potential energy stored in the density field of the oceans.

In the case of flows through lateral contractions or over a weir in a constriction the overall mixing efficiency is found to be $11 \pm 1\%$ for sufficiently high Reynolds numbers, independent of flow aspect ratio and channel geometry. For a triangular sill case the measured bulk efficiency is found to be 8% at high Re, independent of the parameters used. These results are consistent with an upper bound prediction for the mixing efficiency of 12.5%, based on a scaling analysis developed for two-layer steady exchange flows with an interfacial mixing layer. Smaller mixing efficiencies are observed in experiments with relatively low Re, owing to intermittent turbulence and relatively greater viscous dissipation. The results for the asymptotic behaviour at large Re flows are relevant to ocean strait flows. Our results, along with the results from some previous studies, raise the possibility that the average mixing efficiency in the oceans may be of the order of one half of that previously proposed.

In this thesis we have also examined the effects of mixing on the exchange transport. Unlike the mixing efficiency, the exchange mass transport is dependent on the channel shape. For the short constrictions the mass transport is, owing to mixing and friction, reduced to 82% of the maximal hydraulic solution, independent of the external parameters. This measurement is in good agreement with the laboratory

measurements of Helfrich (1995). This result is also consistent with the theoretical prediction presented here for the upper bound on the mass transport which, in the absence of friction, is 83% of the maximum transport based on hydraulic theory. In other geometries with a long constriction the transport is less than in the short constriction cases, owing to the presence of two hydraulic exit control points and the influence of both mixing and friction.

Finally, for completeness and comparison, we examine the bulk mixing efficiency in lock-release exchange flows in a simple uniform channel with no hydraulic control points. In this case the flow is inherently unsteady and much of the mixing occurs behind the gravity current heads. Efficiencies range from 5% to 13% but we do not find an asymptotic reach at large Reynolds numbers. This result remains to be fully understood.

Contents

List of Figures

List of Tables

Chapter 1

Introduction

1.1 Motivation

Natural flows in geophysical environments are usually turbulent. The source of the turbulence in a stratified flow can be attributed to a variety of mechanisms; two common examples are shear instability and breaking of internal gravity waves. Shear instability extracts kinetic energy from the mean shear and converts it into smaller scales, while internal gravity waves may carry energy over large distances before breaking. Both of these mechanisms result in small-scale turbulence, which in turn generates vertical mixing and redistribution of density.

The role played by turbulent mixing is of great importance in geophysical flows. For example, mixing in the atmosphere influences the global distributions of heat and water vapour, or the spreading of air pollutants. Mixing in the oceans governs the stratification of the deep ocean, and thereby feeds back into the large-scale circulation. Thus there is a need for a good understanding of mixing in stratified, turbulent shear flows, including determination of mechanisms responsible for the mixing. Theoretical, numerical, laboratory and field studies have all contributed to understanding such mechanisms. However, despite major advances in this topic, there remains considerable uncertainty.

In this thesis we examine a specific class of flows of fundamental interest in which turbulent mixing occurs, namely buoyancy-driven exchange flows. In this type of flow the geometry of the boundaries, or topography, is important as it can serve as a hydraulic control that leads to a long-lived exchange, or shear, flow. As a result, shear-induced mixing occurs in the flow, resulting in changes in the density structure of the water in the reservoirs. This hydraulically controlled flow is also of substantial interest because it controls flows between abyssal ocean basins and through upper ocean straits. Indeed, strait and sill flows are very common features in the oceans

at all depths and geographic locations. Buoyancy-driven exchange and mixing can also occur at the mouth of an estuary (e.g., Stommel & Farmer, 1953), where the exchange is between inflowing sea water and outflowing river water. This process maintains the properties of water masses (e.g., temperature and salinity distributions, dissolved gases and nutrients). Mixing also plays a role in the exchange of air through openings in buildings, such as doorways and windows (Dalziel & Lane-Serff, 1991). Temperature differences across such openings generally drive air circulation between internal spaces and the outside environment, and between rooms within buildings. These openings can serve to naturally ventilate the buildings (Linden, 1999; Hunt & Linden, 1999; Lin & Linden, 2002) and have several advantages compared with air-conditioned buildings, such as reducing additional costs for energy consumption and maintenance of equipment.

Thus mixing in shear flows is an important process in many geophysical situations and engineering applications. It is therefore essential to parameterise mixing and relate it to the large-scale flow in the oceans. In the next section we will discuss some aspects of mixing in the oceans, describing the importance of turbulent mixing in stably-stratified oceans.

1.2 Mixing in the oceans

Vertical mixing assists in maintaining the ocean stratification in the face of broad upward displacement of water by the localised downwelling of dense currents (Munk & Wunsch, 1998). This mixing will be distributed throughout the ocean depth and will be confined in regions close to the ocean boundaries (i.e., bottom and side boundaries). The rate at which this mixing occurs in the oceans (parameterised as a vertical eddy diffusivity), as well as the amount of energy required for this purpose, has been inferred in numerous studies. For example, a proposed balance between the upwelling of relatively dense, cold, bottom waters and the downward turbulent mixing of heat requires a rate of vertical mixing of $\sim 10^{-4}$ $m^2 s^{-1}$ (Munk, 1966; Munk & Wunsch, 1998), and a relatively large amount of mechanical energy of ~ 2 TW is required to support this mixing rate (Munk & Wunsch, 1998; Wunsch, 2002; Wunsch & Ferrari, 2004). This predicted mixing rate is in agreement with direct measurements of a vertical eddy diffusivity at various sites (Hogg *et al.*, 1982; Whitehead & Worthington, 1982; Ganachaud & Wunsch, 2000). These field studies found a typical value in the range $1 - 5 \times 10^{-4}$ $m^2 s^{-1}$ for the vertical diffusivity. However, dissipation and tracer measurements in the ocean interior (Gregg, 1989; Ledwell *et al.*, 1993; Kunze & Sanford, 1996; Ledwell *et al.*, 1998) measured a value

of $\sim 10^{-5}$ $m^2 s^{-1}$ for the vertical diffusivity, an order of magnitude smaller than the previously proposed value. It is interesting to note that enhanced mixing over rough topography (Polzin *et al.*, 1997; Ledwell *et al.*, 2000) was observed in the deep ocean. As a result of intense turbulence, a greater value of the vertical diffusivity (up to 10^{-3} $m^2 s^{-1}$) was found in this region.

A common oceanographic assumption is that about 20% of the energy supply is transferred into stratified turbulence through mixing (Munk & Wunsch, 1998; Webb & Suginohara, 2001; Wunsch & Ferrari, 2004). This assumption is widely referred to as the average efficiency of mixing, which is the proportion of turbulent kinetic energy supply used to irreversibly increase potential energy stored in the density distribution of the oceans. Whether the efficiency of this mixing has a 'canonical' value of ~ 0.2 derived for stratified shear flows remains the subject of continuing debate. This value is obtained by assuming that steady turbulence is maintained by the growth and decay of Kelvin-Helmholtz instability generated in a shear flow (Osborn, 1980), where the time-averaged flux Richardson number is taken to be at its critical value of 0.15 (Ellison, 1957), above which the turbulence cannot be sustained.

Because of its importance, mixing efficiency in the oceans has been estimated through field observations (Gargett & Moum, 1995; Moum, 1996; Ruddick *et al.*, 1997). Other studies using laboratory experiments (Thorpe, 1973; Linden, 1980; McEwan, 1983; Park *et al.*, 1994; Holford & Linden, 1999; Monti *et al.*, 2007) and numerical simulations (Caulfield & Peltier, 2000; Staquet, 2000; Peltier & Caulfield, 2003) have also examined some aspects of mixing in stratified fluids. The results from these studies suggested that the mixing efficiency is not unique, but is likely to depend on various factors, including the strength of background stratification and the nature of turbulence. The detail of the laboratory experiments on mixing is reviewed in §2.1, with discussion on types of experimental measurements and on various definitions of mixing efficiency used.

There have been no previous measurements of the amount of turbulent mixing in exchange flows. The amount of this mixing is, however, needed to understand the rate of production of mixed water or the global contribution of these flows to vertical mixing. The observed shear instability in buoyancy-driven exchange flows may also provide insights into the dynamics of the mixing relevant to other forms of unstable shear flows. Hence, it is of fundamental interest to parameterise mixing in such flows. In the next section we will describe exchange flows in the oceans, featuring a wide variety of examples of such flows in many geophysical situations, as well as in engineering applications.

1.3 Oceanic exchange flows

Exchange flows through topographic constrictions that connect two bodies of water with different densities occur in many geophysical situations. Such constrictions include straits and sills, and affect both upper ocean and abyssal exchange flows. These flows are generally driven by density differences between marginal seas and the oceans, within estuaries (Stommel & Farmer, 1953; Grigg & Ivey, 1997) and between water masses in the deep oceans (Whitehead, 1998; Bryden & Nurser, 2003). A well-known example of these flows is the exchange between the Mediterranean Sea and the North Atlantic Ocean that takes place through the Strait of Gibraltar (Armi & Farmer, 1987; Bray *et al.*, 1995; Tsimplis & Bryden, 2000). Due to net evaporation in the Mediterranean, there exists a horizontal density contrast with the North Atlantic that drives the exchange of water through the Strait of Gibraltar. Dense, warm salty water flows out of the sea at depth, and is replaced by relatively cool, fresh surface water from the ocean.

Other examples of density-driven exchange flow include the exchange through the Bosphorus (Oğuz *et al.*, 1990; Gregg *et al.*, 1999; Gregg & Özsoy, 2002; Oğuz, 2005) and the Bab el Mandab (Pratt *et al.*, 1999; Smeed, 2000; Smeed, 2004). In the Bosphorus the flow runs approximately north-south, connecting the Black Sea in the north to the Sea of Marmara in the south. With two sills near its ends and a contraction in the middle the flow in the Bosphorus is characterised by relatively fresh, surface water flowing southward and salty, dense water counter-flowing northward. In the Bab el Mandab the exchange occurs between the Red Sea and the Persian Gulf, and has outflows over shallow sills. Unlike the Gibraltar and the Bosphorus, the Bab el Mandab is strongly affected by seasonal variation of the local winds (Murray & John, 1997), which leads to different circulations in the strait between winter and summer times (Smeed, 2000, 2004).

The flows in the Bosphorus and in the Bab el Mandab described above are primarily buoyancy-driven and lead to baroclinic exchange. However, exchange flow between ocean waters can also be strongly influenced by barotropic effects. One example of such a situation is the Indonesian Throughflow (ITF), which carries heat and water from the warm surface waters of the western Pacific Ocean to the Indian Ocean through a series of narrow straits in the Indonesian Archipelago. This transport of water is mainly carried by the upper layer of the eastern Indonesian seas (e.g., Vranes *et al.*, 2002). However, water properties in the Indonesian seas indicate an important contribution from the deeper layer. Enhanced vertical mixing is possible owing to the complex bathymetry of the seas with numerous sills encoun-

tered at greater depths (Gordon *et al.*, 2003). Dense water overflowing sills into the depth of a confined basin displaces the resident water upward. Thus the density-driven overflow is compensated by upwelling within the basin, bringing relatively cold, deep, nutrient-rich waters up to the surface. Such a local circulation between deep overflows and upwelling processes maintain the properties of the confined water masses in the local region, implying a biological balance between the upper layer and deeper waters.

In other regions of the oceans, such as the abyss, water masses tend to fill up deep basins and then flow through a large number of narrow gaps in sea-floor mountain ranges (e.g., mid-ocean ridges) or over sills. For example, the Denmark Strait and Faroe Ridge (Dickson & Brown, 1994; Duncan *et al.*, 2003) separate the deep waters of the Norwegian Sea from those in the North Atlantic. Another example of deep flow is the transport of bottom waters through the Vema Channel (Hogg *et al.*, 1982; McDonagh *et al.*, 2002) in the South Atlantic, where Antartic Bottom Water (AABW) flows northward from the Argentine Basin to the Brazilian Basin.

Exchange flows are also common in man-made structures, such as a canal connecting two bodies of water with different salinities or temperatures. During summer periods the temperature difference between warmer water of Hamilton Harbour and cooler water of Lake Ontario drives the exchange through the Burlington Ship Canal (Greco, 1998; Tedford, 1999; Gu, 2001). In buildings, the exchange of warm and cold air through openings may also occur (Dalziel & Lane-Serff, 1991).

1.4 Models of exchange flows

Buoyancy forces associated with a density difference between two water masses will drive horizontal exchange. When the flow encounters geometrical changes in either width or depth, the flow will accelerate. Topographical constrictions such as straits and sills in the oceans cause locally increased flow speeds. Locations where the speeds become critical are called hydraulic control points. These are common in geophysical exchange flows. The flow is then hydraulically controlled in the sense that the rate of water exchange through the strait or over the sill is limited by a critical flow condition in the constriction (Armi, 1986; Lawrence, 1990; Dalziel, 1991). Note that the dynamics of exchange flows, along with the concept of hydraulic control, is reviewed in detail in Chapter 2. Many oceanic exchange flows between two adjacent ocean basins may be hydraulically controlled at one or two control points (e.g., Farmer & Armi, 1986; Armi & Farmer, 1988; Smeed, 2004). These are the 'choke points' that control the global circulation of ocean waters (Bryden &

Stommel, 1984; Pratt & Lundberg, 1991; Dickson & Brown, 1994) and the exchanges between estuaries or coastal seas and the open ocean (Stommel & Farmer, 1953).

Transport of water between ocean basins may also occur in situations where hydraulic control is absent. This is associated with the propagation of gravity currents, much as in cases with hydraulic control, but in the absence of the control. The exchange will be more rapid and in practice will tend to remove the lateral density difference. Hence, it will generally be an unsteady and short-lived flow.

The basic theory for a gravity current was first proposed by Benjamin (1968), who used a two-layer flow with no mixing and no energy dissipation to model the gravity current. Laboratory experiments (Hallworth *et al.*, 1993; García & Parsons, 1996; Hacker *et al.*, 1996) have also examined some aspects of the small-scale mixing processes between the current and the surrounding fluid. Hallworth *et al.* (1993) and Hacker *et al.* (1996) considered the rate of dilution of a gravity current 'head' as it propagates in a horizontal surface and is continuously fed by buoyant fluid from its source region. García & Parsons (1996) examined mixing at the front of a gravity current using a specifically designed tank for 'freezing' the front and found mixing rates to be dependent upon experimental conditions. Gravity currents are important in many practical applications. For example, in oceanography it may be important to know how propagating gravity currents transport sediment (García & Parsons, 1996), and distribute fluid properties, such as salt (or heat), between parts of the ocean. Other examples include front formation at the mouth of an estuary (Wang, 1984) and at the inlet between a river and a lake. The formation of fronts in such systems may cause environmental problems as pollutant may be carried by the discharge of river water into the coastal ocean (Munchow & Garvine, 1993), or to a greater depth of the lake.

In this thesis we consider the dynamics of exchange flow processes in the oceans using an approach of laboratory work. In particular, we investigate the nature of turbulent mixing that occurs in laboratory experiments, along with the effects of mixing on the rate of exchange. A general overview of the thesis including synopsis of each chapter is given in the next section.

1.5 Overview

The primary aim of the thesis is to quantify the overall amount of mixing in the buoyancy-driven exchange flows, hence to determine the bulk efficiency of mixing. In the process we also examine the effects of mixing on the rates of exchange. Scaling arguments are developed to describe the flow and these are an important step in

applying the experimental results to a range of specific ocean strait flows.

The laboratory experiments conducted in this thesis focus on exchange flows through topographic constrictions that connect two large reservoirs of water. The topographic constrictions include a pure contraction in width and a constriction with a bottom sill. We present a new approach that involves measurements of the change in potential energy, hence the amount of turbulent mixing, in the exchange flows. The measurements are used to determine the bulk efficiency of mixing and the effects of the mixing on the mass transport through the constricted channel. For comparison we report similar measurements for flows without hydraulic control, which we refer to as 'gravity current' experiments.

This thesis is structured as follows. Chapter 2 reviews previous work of direct relevance. The concept of mixing efficiency in a stratified shear flow is introduced. Of particular interest is the equivalence between the definition of the mixing efficiency used here and that used by other authors. We then present internal hydraulic theory, which serves as a useful tool for modeling two-layer exchange flows. The application of this theory in predicting the maximal transport through the channel is discussed in the context of a two-layer approximation. Mixing produced by lock-release gravity currents in a horizontal channel of uniform width and depth is also described.

Chapter 3 presents the methods used in the experiments. These include the laboratory apparatus and procedure for all experiments conducted and the measurement techniques developed. Details of each type of experiment and the external parameters that govern the dynamics of the flow are also introduced. Chapter 4 constructs a theoretical framework that will be used to analyse and interpret experimental results. This framework allows the calculation of mass transport and mixing efficiency. We also present a scaling theory that leads to a prediction for the mixing efficiency and the mass transport in controlled exchange flows.

Chapters 5-7 report all results of the laboratory experiments. In Chapter 5 we examine the results for exchange flows through a constriction. In Chapter 6 the results are presented for exchange flows over a sill. In Chapter 7 we present the results for the contrasting case of lock-release gravity currents in a channel of uniform width and depth, hence without hydraulic control.

In Chapter 8 the results are reviewed in the context of previous works on turbulent mixing or hydraulically controlled exchange flows, and possible applications of the results to oceanic strait flows are discussed. The main conclusions of the thesis and suggestions for future work are then summarised in Chapter 9.

Chapter 2

Background

In §2.1 we discuss mixing in stratified shear flows, starting from a fundamental understanding of mixing processes and ending with the discussion of various definitions of mixing efficiency currently used. In §2.2 we present internal hydraulic theory, including the application of this theory to the problem of two-layer exchange flows and its limitations in oceanic flows. Maximal exchange and the role of mixing in reducing the transport in hydraulically controlled exchange flows are introduced in §2.3. Mixing produced by lock-release gravity currents in a uniform channel is described in §2.4.

2.1 Mixing in stratified shear flows

Because mixing processes in stratified shear flows involve exchange of energy between potential and kinetic forms, then it is necessary to understand mechanisms that are responsible for transfer of these energies from one form to another. We begin with a fundamental understanding of how potential energy is divided into 'background' and 'available' components in a two-fluid system (see Winters *et al.*, 1995, for a comprehensive discussion). The background potential energy state is the minimum potential energy state that would be attained by allowing the fluid to redistribute, without mixing, until there is no further motion. The potential energy of the fluid in any other state can be calculated relative to this reference state. If mixing occurs in the system, work is done against buoyancy forces (Cushman-Roisin, 1994, ch.11) and the potential energy is irreversibly increased (Caulfield & Peltier, 2000; Peltier & Caulfield, 2003), with an equivalent loss of turbulent kinetic energy (Carpenter *et al.*, 2007; Smyth *et al.*, 2007). Turbulent kinetic energy is also dissipated by viscosity, and the fraction of the loss that goes into mixing is referred to as 'mixing efficiency'.

The source of the turbulent kinetic energy may be 'external' or 'internal' (see Turner, 1973, ch.4, 5, 9 and 10 for further details). External sources include mechanical devices, such as an oscillating or falling grid, as was used to examine mixing in a stratified fluid with zero mean shear (Linden, 1980; Park *et al.*, 1994; Redondo *et al.*, 1996; Holford & Linden, 1999). In these cases the energy transformation and mixing efficiency are determined by estimating either the energy input, or measuring the turbulent kinetic energy from turbulent flow characteristics, and measuring the change in the density distribution. Mixing due to externally driven turbulence is referred to as external mixing.

However, in laboratory shear flows sources of turbulence are shear instabilities formed at the interface between two miscible fluids. Mixing associated with these sources is referred to as internal mixing (Thorpe, 1968, 1973; Koop & Browand, 1979; McEwan, 1983; Monti *et al.*, 2007). Using a tilted tank, Thorpe (1968, 1973) pioneered laboratory experiments on this type of mixing and observed the growth and decay of two-dimensional billows induced by Kelvin-Helmholtz (KH) instability at the interface between the layers. Koop & Browand (1979) examined this mixing by measuring the thicknesses of an interfacial mixed layer, and found that the dimensionless layer thickness is approximately 0.3 (further described in §4.4). Using the same experimental set-up as was used by Thorpe (1973), Monti *et al.* (2007) were able to reproduce and examine the evolution of KH billows at different stages. They considered the flux Richardson number (defined below) as a measure of the mixing efficiency and found that at late times 'this efficiency' is approximately constant in time, and independent of initial flow conditions.

This thesis focuses on mixing in a buoyancy-driven exchange flow – an internal mixing process – where the source of turbulent kinetic energy is the available potential energy released from the density field by the mean flow. This mixing causes an irreversible increase in the background potential energy relative to that in an exchange flow without mixing (see §4.3 for further details). In this type of flow the initial development and maintenance of turbulent overturning motions are due to the shear instability and turbulent breakdown of KH billows (Caulfield & Peltier, 2000; Peltier & Caulfield, 2003; Patterson *et al.*, 2006; Monti *et al.*, 2007). The amount of turbulent mixing in this flow is determined by the amount of energy supplied to the turbulence and the proportion of that turbulent kinetic energy, which is irreversibly converted into potential energy of the density field.

It is important to note that the mixing considered here corresponds to a flow instability occurring in a stably stratified density field (Fernando, 1991; Fernando & Hunt, 1996; Strang & Fernando, 2001*a*, *b*; Peltier & Caulfield, 2003). This case

is fundamentally different from mixing in a statically unstable density field (Dalziel, 1993; Dalziel *et al.*, 1999), where the primary mechanism for mixing is Rayleigh-Taylor (RT) instability.

Three definitions of the mixing efficiency have been used previously. Two of these definitions are derived from the simplified, steady-state energy balance. This balance is between turbulent kinetic energy production on the one hand, and buoyancy flux owing to mixing and turbulent kinetic energy loss to viscous dissipation on the other hand (Osborn, 1980). In any point of a turbulent field this energy balance (see Appendix A for a detailed derivation) is written as

$$-\overline{u_i'w'}\frac{\partial \overline{u}_i}{\partial z} = \frac{g}{\overline{\rho}}\overline{\rho'w'} + \varepsilon, \tag{2.1}$$

where ρ', u_i' $(i = 1, 2)$ and w' are the fluctuating components of the density, horizontal velocities and vertical velocity, respectively, $\overline{\rho}$ and $\overline{u}_i$ are the time-averaged components of the density and horizontal velocities, respectively, g is acceleration due to gravity and ε is the rate of turbulent dissipation. The full turbulent kinetic energy equation is presented in detail in §A.1.2, and the relative importance of each term in the turbulent kinetic energy from which (2.1) is derived is discussed in §A.2.

One definition of mixing efficiency is directly related to the terms in (2.1). The left-hand side of (2.1) represents the production of turbulent kinetic energy. The terms on the right-hand side of (2.1) are the buoyancy flux and the loss of turbulent kinetic energy to viscous dissipation, respectively. Based on these quantities the flux Richardson number, Ri_f, is defined as the ratio of the buoyancy flux to the turbulent kinetic energy production (Turner, 1973, ch.5; Osborn, 1980; Ivey & Imberger, 1991; Strang & Fernando, 2001*b*),

$$Ri_f = \frac{\frac{g}{\overline{\rho}}\overline{\rho'w'}}{-\overline{u_i'w'}\frac{\partial \overline{u}_i}{\partial z}}. \tag{2.2}$$

If the numerator and denominator in (2.2) can be measured, then the flux Richardson number can be used as a measure of mixing efficiency (Linden, 1980; Osborn, 1980; Ivey & Imberger, 1991; Strang & Fernando, 2001*b*). For the case of a stably stratified density field (with a positive vertical eddy viscosity), both the numerator (buoyancy flux) and denominator (shear production) on the right-hand side of (2.2) are positive, and hence $Ri_f > 0$. In this case the buoyancy flux corresponds to an extraction of turbulent kinetic energy from the mean flow and an irreversible increase in the potential energy of the density field.

The second approach to determining mixing efficiency is based on field observations, where the rate at which mixing occurs is usually parameterised as a vertical

eddy diffusivity for density, κ_ρ. In this approach κ_ρ is written as

$$\kappa_\rho = -\frac{\overline{\rho' w'}}{\partial\overline{\rho}/\partial z}, \tag{2.3}$$

where $\partial\overline{\rho}/\partial z$ is the mean vertical gradient of the density. If the buoyancy frequency N is defined as

$$N = \left(\frac{-g}{\rho_o}\frac{d\overline{\rho}}{dz}\right)^{1/2}, \tag{2.4}$$

then N^2 can be written as

$$N^2 = -\frac{g}{\rho_o}\frac{d\overline{\rho}}{dz}, \tag{2.5}$$

where ρ_o is a reference density. Using (2.5), then (2.3) becomes

$$\kappa_\rho = \frac{g}{\rho_o}\frac{\overline{\rho' w'}}{N^2}. \tag{2.6}$$

Taking the reference density ρ_o to be the mean density $\overline{\rho}$, and substituting (2.2) and (2.6) into (2.1) yields

$$\kappa_\rho \frac{N^2}{Ri_f} = \kappa_\rho N^2 + \varepsilon, \tag{2.7}$$

which can be rearranged (see Osborn, 1980) to become

$$\kappa_\rho = \left(\frac{Ri_f}{1 - Ri_f}\right)\frac{\varepsilon}{N^2} = \Gamma\frac{\varepsilon}{N^2}. \tag{2.8}$$

Thus the vertical eddy diffusivity κ_ρ is related to measurements of the rate of turbulent dissipation ε and the strength of the background stratification N^2. It is clear from (2.8) that

$$\Gamma = \frac{Ri_f}{1 - Ri_f}, \tag{2.9}$$

where Γ here is used as an 'alternative' measure of mixing efficiency. Physically, this definition of mixing efficiency (2.9) represents the ratio of the proportion of total energy used for mixing to the proportion dissipated by viscosity. As viscous dissipation is always present in a flow, then $Ri_f < 1$. Osborn (1980) adopted the theoretical prediction of Ellison (1957) for a critical value of $Ri_f = 0.15$, above which turbulence cannot be sustained in a steady shear flow, and used this value as an upper bound on Ri_f giving an estimate of Γ to be 0.18, being rounded to 0.2. Note that the efficiency frequently used by many ocean modelers is $Ri_f \approx 0.2$ (corresponding to $\Gamma \approx 0.25$), so that 20% of the available energy goes into mixing (Munk & Wunsch, 1998; Webb & Suginohara, 2001; Wunsch & Ferrari, 2004).

In this thesis we use a third definition of the efficiency of mixing in a stably stratified flow. The efficiency of mixing in this method is directly related to the fraction of the turbulent kinetic energy available for mixing. This fraction appears as the change in potential energy that corresponds to an irreversible increase in the potential energy of the density stratification (Caulfield & Peltier, 2000; Peltier & Caulfield, 2003). Thus, the mixing efficiency η is written as

$$\eta = \frac{\Delta P}{\Delta K}, \tag{2.10}$$

where ΔP is the irreversible increase in the potential energy of the density distribution and ΔK is the turbulent kinetic energy supply. As in the first definition (2.2) we again consider the fraction of turbulent kinetic energy that goes into mixing, but this time use the changes in potential and kinetic energies, rather than the turbulent fluxes (see Caulfield & Peltier, 2000; Peltier & Caulfield, 2003). The efficiency η is therefore a time and space average, and a cumulative efficiency.

The definition of mixing efficiency in (2.10) is similar to that discussed by Holford & Linden (1999), although they did not measure the efficiency in a suitable manner for direct comparison. Holford & Linden (1999) used grid-generated turbulence with a rake of bars mounted vertically in a stratified fluid and observed the change in potential energy of the fluid, assuming that the energy input was kinetic energy of the bar. The work of Holford & Linden (1999) is somewhat similar to the laboratory experiments of Park *et al.* (1994). The latter carried out mixing experiments using vertical rods pulled horizontally through a stratified fluid. The resulting mixing was observed and the potential energy change was then measured. In both cases the source of mixing is external, as opposed to our method.

Both Ri_f and η defined in (2.2) and (2.10), respectively, should be equivalent for the efficiency of mixing in a steady shear flow, if the local definition of Ri_f is steady and representative of the spatial average in the flow.

Numerous laboratory experiments on mixing in stratified fluids have been carried out, in which the flux Richardson number Ri_f has been used to estimate mixing efficiency. In general the results of these experiments show a curve shape, implying that there is no unique value for Ri_f, but $Ri_f \leq 0.25$ with shear-induced mixing seems to be the most efficient process (see figure 4 of Linden, 1979). This shape is independent of initial conditions, or types of experiment; whether the source of turbulent kinetic energy is external or internal. Using grid-generated turbulence Linden (1980) demonstrated that Ri_f was a function of the strength of the stratification, measured by the overall Richardson number $Ri_o = g'\mathcal{L}/\mathcal{U}^2$, where $\mathcal{L}$ and

$\mathcal{U}$ are the length and velocity scales in the measurements. The results show two different flow regimes over the range of Ri_o examined. It was found that in the case of weak stratification (regions of low Ri_o) Ri_f increases with Ri_o and eventually reaches a maximum value of 0.12 ± 0.01 at $Ri_o \approx 1.3$. This reflects that as Ri_o increases more energy supply from turbulent kinetic energy is needed to overcome stabilising effects by the stratification. If the stratification is further increased, then Ri_f decreases, suggesting that the turbulence is suppressed by buoyancy forces in strongly stratified fluids. However, little is known about the role played by Reynolds number in characterising Ri_f, or the efficiency of mixing from Linden's (1979, 1980) studies.

Ivey & Imberger (1991) generalised the common definition of Ri_f (2.2) to include all sources of mechanical energy required to maintain the turbulence, for which the net energy is written as E (see §A.2 for details). For mechanically energised turbulence (positive buoyancy fluxes) Ivey & Imberger (1991) found that Ri_f can be parameterised by two dimensionless numbers: the turbulent Froude Fr_T and Reynolds Re_T numbers, defined as

$$Fr_T = \frac{u}{N\lambda} = \left(\frac{\varepsilon}{N^3\lambda^2}\right)^{1/3}, \qquad Re_T = \frac{u\lambda}{\nu} = \frac{\varepsilon^{1/3}\lambda^{4/3}}{\nu}, \tag{2.11}$$

respectively, where u is the rms velocity of the turbulent motions, λ is the lengthscale of the observed overturns and ν is the kinematic viscosity. The above parameters are related to each other by an expression below,

$$Fr_T = \left(\frac{\varepsilon}{Re_T \nu N^2}\right)^{1/2}. \tag{2.12}$$

In the case of shear-generated turbulence induced by the development and breakdown of KH billows $Fr_T \approx 1$ (Ivey & Imberger, 1991) so that (2.12) becomes

$$Re_T \approx \frac{\varepsilon}{\nu N^2}. \tag{2.13}$$

As previously mentioned, Ri_f is a function of Ri_o, hence of the strength of the stratification N^2. This fundamental concept, together with (2.13), provides insight into the relationship between the strength of turbulence as implied by the turbulent Reynolds number Re_T and the mixing efficiency as measured by Ri_f. Using the experimental data of Ivey & Nokes (1989), Ivey & Imberger (1991) showed that Ri_f increases with Re_T, then approaches an asymptotic value of approximately 0.2 for $Re_T > 16$.

There are two important points that can be made from the above investigations. First, the mixing efficiency increases with intensity of turbulence at low Ri_o (weak stratification). Second, the efficiency tends to asymptote to a constant value at high Ri_o (strong stratification). However, none of the above studies relate the mixing efficiency to the Reynolds number of the flow based on external quantities.

2.2 Internal hydraulic theory

This section reviews previous work on the hydraulics of two-layer exchange flows past through a topographical constriction. These flows have been examined because they are of fundamental interest in fluid mechanics and engineering, and because straits and sills control flows between neighbouring parts of the oceans. They are of additional interest in this thesis because they can serve as a steady shear flow in which turbulent mixing can be examined.

The importance of such flows was studied by Stommel & Farmer (1953), who examined hydraulically controlled two-layer flows in an estuary. In this context, the flow is characterised by conditions at hydraulic control points, defined as positions in the flow where the speed of long internal waves is zero (Dalziel, 1991; described later in details in this section). Once these control points are determined in the flow, a global solution for the flow field can be obtained (Armi, 1986). It was found that the hydraulic transition at the mouth of the estuary serves as a 'constriction' to limit the maximum possible transport that may occur between the estuary and the open ocean.

Hydraulic control can be studied in a systematic way using laboratory experiments on two-layer flows. Wood (1970) and Lawrence (1990) examined two-layer exchange flows through a contraction connecting two reservoirs of water with different densities, and demonstrated the possibility of two hydraulic control points in the flow, namely a topographic control at the minimum width of the contraction, and a second, 'virtual' control away from the contraction minimum width. Between these two control points there is a region in which the flow is subcritical; outside this region, the flow is supercritical.

The role of topographic and virtual controls can be clarified using Armi's (1986) graphical method in the Froude-number plane. This technique, developed for exchange flows through channels of slowly varying width and depth, illustrates concepts of hydraulic control points and maximal exchange. Two counter-flowing fluid layers are assumed to be homogeneous, inviscid and immiscible, having constant density and velocity for each layer, as shown in Figure 2.1(b, c). Armi (1986) de-

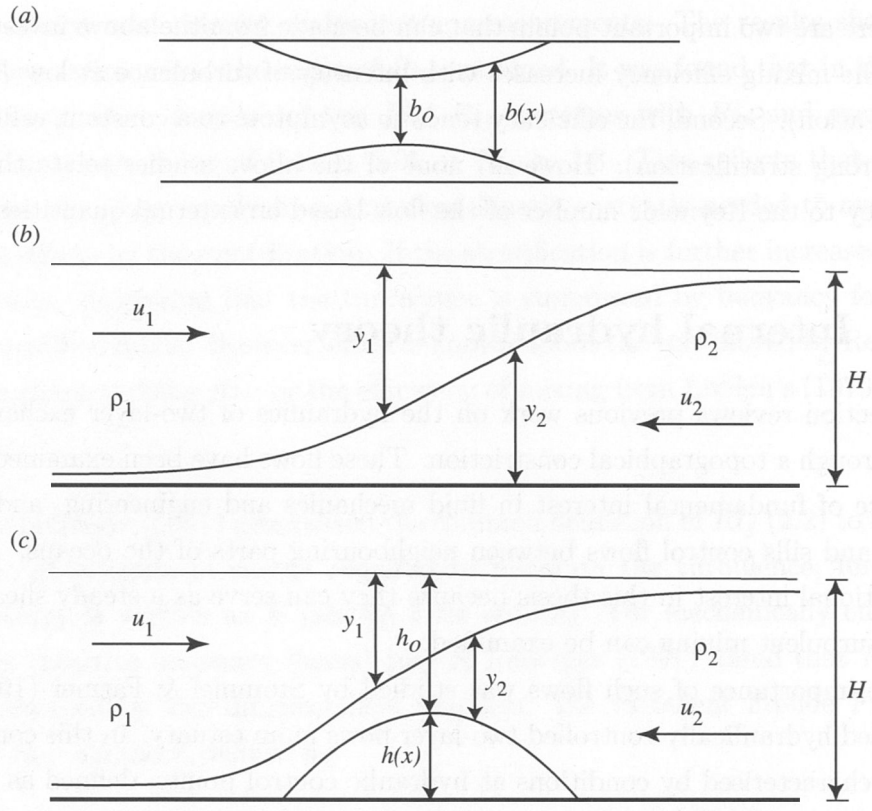

Figure 2.1: (a) Plan view of a contraction. Side views of a two-layer exchange flow (b) through a pure contraction and (c) over a pure sill.

rived analytical solutions for the problem of two flowing layers. The solutions for flow through a contraction or over a sill were obtained using continuity and Bernoulli equations. Provided that variations in both channel width and depth are small in the streamwise (x) direction, the solutions can be written as

$$\frac{1}{y_1}\frac{\partial y_1}{\partial x} = \frac{1}{b}\frac{\partial b}{\partial x}\left(\frac{G^2 - (1 + y_2/y_1)F_2^2}{1 - G^2}\right) + \frac{1}{y_1}\frac{\partial h}{\partial x}\left(\frac{F_2^2}{1 - G^2}\right) \tag{2.14}$$

and

$$\frac{1}{y_2}\frac{\partial y_2}{\partial x} = \frac{1}{b}\frac{\partial b}{\partial x}\left(\frac{G^2 - (1 + ry_1/y_2)F_1^2}{1 - G^2}\right) - \frac{1}{y_2}\frac{\partial h}{\partial x}\left(\frac{1 - F_1^2}{1 - G^2}\right), \tag{2.15}$$

where $b = b(x)$ is the contraction width, $h = h(x)$ is the sill height, $r = \rho_1/\rho_2$ is the ratio of the upper layer density to the lower layer density, $F_i^2 = u_i^2/g'y_i$ is the internal Froude number for the i th layer $(i = 1, 2)$, u_i is the flow speed in each layer at a given location x, y_i is the thickness of each layer, $g' = \epsilon g$ is the reduced gravity, g is acceleration due to gravity, $\epsilon = (\rho_2 - \rho_1)/\rho_2$ is the fractional density difference and G^2 is the composite Froude number, an important parameter that governs the

dynamics of the flow, and defined as

$$G^2 = F_1^2 + F_2^2 - \epsilon F_1^2 F_2^2. \tag{2.16}$$

For layered flows with a free surface and a sufficiently small density difference (i.e., $\epsilon \ll 1$), then (2.16) simply becomes

$$G^2 \approx F_1^2 + F_2^2. \tag{2.17}$$

The flow is said to be critical, or hydraulically controlled, at locations where the composite Froude number G^2 is equal to unity. Otherwise, the flow is classified as a supercritical or subcritical region depending on whether $G^2 > 1$ or $G^2 < 1$.

The application of the equations above for the case of a pure contraction, i.e., $\partial h/\partial x = 0$, as shown in Figure 2.1(a, b), implies that the flow is critical ($G^2 = 1$) at the minimum width of the contraction (the narrowest section) where $\partial b/\partial x = 0$. Similarly, for the case of a pure sill, i.e., $\partial b/\partial x = 0$, as shown in Figure 2.1(c), the flow is controlled ($G^2 = 1$) at the crest of the sill (the shallowest section) where $\partial h/\partial x = 0$. This topographic control point (either the contraction minimum width or the sill crest) may be complemented by a virtual control point, where the numerators in (2.14) and (2.15) are zero.

In the simple case of an exchange flow through a contraction and with zero barotropic component (i.e., a purely baroclinic flow with an equal but opposite volume transport in each layer), the topographic and virtual control points coalesce at the narrowest section. In this case supercritical flow is found everywhere throughout the channel except at this single control point. Subsequently, Armi & Farmer (1986) and Farmer & Armi (1986) developed the Froude-number plane for exchange flow with a net barotropic component. For the case of flow through a contraction ($\partial h/\partial x = 0$ in 2.15), the topographic control is located at the narrowest section and the virtual control is positioned upstream of the narrowest section with respect to the net flow (Armi & Farmer, 1986). For a net barotropic flow over a sill ($\partial b/\partial x = 0$ in 2.15), the topographic control is located at the shallowest point and the second control may occur closer to the reservoir containing the denser fluid (Farmer & Armi, 1986). We here refer these cases to (2.15) because of two reasons. First, this equation describes the spatial variation $\partial y_2/\partial x$ of the dense layer thickness of significant interest along the channel. Second, it contains explicitly the density ratio $r = \rho_1/\rho_2$ with which the Boussinesq approximation can be made ($1 - r = \epsilon \ll 1$).

Furthermore, when the topographic constrictions consist of both a contraction and a sill two possible types of exchange flow may occur. These flow types are

associated with cases where (1) the contraction coincides with the sill; or (2) the contraction and the sill are separated. In the first case the topographic control is located at the narrowest point of the constriction and the virtual control is situated upstream of the topographic control (relative to the dense layer). In the second case the topographic control is at the shallowest point and the second control is at the narrowest point. Farmer & Armi (1986) argued that the contraction affects the exchange flow only if it lies between the sill and the dense reservoir, as it does in the case of the Strait of Gibraltar, where the flow involves two control points at Camarinal Sill and Tarifa Narrows (Armi & Farmer, 1988).

Further theoretical developments for two-layer exchange flows have been based on examining the propagation of infinitesimal, long internal waves along the interface between the counter-flowing layers (Dalziel, 1991). Using functional approaches he proposed a simple formula from which one can examine the nature of the control points,

$$G^2 = 1 + \frac{C_1 C_2}{y_1 y_2}, \tag{2.18}$$

where C_1 and C_2 are the phase speeds of the interfacial waves, non-dimensionalised by $0.5(g'H)^{1/2}$. The ability of these waves to transfer information from one region to another characterises the exchange flow. Locations where the flow is critical ($G^2 = 1$) are simply positions along the flow, in which one of these wave speeds vanishes. It follows that either C_1 or C_2 must be zero at the points of hydraulic control.

In general cases where the two control points are spatially separated, the flow is subcritical ($G^2 < 1$) between the two control points, and is supercritical ($G^2 > 1$) between the control region and the reservoirs. In the subcritical region C_1 and C_2 are of opposite signs, representing the propagation of the long waves in both directions. In the supercritical region C_1 and C_2 are of the same sign, implying the propagation of the waves in only one direction, i.e., away from the subcritical region (see Hogg *et al.*, 2001*b*, for a detailed description on the properties of linear internal waves in stratified exchange flows). Thus changes in interface heights in the reservoirs are not communicated to the control region and have no effect on the exchange. For this reason the exchange transport is considered to be an upper bound to the possible transports (Armi, 1986; Armi & Farmer, 1987; Dalziel, 1991; Hogg *et al.*, 2001*a*), and is termed 'maximal' (see §2.3 for a further description).

The concept of maximal exchange in two-layer flows through channels with rectangular cross sections still applies to flows through channels with non-rectangular cross sections (Dalziel, 1992). If there is a control region where the flow is subcrit-

ical, bounded on each side by a supercritical region where the long internal waves are directed away from the control region, the exchange is then maximal (Armi & Farmer, 1987; Dalziel, 1991).

The use of two-layer hydraulic theory relies on the basic assumptions that the flow is immiscible, steady, inviscid, incompressible and hydrostatic (Lawrence, 1990, 1993). However, these fundamental assumptions are in general violated – one example of such a situation is described below. The phase speed C of the interfacial long waves in a two-layer flow is determined by the stability Froude number F_Δ^2 (see Lawrence, 1990; Zhu & Lawrence, 2000), which is given by

$$F_\Delta^2 = \frac{(u_2 - u_1)^2}{g'(y_1 + y_2)}. \tag{2.19}$$

Lawrence (1990) used the stability Froude number to examine the stability of the flow based on a criterion, $F_\Delta^2 \leq 1$ (Long, 1956). He showed that, together with G^2, this Froude number characterises the condition of the flow at any point in space. For example, the condition under which $F_\Delta^2 \leq 1$ and $G^2 = 1$ represents stable critical flows, suggesting that the maximum difference in the flow speed between the layers ($\Delta u = u_2 - u_1$) cannot exceed a critical value of $(g'H)^{1/2}$, where $H = y_1 + y_2$. Using (2.19) the wave phase speed C can then be written as

$$C \sim (1 - F_\Delta^2)^{1/2}. \tag{2.20}$$

It follows that the waves can have imaginary speeds when $F_\Delta^2 > 1$. This suggests that the flow may be unstable to shear during the propagation of the waves along the interface, leading to the generation of shear instability, hence mixing between the layers. If this is the case, then internal hydraulics is no longer exact as such a process fundamentally alters the nature of the flow (Lawrence, 1990).

Transport of water between two adjacent ocean basins is of significant interest. Hydraulic theory is found to be useful in predicting the transport for two-layer exchange flows in the oceans (e.g., the flow in the Bosphorus, Oğuz *et al.*, 1990; Gregg *et al.*, 1999; Gregg & Özsoy, 2002; Oğuz, 2005). However, measured transports show significant differences from the two-layer hydraulic prediction. Corrections to basic hydraulic theory can be made to account for time dependence (Helfrich, 1995), friction (Zhu & Lawrence, 2000; Gu & Lawrence, 2005), non-hydrostatic effects (Zhu & Lawrence, 1998, 2000), rotation effects (Whitehead *et al.*, 1974; Hunkins & Whitehead, 1992) and mixing (Winters & Seim, 2000; Hogg *et al.*, 2001; Stenström, 2003). It is the last case with which we are primarily concerned in this thesis. As a

by product of our investigation of the amount of turbulent mixing we also evaluate the rate of mass transport. In the next section we will discuss the maximal exchange for steady, two-layer hydraulic exchange flows and examine the roles of mixing and friction in the reduction of the transport.

2.3 Maximal exchange and transport reduction

A quantity of interest in most geophysical exchange flows is the exchange transport. As the presence of topography in these flows may induce hydraulic controls, internal hydraulic theory is then used to predict the maximum possible exchange transport. This transport of water occurs between marginal seas (or estuaries) and the open ocean, and may modify heat exchange with the atmosphere in areas that are remote from the control region. For example, the Mediterranean outflow through the Strait of Gibraltar (Bryden & Stommel, 1984; Armi & Farmer, 1988; Pratt & Lundberg, 1991) has a large influence on salt and heat fluxes over large parts of the North Atlantic. In the abyss the flow in the Denmark Strait plays an important role in feeding the North Atlantic Deep Water (NADW) (Dickson & Brown, 1994), and in setting the strength of the Atlantic meridional overturning circulation, which in turn has an impact on the European climate (Kösters *et al.*, 2005). Therefore, predicting inter-basin water transports is of global significance.

In the following discussion the maximal exchange transport through a channel connecting two reservoirs of water with different density is derived. For the case of a pure contraction, as shown in Figure 2.1(*a*, *b*), the maximal transports of both mass and volume can be simply calculated from external parameters (Hogg *et al.*, 2001*a*; Ivey, 2004). This requires a knowledge of flow variables at the control point: each layer has an equal height ($y_1 = y_2 = H/2$) and an equal but opposite velocity ($u_1 = -u_2$). We can calculate the net mass transport as the product of the density contrast and the maximal volume transport (determined by the height and velocity in each layer). Thus for no barotropic exchange, the net mass transport $M_{\max}$ through the contraction is given by

$$M_{\max} = 1/4 \Delta\rho b_o g'^{1/2} H^{3/2}, \tag{2.21}$$

where $\Delta\rho$ is the density contrast across the contraction, $g' = g\Delta\rho/\rho_o$ is the reduced gravity, g is the acceleration due to gravity, ρ_o is a reference density, b_o is the minimum width of the contraction and H is the total depth of the water. The corresponding baroclinic volume transport $Q_{\max}$ through the contraction in each

layer is given by

$$Q_{\max} = \frac{M_{\max}}{\Delta\rho}. \tag{2.22}$$

The maximal net mass transport in (2.21) can also be applied to exchange flow over a sill shown in Figure 2.1 (*c*), with H being replaced by h_o, which is the total water depth above the sill crest. Thus the net mass transport over the sill is

$$M_{\max} = 1/4\Delta\rho b_o g'^{1/2} h_o^{3/2}. \tag{2.23}$$

The same formulation for the maximal transport of mass as in (2.23) is obtained for convectively driven exchange flow in a stratified sill-enclosed basin (see Grimm & Maxworthy, 1999; Finnigan & Ivey, 2000; Ivey, 2004, for a detailed discussion).

The effects of turbulent mixing on the exchange transport have been studied by Hogg *et al.* (2001*a*) using two limiting analytical solutions of the flow. In one limit the internal hydraulic solution can be used to predict to first order the maximal exchange, provided that friction and mixing are negligible. In the other limit a viscous-advective-diffusive solution is applied, where viscous dissipation and turbulent mixing dominate the flow. It is found that the behaviour of the flow between these two limits can be best described by a single dimensionless parameter, $Gr_T\Lambda^2$, where Gr_T is the turbulent Grashof number, defined as $Gr_T = g'H^3/\kappa_\nu^2$ and Λ is the aspect ratio, defined as $\Lambda = H/L_m$. In this parameter, κ_ν is the turbulent eddy viscosity for momentum, H is the total water depth and L_m is the *length* of the mixed region.

Hogg *et al.* (2001*a*) demonstrated that for flows with sufficiently large $Gr_T\Lambda^2$ (of order 10^6), such as the Gibraltar (e.g., Armi & Farmer, 1988; Farmer & Armi, 1988), the mass transport is about 90% of the hydraulic solution given in (2.21). However, when there is significant vertical transport of either mass or momentum across the layers, the transports of both mass and volume may be further reduced and substantially less than the maximal prediction given in (2.21) and (2.22), respectively. For example, in the Bosphorus (Gregg *et al.*, 1999; Gregg & Özsoy, 2002), where $Gr_T\Lambda^2$ is of order 10^4 (Hogg *et al.*, 2001*a*), the transport is reduced to 70% of the maximal exchange in (2.21), and thus deviates significantly from the hydraulic solution.

The results of both laboratory experiments and numerical simulations suggest that mixing plays a key role in reducing the transport, in qualitatively good agreement with such field observations. In particular, laboratory measurements of a two-layer exchange flow through a constriction (Helfrich, 1995) showed that mixing is responsible for reducing the net mass transport from the maximal hydraulic solution in (2.21) by about 20%. Although Helfrich (1995) considered dependence

of such a flow upon geometrical and temporal parameters, the resulting transport reduction is for the case of no barotropic forcing, independent of the details of the channel geometry. Numerical simulations (Winters & Seim, 2000; Stenström, 2003) for steady shear flows demonstrated that volume transport is reduced by about 15% from the predicted maximal transport given in (2.22) owing to turbulent mixing. While Winters & Seim (2000) and Stenström (2003) used non-hydrostatic models, Helfrich (1995) demonstrated that departures from the hydrostatic assumption are still acceptable. However, other effects such as friction and rotation were not considered in both investigations. Of particular interest is that although mixing was found to be responsible for reducing the transport, the amount of mixing was not measured in these studies.

The role of non-hydrostatic effects needs also to be examined in practical laboratory flows. In this regard, Zhu & Lawrence (1998) explored these effects on flows over a sill, and found that the relevant parameter characterising these flows is the square of the aspect ratio $(H/L_s)^2$, where H is the water depth and L_s is the channel (sill) length. This parameter needs to be significantly less than one, i.e., $(H/L_s)^2 \ll 1$, for the hydrostatic assumption to be valid. The non-hydrostatic approach is only relevant to the case of 'approach-controlled' flows, in which a region of a 'supercritical leap' exists (i.e., the flow remains supercritical while experiencing a change in an interface height from a thin upper layer upstream of the sill to a thin lower layer downstream of the sill).

2.4 Lock-release gravity currents

Mixing in lock-release gravity currents has been investigated through laboratory experiments (Hallworth *et al.*, 1993; García & Parsons, 1996; Hacker *et al.*, 1996). These studies have examined some aspects of turbulent mixing processes between the dense current and the surrounding fluid when the current propagates along a horizontal surface. Hallworth *et al.* (1993) examined the way in which the current head became diluted while advancing over some distance. On the release of a fixed volume of the dense, alkaline current from the gate, an acidic ambient fluid began to neutralise this current through entrainment processes at the current head, where most mixing occurred. They demonstrated that a full change in the colour of the head occurred at a distance from the lock. Thus the amount of ambient fluid required to neutralise the head colour can be estimated.

The results of Hallworth *et al.* (1993) did not include the details of the change in internal density structure associated with mixing processes above the gravity current

head. Hacker *et al.* (1996) carried out lock-release gravity currents using various aspect ratios of the lock to examine mixing rates in the currents. The optical-based technique was used to analyse density structures of these currents. In this method the relatively dense current was dyed and the dye was diluted when this current mixed with the ambient fluid. The mixed fluid detrained from the current head was replaced with dense fluid from the rear of the current so as to maintain the shape of the head. As the current moved further, the fluid within the current became more diluted. For different aspect ratios, they concluded that differences in the density structure of the current were associated with different extents of the mixing process.

In addition, García & Parsons (1996) used a movable-base tank to produce a 'freezing' front and examine mixing at the front of a gravity current. It was found that the scale of the apparatus and Reynolds number influenced the rates of the mixing. Smaller mixing rates were obtained from experiments with relatively shallow water, associated with low Reynolds numbers.

However, neither of the above studies has measured the overall amount of mixing generated by lock-exchange experiments, rendering the mixing efficiency in gravity currents still unresolved. Because gravity currents in nature are able to propagate to a long distance while carrying fluid properties and sediments, the amount of turbulent mixing and hence the efficiency of the mixing in the currents needs to be measured. We will compare the results for these flows with those for the steady, hydraulically controlled exchange flows.

Chapter 3

Experimental methods

Laboratory experiments are the primary means used in this thesis to investigate exchange flow processes. The experiments can be divided into three distinct groups: exchange flow through contractions, exchange flow over sills and lock-release gravity currents in a uniform channel. In this chapter we outline the methodology as follows. The laboratory apparatus and procedures for each of these experiments are described in §3.1. The measurement techniques and flow visualisation are summarised in §3.2. The details of the experimental conditions for each type of the experiments, including additional runs with a short constriction using various dimensionless run times are reported in §3.3.

3.1 Laboratory apparatus and procedure

3.1.1 Exchange flows through constrictions

All experiments were conducted in a rectangular glass tank of total length $L = 5.26$ m and width $B = 0.2$ m. The tank had a flat, horizontal base and was of uniform width. In each experiment one of four acrylic, symmetric constrictions was placed at the centre of the channel length (Figure 3.1). Three of the constrictions had a sinusoidal shape for each side wall so that the width of the channel varied smoothly with horizontal distance (Figure 3.1*a*, *c*). More precisely, the constriction width was a function of cosine, i.e., $b = B(1 - \cos\frac{\pi x}{L_c}) + b_o \cos\frac{\pi x}{L_c}$, where $b \leq B$ represented the constriction wall along the streamwise direction, b_o was the minimum width of the constriction, L_c was the total length of the constriction and x was the distance along the channel (with $x = 0$ was taken to be at the mid-point of the constriction). The minimum widths of the three constrictions were 20 mm, 60 mm and 100 mm (for which the total constriction length L_c was 0.6 m, 0.5 m or 0.4 m, respectively).

The fourth constriction (Figure 3.1*b*, *d*) also varied smoothly but included a straight central section having parallel walls 0.06 m apart and 0.5 m in length (such that the total constriction length L_c was 1.0 m for this particular geometry). Throughout this thesis we refer to the first three constrictions as 'short constrictions' and the latter as the 'long constriction'.

In each experiment the tank was filled with freshwater to depth H and a sliding vertical barrier was inserted at the narrowest part (or central point) of the constriction dividing the tank into two reservoirs. A density difference between the reservoirs was created by dissolving a measured quantity of salt into the reservoir on the right-hand side of the barrier. In some experiments the denser water was dyed with food colouring for the purpose of flow visualisation. In other runs both the dense and light fluids were dyed with different colours. In each case both reservoirs were stirred thoroughly to ensure homogeneity in density.

After adding the salt and dye there was a small difference between the free surface heights on either side of the barrier. The free surface heights were adjusted to one of three different initial conditions: (1) the hydrostatic pressure was equalised at the bottom of the tank (by lifting the barrier a millimetre or two until there was no net flow); (2) the free surface heights were adjusted to equalise pressures in the two reservoirs at approximately mid-depth (see Appendix B for details); or (3) freshwater was added to the left reservoir so that the free surface heights were the same. In each case the two reservoirs were again stirred before the experiment to ensure homogeneity in density. In the majority of experiments condition (2) was used as only this case was expected to give a purely baroclinic exchange. In the case of equal pressures at the bottom of the tank (case 1) and for equal surface heights (case 3), the difference in the heights between the initial and final states contributes only minor amounts of energy to the total energy available for mixing (see Appendix B for a further explanation). In addition, the measured transports and mixing results to be presented in Chapter 5 show no dependence on which of these three initial states was used. Thus the experimental results presented in this thesis are insensitive to these initial conditions.

The exchange flow was initiated by the smooth and rapid removal of the sliding barrier. The time taken to slide the barrier out of the water was approximately 1 s in each case. At the end of this time the density interface remained vertical for most cases but the larger density differences. An assistant started a timer at the moment the barrier left the water. Gravity currents formed on each side of the constriction, and accommodated the exchange flux. In the main series of experiments the barrier was rapidly reinserted into the constriction at a time when the gravity currents had

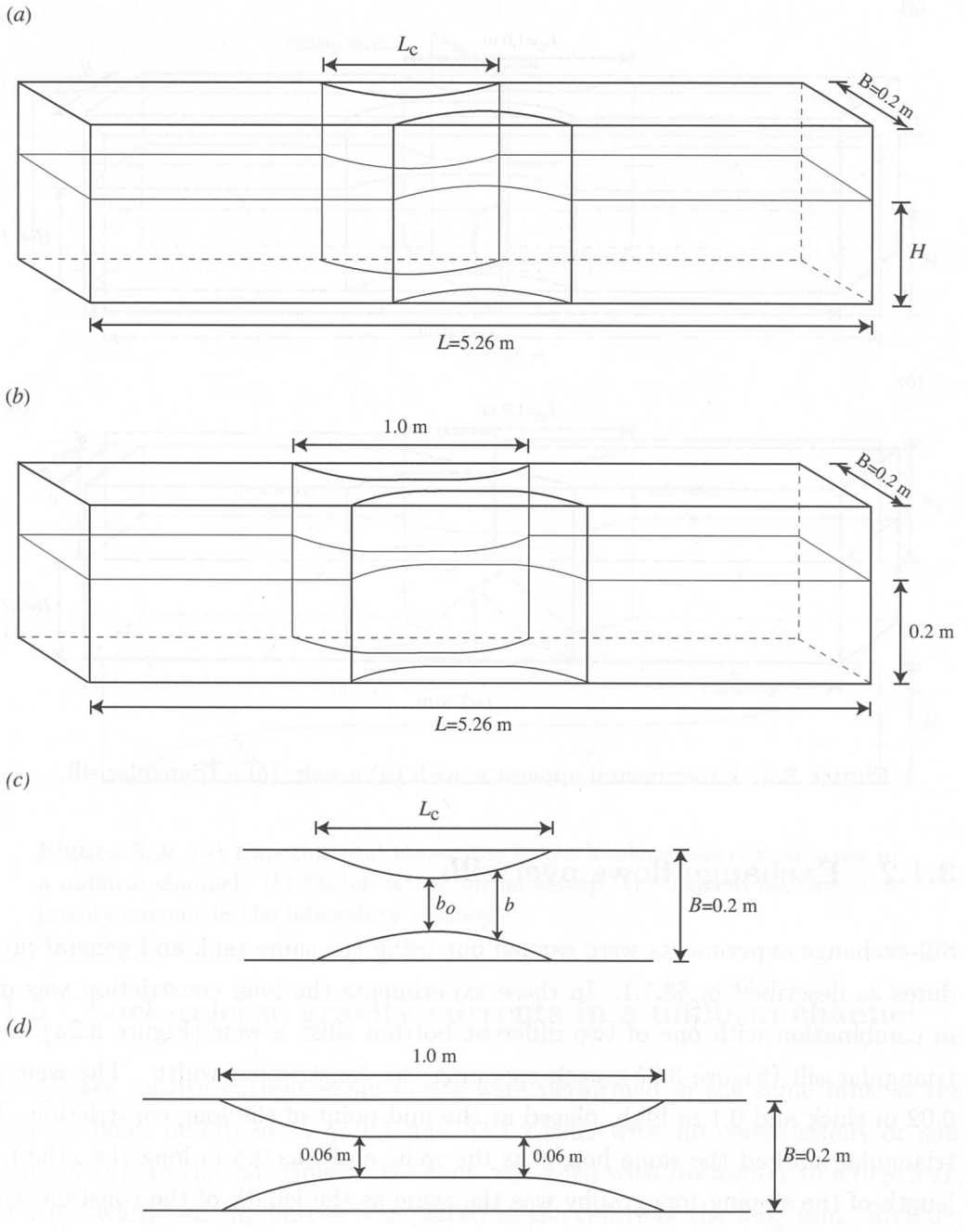

Figure 3.1: Experimental apparatus with (*a*) a short constriction; (*b*) a long constriction. Plan view of (*c*) the short constriction; (*d*) the long constriction.

nearly reached the endwalls of the tank. The timer was stopped as the barrier was inserted. Throughout the exchange the hydraulic control of the mean flow implied an approximately steady-state shear flow in the constriction, and the distant endwalls had no influence on the flow. The detail of the exchange flow is described in §5.1.

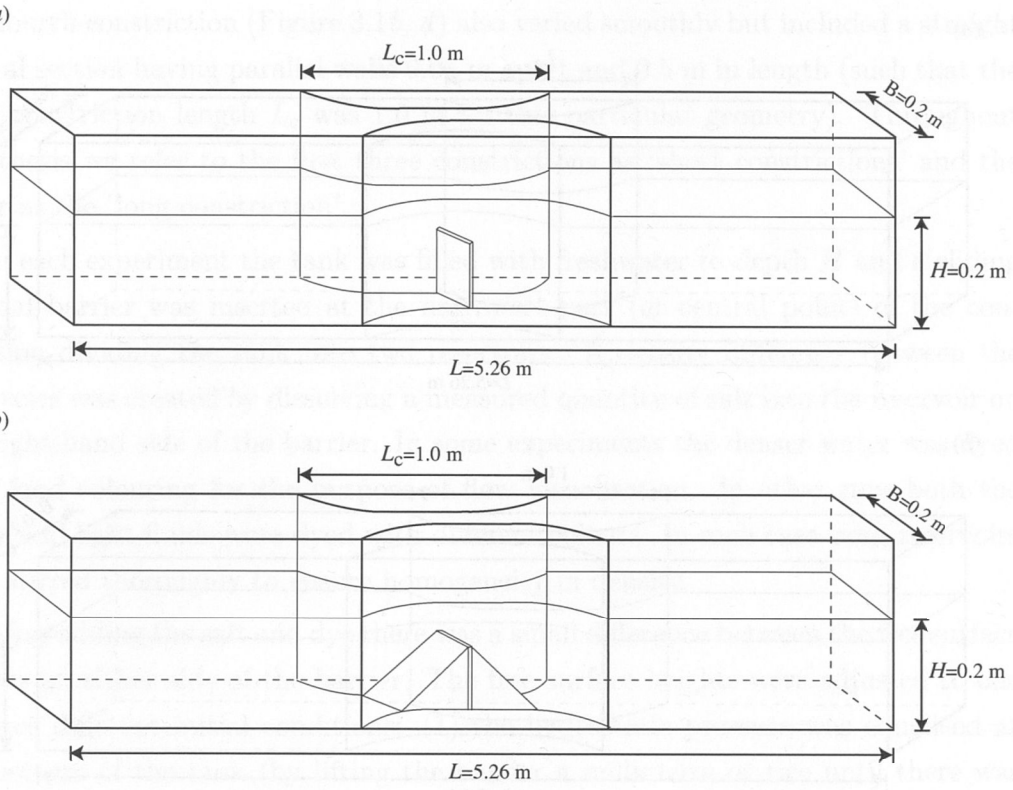

Figure 3.2: Experimental apparatus with (*a*) a weir; (*b*) a triangular sill.

3.1.2 Exchange flows over sills

Sill-exchange experiments were carried out using the same tank and general procedures as described in §3.1.1. In these experiments the long constriction was used in combination with one of two different bottom sills: a weir (Figure 3.2*a*) and a triangular sill (Figure 3.2*b*), each spanning the constriction width. The weir was 0.02 m thick and 0.1 m high, placed at the mid-point of the long constriction. The triangular sill had the same height as the weir, and was 0.5 m long (i.e., the total length of the sloping topography was the same as the length of the constant width section of the long constriction).

In each experiment the tank was filled with freshwater to a depth of 0.2 m, and a vertical barrier was inserted at the centre of the constant width section so as to make contact with the top of the sill. The followings are generic procedures for running an experiment. Salt and dye were added as required, the pressures in the two reservoirs were equalised at mid-depth (see Appendix B for further details), the reservoirs were stirred again, and the barrier was carefully withdrawn. The subsequent flow is described in §6.1.

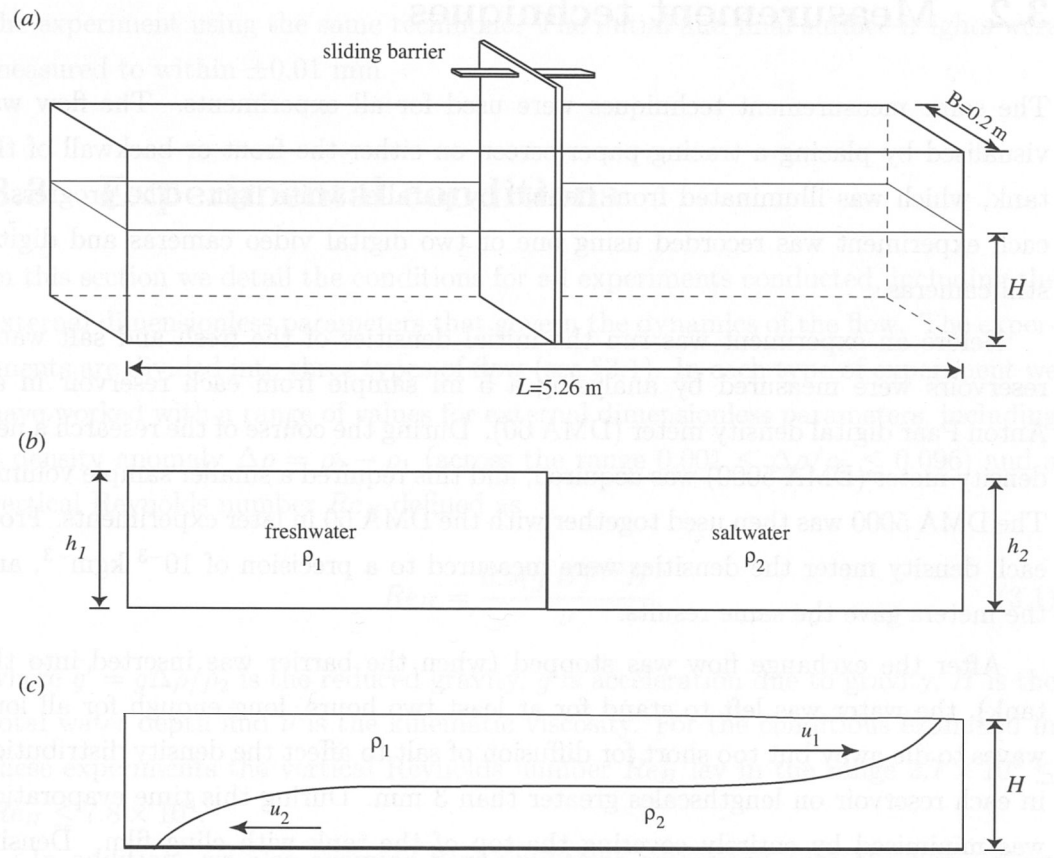

Figure 3.3: (*a*) Experimental apparatus for lock-release gravity currents in a uniform channel. (*b*) Sketch of the initial set-up. (*c*) Typical features of a gravity current in the laboratory channel.

3.1.3 Lock-release gravity currents in a uniform channel

Lock-release gravity current experiments were performed in the same tank as the exchange flows described in §3.1.1 and §3.1.2, but with no constrictions or sills (Figure 3.3*a*). In the experiments the tank was filled with freshwater to a depth H, and a full-width, sliding barrier was placed in the centre of the long tank, dividing it into two reservoirs of equal plan-form area. The procedures in these experiments were the same as those previously described in §3.1.1 and §3.1.2. Again, before running each experiment the free surface heights were adjusted to equalise pressures in the reservoirs at mid-depth (see Appendix B for details). After the barrier was withdrawn gravity currents propagated into each reservoir, with the dense fluid flowing along the base of the tank and the less dense fluid flowing in the opposite direction at the surface, as illustrated schematically in Figure 3.3(*c*). The detail of flow development is described in §7.1.

3.2 Measurement techniques

The same measurement techniques were used for all experiments. The flow was visualised by placing a tracing paper screen on either the front or backwall of the tank, which was illuminated from behind by parallel white light. The progress of each experiment was recorded using one or two digital video cameras and digital still cameras.

Before an experiment was run the initial densities of the fresh and salt water reservoirs were measured by analysing a 5 ml sample from each reservoir in an Anton Paar digital density meter (DMA 60). During the course of the research a new density meter (DMA 5000) was acquired, and this required a smaller sample volume. The DMA 5000 was then used together with the DMA 60 in later experiments. From each density meter the densities were measured to a precision of 10^{-3} kgm^{-3}, and the meters gave the same results.

After the exchange flow was stopped (when the barrier was inserted into the tank), the water was left to stand for at least two hours, long enough for all long waves to die away but too short for diffusion of salt to affect the density distribution in each reservoir on lengthscales greater than 3 mm. During this time evaporation was minimised by entirely covering the top of the tank with cling film. Density profiles were measured by taking 20 samples from each reservoir using a rake of hypodermic sampling tubes spaced vertically at 1 cm intervals throughout the water column. Each tube was attached to a syringe, and all of the syringes were mounted in a simple apparatus that allowed all samples to be withdrawn at the same time. The density of each sample was then measured using the DMA 60 (in most experiments) or both the DMA 60 and DMA 5000 (in some experiments).

Over the course of the work it has been found to be more accurate to use direct density measurements of samples rather than measurements of conductivity or refractive index either of sample or *in situ*. Determination of density from both conductivity and refractive index is limited to an accuracy of 10^{-1} kgm^{-3} (Ruddick & Shirtcliffe, 1979). Density needs to be measured to an accuracy of at least 10^{-2} kgm^{-3} in order to determine potential energy differences between vertical profiles sufficiently accurately for our purposes.

In addition to the density measurements, very accurate measurements of the free surface heights of the fresh and saltwater reservoirs were required to calculate initial and final potential energies in the water column. The initial heights were measured before each experiment using a digital micrometer gauge with an attached upward-pointing needle immersed in the water. The final heights were also measured after

the experiment using the same technique. The initial and final surface heights were measured to within ± 0.01 mm.

3.3 Experimental conditions

In this section we detail the conditions for all experiments conducted, including the external dimensionless parameters that govern the dynamics of the flow. The experiments are divided into three types of flow (see §3.1). In each type of experiment we have worked with a range of values for external dimensionless parameters, including a density anomaly $\Delta\rho = \rho_2 - \rho_1$ (across the range $0.001 \leq \Delta\rho/\rho_2 \leq 0.096$) and a vertical Reynolds number Re_H defined as

$$Re_H = \frac{0.5(g'H)^{1/2}H}{\nu}, \tag{3.1}$$

where $g' = g\Delta\rho/\rho_2$ is the reduced gravity, g is acceleration due to gravity, H is the total water depth and ν is the kinematic viscosity. For the conditions examined in these experiments the vertical Reynolds number Re_H lay in the range $2.7 \times 10^3 \leq Re_H \leq 7.8 \times 10^4$.

In addition, we also examine flow conditions associated with the flow aspect ratios H/L_c, the constriction aspect ratio B/L_c and the contraction aspect ratio b_o/B (see Figure 3.1), where L_c is the total length of the constriction and B is the full width of the tank. Different combinations of vertical Reynolds number and aspect ratio characterise the flow in each experiment.

Apart from the density of the salt solution, and the minor effect of salt concentration on the kinematic viscosity ν, the physical fluid properties are adequately described by a nominal, fixed Schmidt number $S_c = \nu/\kappa \approx 10^3$, where the kinematic viscosity ν is of 1.1×10^{-6} m^{2}s^{-1} and the molecular diffusion coefficient for salt κ is of 1.5×10^{-9} m^{2}s^{-1}. The water was always at the room temperature of 24 ± 2°C, in an air-conditioned laboratory.

3.3.1 Flows through constrictions

We carried out a main series of experiments (thirty nine runs) in exchange flows through constrictions, comprising thirty runs using the short constrictions and nine runs using the long constriction, in which the exchange flow was stopped shortly before the gravity current noses reached the ends of the long tank. A summary of these experiments with the short constrictions is given in Table 3.1. In these

experiments the constriction minimum width b_o, the reservoir density difference $\Delta\rho$ and the total water depth H were systematically varied. The fractional density difference $\Delta\rho/\rho_2$ was across the range of 0.001 to 0.096, and the water depth H was set to 0.1 m, 0.2 m or 0.3 m. The three values of b_o were associated with different constriction lengths L_c (see §3.1.1).

Several experiments were run using the same $\Delta\rho/\rho_2$ and H, but with different b_o (and L_c), testing the sensitivity of the results to the constriction geometry. Another series of experiments was run using the same b_o and $\Delta\rho/\rho_2$, but with different water depths H in order to examine the role of the vertical lengthscale in the flow dynamics.

In addition, the results for the short constrictions were compared with those from nine runs with the long constriction. Table 3.2 gives a summary of the experiments with the long constriction. In this case the water depth H was always 0.2 m and the only variable changed was the fractional density difference $\Delta\rho/\rho_2$ (across the range $0.003 \leq \Delta\rho/\rho_2 \leq 0.092$), testing the sensitivity of the results to the density difference and the consequent flow velocity and level of turbulence.

For the short constrictions the flow aspect ratio H/L_c varied from 0.17 to 0.52. For the case of the long constriction this ratio was $H/L_c = 0.2$. Thus $(H/L_c)^2$ varied between 0.03 and 0.27 in flows through the constrictions. Previous experiments (Zhu & Lawrence, 1998) showed that non-hydrostatic effects at similar aspect ratios to those used here do not influence the flow, and this conclusion is also consistent with scaling of the momentum equation in which non-hydrostatic mean flow effects appear to be important at order $(H/L_c)^2$.

After examining the roles of all parameters we find that the mixing efficiency and mass transport are a function of the product of Re_H (3.1) and L_c/H, which we write as the horizontal Reynolds number Re,

$$Re = \frac{0.5(g'H)^{1/2}L_c}{\nu}. \tag{3.2}$$

The lengthscale of interest is the distance over which the fluid accelerates (and over which a train of billows was observed to form) or the length of the mixing region. This is the physical reason why the horizontal Reynolds number based on the constriction length L_c best characterises the flow in these experiments. The horizontal Reynolds number Re lie in the range $1.2 \times 10^4 \leq Re \leq 2.1 \times 10^5$. We will examine later in §5.3 the dependence of the measured efficiencies and transports on this Reynolds number.

Combinations of variable values were chosen so as to cover the maximum pos-

Exp	b_o (mm)	L_c (m)	$\Delta\rho/\rho_2$ (%)	H (m)	Re	t_r (s)
A8	20	0.6	0.7	0.2	3.5×10^4	58
B6	20	0.6	0.7	0.2	3.5×10^4	88
A7	20	0.6	1.0	0.2	4.2×10^4	55
A6	20	0.6	1.2	0.2	4.6×10^4	58
A5	20	0.6	1.5	0.2	5.1×10^4	60
E11	20	0.6	1.9	0.3	7.1×10^4	38
E16	20	0.6	1.9	0.2	5.8×10^4	49
E14	20	0.6	1.9	0.1	4.1×10^4	72
E8	20	0.6	2.4	0.2	6.6×10^4	43
E1	20	0.6	3.1	0.2	7.5×10^4	37
E10	20	0.6	4.8	0.3	11.6×10^4	24
B3	20	0.6	4.8	0.2	9.4×10^4	15
B2	20	0.6	4.8	0.2	9.4×10^4	30
E7	20	0.6	4.8	0.2	9.4×10^4	29
E9	20	0.6	4.8	0.2	9.4×10^4	30
E13	20	0.6	4.8	0.1	6.7×10^4	44
E19	20	0.6	4.8	0.1	6.5×10^4	45
E2	20	0.6	6.7	0.2	11.3×10^4	24
E18	20	0.6	9.2	0.3	15.6×10^4	17
E17	20	0.6	9.3	0.2	12.8×10^4	21
E15	20	0.6	9.3	0.1	9.0×10^4	33
E3	20	0.6	9.6	0.2	13.7×10^4	19
F2	60	0.5	0.1	0.2	1.2×10^4	147
F1	60	0.5	0.3	0.2	2.0×10^4	89
C5	60	0.5	0.7	0.2	2.9×10^4	60
F3	60	0.5	3.0	0.2	6.1×10^4	27
F4	60	0.5	6.7	0.2	9.0×10^4	18
C6	100	0.4	0.7	0.2	2.3×10^4	59
F5	100	0.4	3.0	0.2	4.8×10^4	24
F6	100	0.4	6.7	0.2	7.2×10^4	16

Table 3.1: List of conditions for experiments with the short constrictions.

sible range of both the aspect ratio L_c/H and the vertical Reynolds number Re_H, hence the horizontal Reynolds number Re. Another important aspect ratio is the contraction aspect ratio b_o/B, which was between 0.1 and 0.5, small enough to justify the use of hydraulic theory in predicting the maximal transport for these flows. Note that this ratio was equal to one for gravity current experiments as there is no contraction in the channel, hence no hydraulic control.

Exp	b_o (mm)	L_c (m)	$\Delta\rho/\rho_2$ (%)	H (m)	Re	t_r (s)
H1	60	1.0	0.3	0.2	3.8×10^4	93
H2	60	1.0	0.7	0.2	5.8×10^4	60
H3	60	1.0	1.9	0.2	9.6×10^4	34
H4	60	1.0	3.0	0.2	12.0×10^4	28
H5	60	1.0	4.9	0.2	15.5×10^4	21
H6	60	1.0	6.7	0.2	18.1×10^4	17
H7	60	1.0	9.2	0.2	21.2×10^4	16
H8	60	1.0	0.7	0.2	5.8×10^4	61
H9	60	1.0	8.0	0.2	19.8×10^4	18

Table 3.2: List of conditions for experiments with the long constriction.

Exp	b_o (mm)	L_c (m)	$\Delta\rho/\rho_2$ (%)	H (m)	Re	t_r (s)
J1	60	1.0	0.7	0.2	2.0×10^4	82
J2	60	1.0	4.8	0.2	5.4×10^4	30
J3	60	1.0	3.0	0.2	4.2×10^4	40
J4	60	1.0	1.9	0.2	3.4×10^4	47
J5	60	1.0	6.7	0.2	6.4×10^4	24
J6	60	1.0	9.4	0.2	7.6×10^4	22

Table 3.3: List of conditions for experiments with the weir.

3.3.2 Flows over sills

We conducted two series of experiments in exchange flows over sills, where a sill was placed at the centre of the long constriction (see §3.1.2 and Figure 3.2). These consisted of six runs with the weir (Table 3.3) and nine runs with the triangular sill (Table 3.4). These experiments were designed to examine the effects of bottom topography in altering the mixing processes near the sill.

We use a different definition of vertical Reynolds number for this type of experiment (compared with flows through the constrictions). The vertical Reynolds number Re_h is defined as

$$Re_h = \frac{0.5(g'H/2)^{1/2}H}{\nu}. \tag{3.3}$$

Note that the flow speed scaled with $(g'H/2)^{1/2}$ because the sill occupied a half of the total water depth (for which the water depth over the sill was only $H/2$). The only variable changed was the density difference $\Delta\rho$ across the barrier: the fractional density difference lie in the range $0.007 \leq \Delta\rho/\rho_2 \leq 0.095$, corresponding to $2.7 \times 10^3 \leq Re_h \leq 1.5 \times 10^4$.

As in flows through the constrictions, the horizontal Reynolds number in these

Exp	b_o (mm)	L_c (m)	$\Delta\rho/\rho_2$ (%)	H (m)	Re	t_r (s)
K1	60	1.0	0.7	0.2	4.2×10^4	84
K2	60	1.0	4.9	0.2	10.9×10^4	27
K3	60	1.0	2.9	0.2	8.4×10^4	36
K4	60	1.0	1.9	0.2	6.7×10^4	47
K5	60	1.0	1.9	0.2	6.8×10^4	48
K6	60	1.0	6.7	0.2	12.7×10^4	24
K7	60	1.0	9.5	0.2	15.2×10^4	19
K8	60	1.0	7.9	0.2	13.9×10^4	20
K9	60	1.0	0.3	0.2	2.7×10^4	131

Table 3.4: List of conditions for experiments with the triangular sill.

experiments is a combination of this vertical Reynolds number Re_h (3.3) and the aspect ratio L_c/H. However, it should be noted that the lengthscale of interest may be different for each sill. This leads to different definitions of horizontal Reynolds numbers for cases with the weir and with the triangular sill. For the case of the triangular sill the horizontal Reynolds number is defined as $Re = 0.5(g'H/2)^{1/2}L_c/\nu$ based on the constriction length L_c, which characterises the scale over which billows were observed to form on both sides of the sill. For the weir case we define the horizontal Reynolds number as $Re = 0.5(g'H/2)^{1/2}L_c/2\nu$. In this case we use a half of the constriction length as the relevant lengthscale because this characterises the scale over which strong turbulence was observed to develop (hence enhanced mixing was restricted only to the left side of the sill).

3.3.3 Gravity currents in a uniform channel

We conducted eleven experiments with lock-release gravity currents in a channel of uniform width $B = 0.2$ m and a flat base. These had a water depth H of either 0.2 m (G1-G7) or 0.3 m (G8-G11), as shown in Table 3.5. For each H the density difference $\Delta\rho$ across the barrier was varied ($0.007 \leq \Delta\rho/\rho_2 \leq 0.067$).

Unlike the exchange flow cases, the gravity current experiments were carried out with no topographic constrictions placed inside the tank. Thus the only external lengthscale (until the gravity currents reached the endwalls) was the water depth H. Hence, these 'uncontrolled' gravity current flows must be characterised by the vertical Reynolds number Re_H (3.1), which varied between 1.2×10^4 and 5.6×10^4. There are no aspect ratios describing the geometry as the channel is uniform in width and the full length L of the reservoirs is not relevant throughout the period before the gravity currents reached the endwalls. Unless the density difference between the

Exp	H (m)	$\Delta\rho/\rho_2$ (%)	Re_H	t_r (s)
G1	0.2	0.7	1.2×10^4	48
G2	0.2	1.9	1.9×10^4	29
G3	0.2	3.0	2.4×10^4	23
G4	0.2	3.9	2.8×10^4	19
G5	0.2	4.8	3.1×10^4	17
G6	0.2	6.7	3.6×10^4	14
G7	0.2	1.9	1.9×10^4	29
G8	0.3	3.0	4.5×10^4	16
G9	0.3	4.8	5.6×10^4	14
G10	0.3	1.9	3.6×10^4	23
G11	0.3	0.7	2.1×10^4	37

Table 3.5: List of conditions for gravity current experiments.

reservoirs was large enough to introduce significant non-Boussinesq effects (through the role of density in the acceleration terms of the momentum equation), the flows considered here were symmetric about the mid-point of the channel, and Re_H was the only dimensionless parameter varied.

3.3.4 Additional experiments

It is also of interest to examine traveling time of the gravity current from the exit of the constriction to the endwall, and compare this time with the experimental run time t_r. We write this 'theoretical time' as $t_g = (L - L_c)/2u_g$, where u_g is the current speed defined as $u_g = c(g'H)^{1/2}$, where c is a constant that depends on the constriction geometry and that can be estimated from the data in Table 3.1. We find c for three different geometries to be 0.23 ($b_o = 20$ mm), 0.34 ($b_o = 60$ mm) and 0.36 ($b_o = 100$ mm). We then define the dimensionless time τ for all experiments as $\tau = t_r/t_g$. For the parameters used we find that this dimensionless time has to be at $\tau \approx 1.0$ for the nose of the gravity current to reach the endwall.

Based on the above analysis additional runs with $\tau < 1.0$ for a particular flow condition were carried out in order to examine whether the mixing might depend on time. Runs with a short constriction ($b_o = 20$ mm) having small ($\Delta\rho/\rho_2 = 0.7\%$) and large ($\Delta\rho/\rho_2 = 4.8\%$) fractional density differences were chosen for this purpose. Another series of runs with the same constriction geometry and fractional density differences was also conducted where the barrier was reinserted into the constriction after the gravity currents were reflected from the endwalls of the tank (i.e., runs with $\tau > 1.0$). In these runs the flow in the constriction was thought to remain

Exp	b_o (mm)	H (m)	$\Delta\rho/\rho_2$ (%)	Re	τ
A8	20	0.2	0.7	3.5×10^4	0.7
B6	20	0.2	0.7	3.5×10^4	1.0
B5	20	0.2	0.7	3.5×10^4	1.3
B4	20	0.2	0.7	3.5×10^4	2.0
B3	20	0.2	4.8	9.4×10^4	0.5
B2	20	0.2	4.8	9.4×10^4	0.9
B1	20	0.2	4.8	9.4×10^4	1.4
A1	20	0.2	4.8	9.4×10^4	1.8
E5	20	0.2	4.8	9.4×10^4	3.1
E4	20	0.2	4.8	9.4×10^4	5.5

Table 3.6: List of conditions for experiments with the same $b_o = 20$ mm and $H = 0.2$ m but different fractional density differences ($\Delta\rho/\rho_2 = 0.7\%$ and 4.8%), having dimensionless run time in the range $0.5 \leq \tau \leq 5.5$.

Exp	b_o (mm)	H (m)	$\Delta\rho/\rho_2$ (%)	Re
R1	20	0.2	0.7	3.5×10^4
R2	20	0.2	1.2	4.5×10^4
R3	20	0.2	3.0	7.4×10^4
R4	20	0.2	4.8	9.4×10^4
R5	60	0.2	0.7	2.9×10^4
R6	60	0.2	4.8	7.9×10^4
R7	100	0.2	4.8	6.3×10^4

Table 3.7: List of conditions for rundown cases, using the short constrictions with $H = 0.2$ m and three different constriction widths b_o for various fractional density differences $\Delta\rho/\rho_2$.

steady (reflected waves had not reached the constriction), but large amplitude waves with associated mass transport may have caused a vertical displacement of density interfaces that led to an increase in the potential energy. All of these runs are summarised in Table 3.6 (with two experiments B6 and B2 having $\tau \approx 1.0$ for comparison).

In addition, we carried out a small number of runs in which the barrier was not replaced into the tank. These runs were called 'rundown cases', where the flow was allowed to decay to a final state of no motion and no horizontal density gradient. A summary of experimental conditions for the rundown cases is given in Table 3.7. The same general procedure and measurement techniques as those in exchange flows with finite run times were used in these cases. The flow is described in §5.1 and the resulting mixing is discussed in §5.3.

Chapter 4

Theoretical considerations

This chapter presents the theoretical framework for the measurement and analysis of the exchange flows. The equation of state for salt solutions is briefly introduced in §4.1, along with the approximation of a dependence of density on salinity during mixing. The method for calculating mass transport between the reservoirs is given in §4.2. The potential energy budget that leads to an expression for the efficiency of mixing is presented in §4.3. In §4.4 we present a scaling analysis and a prediction for the mixing efficiency, based on the modifications in the potential and kinetic energies in an interfacial mixing layer. In §4.5 the scaling analysis provides a theoretical estimate for the net mass transport in exchange flows through a short constriction, including the roles of both mixing and friction in the flux reduction.

4.1 The equation of state

In general, the density of water depends upon temperature, salinity and pressure, or $\rho = \rho(T, S, p)$. However, under the laboratory conditions used in this work we have density as a function of salinity alone. The isothermal equation of state for salt solutions can be represented by a polynomial (Ruddick & Shirtcliffe, 1979),

$$\rho = \rho_o\big(1 + \beta_1(S - S_o) + \beta_2(S - S_o)^2 + \ldots, \tag{4.1}$$

where ρ_o and S_o are reference values of density and salinity, respectively, and S is the salinity in kg of salt per kg of solution. If the reference density ρ_o is taken to be 998.234 kgm^{-3}, the density of freshwater at 20°C, then the constants take values $\beta_1 = 0.709693$ and $\beta_2 = 0.122737$.

Mass of both water and salt is always conserved. However, the non-linear equation of state (4.1) may affect measurements of water volume in the reservoirs when

mixing occurs during the experiment. We examine this effect by carrying out a simple experiment (see §5.5 for details of the result) with a large density difference, where the mixing tends to decrease the total water volume. This may result in an increase in the internal potential energy, thus reducing the gravitational potential energy owing to mixing. In the following analysis we will assume a linearised form of (4.1) as follows,

$$\rho = \rho_o\big(1 + \beta_1(S - S_o)\big). \tag{4.2}$$

4.2 Calculation of mass transport

Before an experiment was run, the initial densities of the fresh and saltwater reservoirs, ρ_1 and ρ_2, respectively, were measured. After the exchange flow was stopped and all motions had ceased the density profiles in the fresh and saltwater reservoirs, $\rho_1'(z)$ and $\rho_2'(z)$, respectively, were measured. From these measurements and the conservation of mass (or salt) we calculate the mass exchanged. The time-averaged net rate of mass transport through a channel connecting the reservoirs can be written as

$$M_{\text{obs}} = \frac{1}{t_r}\int_0^{h_1'} A\left(\rho_1'(z) - \rho_1\right) \mathrm{d}z, \tag{4.3}$$

where A is the horizontal cross section of each reservoir (which may be uniform or dependent on height), t_r is the experimental run time, z is the vertical coordinate, taken to be zero at the base of the channel and h_1' is the final free surface height of the freshwater (left) reservoir. This quantity represents the increase in mass in the left-hand reservoir resulting from the amount of salt transported through the channel.

For exchange flows through the constrictions and over the weir, $A = A_o$ (i.e., the cross-sectional area of each reservoir is uniform with height) so that the empirical rate of mass transport through the constant cross-section channel is

$$M_e = \frac{A_o}{t_r}\int_0^{h_1'} \left(\rho_1'(z) - \rho_1\right) \mathrm{d}z. \tag{4.4}$$

In experiments with the triangular-shaped sill each reservoir has a depth-dependent cross-sectional area,

$$A = \begin{cases} A_o & \text{for } z > d, \\ A_o - ab_o\Big(1 - \dfrac{z}{d}\Big) & \text{for } 0 \le z \le d, \end{cases} \tag{4.5}$$

where $d = 0.1$ m is the height of the sill and $a = 0.25$ m is a half of the length of the constriction central section. Then substituting (4.5) into (4.3) yields

$$M_e = \frac{A_o}{t_r}\left(\int_0^d \left(1 - \frac{ab_o}{A_o}\left(1 - \frac{z}{d}\right)\right)\left(\rho_1'(z) - \rho_1\right) \mathrm{d}z + \int_d^{h_1'} \left(\rho_1'(z) - \rho_1\right) \mathrm{d}z\right). \quad (4.6)$$

The mass of salt transported is closely related to the exchange of mass. The mass flux of salt is given by

$$M_{\text{salt}} = \frac{1}{t_r}\int_0^{h_1'} A\left(\rho_1'(z)S_1'(z) - \rho_1 S_1\right) \mathrm{d}z, \quad (4.7)$$

where $S_1'(z)$ is the vertical profile of salinity in the left reservoir after the flow was stopped, h_1' is again the water depth in that reservoir after the flow was stopped and S_1 is the salinity (measured in kg of salt per kg of solution).

In the approximation that density and salinity are linearly related, as described by (4.2), we write $\rho_1'(z) - \rho_1 = \rho_1\beta\big(S_1'(z) - S_1\big)$ in (4.3). If we also assume $\rho_1'(z) - \rho_1 \ll \rho_1$ (as commonly found in the Boussinesq approximation), then we can write $\rho_1'(z)S_1'(z) - \rho_1 S_1 = \rho_1\big(S_1'(z) - S_1\big)$ in (4.7). Hence

$$M_{\text{salt}} = \frac{M_e}{\beta}, \quad (4.8)$$

and in this approximation the requirements for conservation of mass of both water and salt are no longer independent.

4.3 Calculation of mixing

In this section we derive a method of calculating the efficiency of mixing in a buoyancy-driven exchange flow. The formulations derived below are applicable to channels having either uniform or variable cross-section.

We define the mixing efficiency as the fraction of the available potential energy released to kinetic energy of the flow that is transformed into an irreversible increase in the potential energy of the density distribution owing to mixing. Thus the final potential energy must be compared with the potential energy state that would be achieved if there were no mixing. We rewrite the efficiency of mixing (2.10) as

$$\eta = \frac{\Delta P}{\Delta K} = \frac{P_m}{P_a}, \quad (4.9)$$

where P_m is the potential energy increase owing to mixing (the 'amount of mixing')

and P_a is the available potential energy released. In the previous definition (2.10) ΔK is the amount of turbulent kinetic energy supplied. In our definition (4.9), to better suit the problem of mixing owing to instability in a buoyancy-forced shear flow, the denominator P_a is the total mechanical energy supplied, whether as kinetic energy of the mean flow or as turbulent kinetic energy. Thus (4.9) represents the overall efficiency with which mixing draws on the available energy in this type of flow. We also argue later that the dissipation of kinetic energy from the mean flow is in the present experiments dominated by turbulent dissipation associated with the flow through the constriction or over the sill, making (4.9) effectively equivalent to (2.10).

Knowledge of the initial and final states is needed to calculate the mixing efficiency. The initial state, shown in Figure 4.1(a), has two basins of homogeneous water of different density. In this state the gravitational potential energy of the water masses is given by

$$P_i = g \int_0^{h_1} A\rho_1 z \, \mathrm{d}z + g \int_0^{h_2} A\rho_2 z \, \mathrm{d}z, \tag{4.10}$$

where h_1 and h_2 are the initial free surface heights of the fresh and saltwater reservoirs, respectively.

We define the final state after the exchange flow and mixing have occurred and altered the properties of water on both sides of the constriction (see Figure 4.1b). The gravitational potential energy in this state is determined by an integral based on the measured density distribution in both reservoirs, and is written as

$$P_f = g \int_0^{h_1'} A\rho_1'(z) z \, \mathrm{d}z + g \int_0^{h_2'} A\rho_2'(z) z \, \mathrm{d}z, \tag{4.11}$$

where h_1' and h_2' are the final free surface heights of the fresh and saltwater reservoirs, respectively.

We examine the change in potential energy in the channel by defining the hypothetical minimum potential energy state that would be present if mixing did not occur during the flow – but the same mass were transported – this serves as the 'background' state. This hypothetical state is obtained by notionally redistributing the measured total amount of salt within each reservoir into fresh and saltwater layers of densities ρ_1 and ρ_2 in the final state (see Figure 4.1c). We then write the required thicknesses of the fresh and saltwater layers in each of the reservoirs 1 and 2 for this hypothetical state as h_{fi} (i = 1, 2) and h_{si} (i = 1, 2), respectively. The actual final potential energy (4.11) is greater than this hypothetical minimum po-

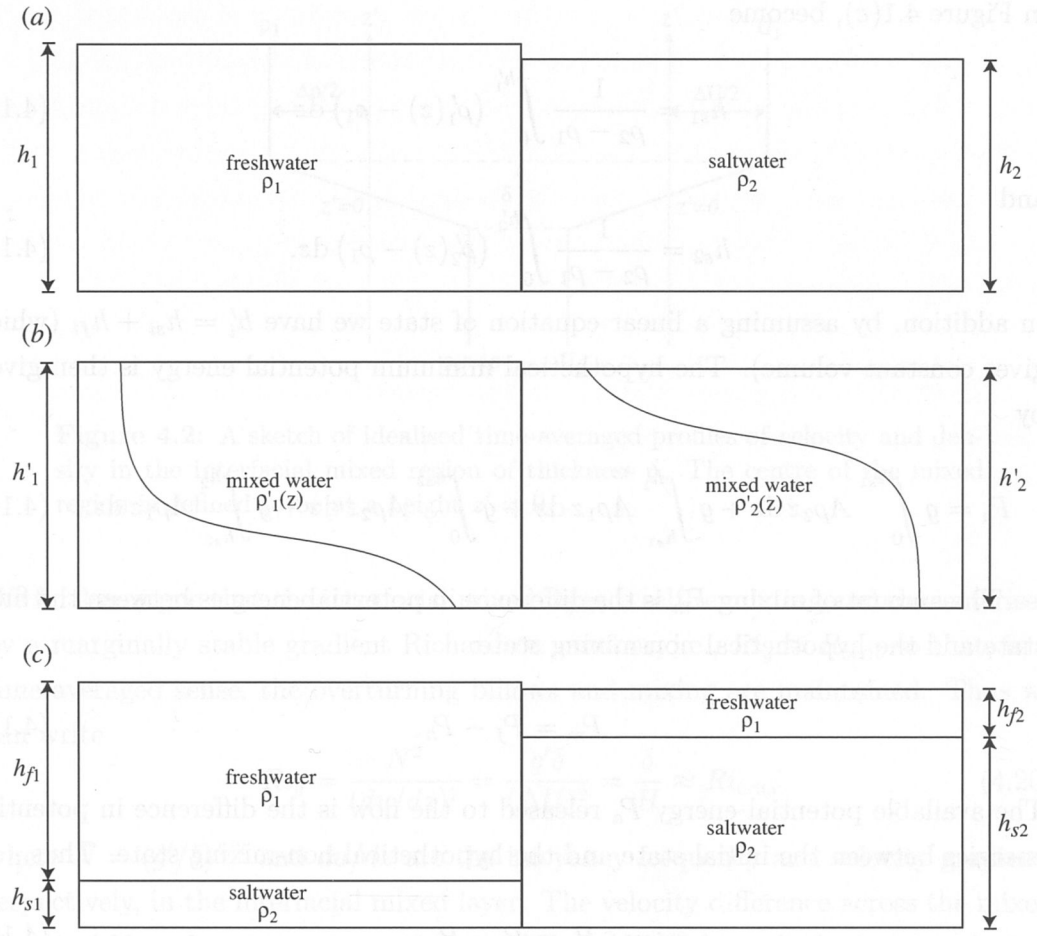

Figure 4.1: (*a*) The initial state (where h_1 is not in general the same as h_2). (*b*) The final state indicating the density profiles measured after the experiment. (*c*) The hypothetical minimum potential energy state following partial redistribution of salt within each reservoir without any mixing.

tential energy. The required redistribution of salt in the vertical to form a two-layer stratification in each reservoir must satisfy conservation of mass below,

$$\int_0^{h'_1} \rho'_1(z) A \, \mathrm{d}z = \int_0^{h_{s1}} \rho_2 A + \int_0^{h_{f1}} \rho_1 A \, \mathrm{d}z \tag{4.12}$$

and

$$\int_0^{h'_2} \rho'_2(z) A \, \mathrm{d}z = \int_0^{h_{s2}} \rho_2 A + \int_0^{h_{f2}} \rho_1 A \, \mathrm{d}z. \tag{4.13}$$

From these relationships the depths h_{s1} and h_{s2} of the hypothetical interfaces dividing the fresh and saltwater layers in each reservoir for the hypothetical state, shown

in Figure 4.1(c), become

$$h_{s1} = \frac{1}{\rho_2 - \rho_1} \int_0^{h_1'} \left(\rho_1'(z) - \rho_1\right) \mathrm{d}z \tag{4.14}$$

and

$$h_{s2} = \frac{1}{\rho_2 - \rho_1} \int_0^{h_2'} \left(\rho_2'(z) - \rho_1\right) \mathrm{d}z. \tag{4.15}$$

In addition, by assuming a linear equation of state we have $h_i' = h_{si} + h_{fi}$ (which gives constant volume). The hypothetical minimum potential energy is then given by

$$P_h = g \int_0^{h_{s1}} A\rho_2 z \,\mathrm{d}z + g \int_{h_{s1}}^{h_1'} A\rho_1 z \,\mathrm{d}z + g \int_0^{h_{s2}} A\rho_2 z \,\mathrm{d}z + g \int_{h_{s2}}^{h_2'} A\rho_1 z \,\mathrm{d}z. \tag{4.16}$$

The amount of mixing P_m is the difference in potential energies between the final state and the hypothetical non-mixing state:

$$P_m = P_f - P_h. \tag{4.17}$$

The available potential energy P_a released to the flow is the difference in potential energies between the initial state and the hypothetical non-mixing state. Thus,

$$P_a = P_i - P_h. \tag{4.18}$$

From (4.17) and (4.18) the efficiency η of mixing previously defined in (4.9) for a two-layer exchange flow can be expressed as

$$\eta = \frac{P_m}{P_a} = \frac{P_f - P_h}{P_i - P_h}. \tag{4.19}$$

4.4 Prediction of mixing efficiency

Anati *et al.* (1977) and Helfrich (1995) argued that an interfacial layer of finite thickness forms at the interface between two counter-flowing layers in an exchange flow. We adopt this argument to construct an estimate for mixing efficiency in an exchange flow through a simple contraction by assuming that the flow accelerates within the contraction until the interface between the layers becomes unstable to shear. We then argue that flow instability develops and that internal mixing creates a region of mixed layer of thickness δ, where the time-averaged vertical gradients of density and velocity are, for simplicity, assumed to be constant (see Figure 4.2).

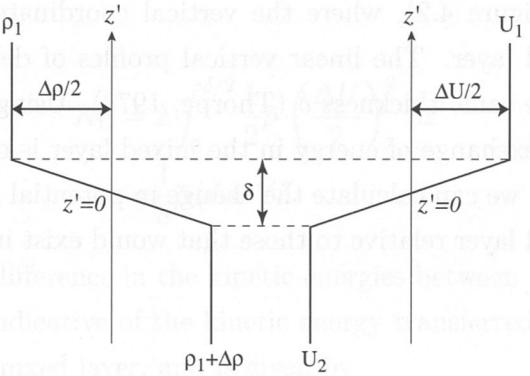

Figure 4.2: A sketch of idealised time-averaged profiles of velocity and density in the interfacial mixed region of thickness δ. The centre of the mixed region is defined to be at a height $z' = 0$.

We further argue that the interfacial mixed layer is self-regulating and characterised by a marginally stable gradient Richardson number, i.e., $Ri_g \approx Ri_{\text{crit}}$ so that, in a time-averaged sense, the overturning billows and mixing are maintained. Thus we can write

$$Ri_g = \frac{N^2}{(du/dz)^2} = \frac{g'\delta}{(\Delta U)^2} = \frac{\delta}{H} \approx Ri_{\text{crit}}, \tag{4.20}$$

where $N = (g'/\delta)^{1/2}$ and du/dz are the buoyancy frequency and velocity gradient, respectively, in the interfacial mixed layer. The velocity difference across the mixed layer is ΔU, and we have assumed that $\Delta U = (g'H)^{1/2}$ from the hydraulic solution.

Taking $Ri_g = 0.25$ based on linear stability analyses for stratified shear flows (Howard, 1961; Miles, 1961), along with (4.20), we then have $\delta/H \approx 0.25$. This value lies between $\delta/H \approx 0.2$ as discussed in Anati *et al.* (1977), based on a theoretical prediction for short straits, and $\delta/H \approx 0.3$ as used by Helfrich (1995), based on the work of Sherman *et al.* (1978) and the experimental measurements of a planar mixing layer by Koop & Browand (1979). It should be noted that the experimental configuration of Koop & Browand (1979) is different from that used here. Koop & Browand (1979) were able to set up an experiment in which mixing evolved in time and that allowed complete mixing to occur, and thus creating the possible maximum thickness of the interface. On the other hand, in the present experiments we characterise the mean thickness of the interfacial layer in a flow that is accelerating spatially, but is steady in a time-averaged sense.

We consider now a scaling analysis for the mixing efficiency in terms of the energy budgets in the interfacial mixed layer. Again, we assume that within the mixed layer the mean density and velocity vary linearly with depth so that $\rho'(z') = -\Delta\rho z'/\delta$, where $\rho'(z')$ is the perturbation of the density in the mixed region, and

$u(z') = \Delta U z'/\delta$ (Figure 4.2), where the vertical coordinate z' is centred on the middle of the mixed layer. The linear vertical profiles of density and velocity are assumed to have the same thickness δ (Thorpe, 1973). Using these definitions and supposing that the exchange of energy in the mixed layer is only between potential and kinetic energies, we can calculate the change in potential and kinetic energies of the interfacial mixed layer relative to those that would exist in an inviscid two-layer flow without mixing.

The gravitational potential energy in the density stratification of the interfacial mixed layer is given by

$$\begin{aligned} P_{\text{int}} &= \int_{-\delta/2}^{\delta/2} \rho' g z' \, \mathrm{d}z' \\ &= -\frac{1}{12} \Delta\rho g \delta^2. \end{aligned} \tag{4.21}$$

We compare P_{int} with the potential energy in the same region in the two-layer flow,

$$\begin{aligned} P_{\text{tl}} &= \int_{-\delta/2}^{0} (\rho_1 + \Delta\rho) g z' \, \mathrm{d}z' + \int_{0}^{\delta/2} \rho_1 g z' \, \mathrm{d}z' \\ &= -\frac{1}{8} \Delta\rho g \delta^2. \end{aligned} \tag{4.22}$$

Thus the increase in potential energy in the mixed layer relative to the two-layer state with no mixing is

$$\begin{aligned} \Delta P &= P_{\text{int}} - P_{\text{tl}} \\ &= \frac{1}{24} \Delta\rho g \delta^2. \end{aligned} \tag{4.23}$$

We argue that this potential energy increase is indicative of the amount of mixing due to shear instability in the exchange flow. The mean kinetic energy in the interfacial mixed layer is given by

$$\begin{aligned} K_{\text{int}} &= 2 \int_{0}^{\delta/2} \frac{1}{2} \overline{\rho} u^2 \, \mathrm{d}z' \\ &= \frac{1}{24} \overline{\rho} \, (\Delta U)^2 \delta, \end{aligned} \tag{4.24}$$

where $\overline{\rho} = (\rho_1 + \rho_2)/2$ is the mean density and we have invoked symmetry in the mixed layer. In the two-layer limit, however, the kinetic energy in the same region

is given by

$$\begin{aligned} K_{\mathrm{tl}} &= 2\int_0^{\delta/2} \frac{1}{2}\overline{\rho}\left(\frac{\Delta U}{2}\right)^2 \mathrm{d}z' \\ &= \frac{1}{8}\overline{\rho}\,(\Delta U)^2\delta. \end{aligned} \tag{4.25}$$

We assume that the difference in the kinetic energies between the ideal non-mixing and actual states is indicative of the kinetic energy transferred from the mean flow to turbulence in the mixed layer, and is given by

$$\begin{aligned} \Delta K &= K_{\mathrm{tl}} - K_{\mathrm{int}} \\ &= \frac{1}{12}\overline{\rho}\,(\Delta U)^2\delta. \end{aligned} \tag{4.26}$$

Thus we can estimate the mixing efficiency using the definition given in (4.9) as follows,

$$\begin{aligned} \eta &= \frac{\Delta P}{\Delta K} \\ &= \frac{1}{2}\frac{g'\delta}{(\Delta U)^2} \\ &= \frac{1}{2}Ri_g \\ &\approx \frac{1}{2}Ri_{\mathrm{crit}}. \end{aligned} \tag{4.27}$$

As previously mentioned, if the time-averaged gradient Richardson number tends to its critical value 0.25, our estimate of the mixing efficiency becomes $\eta \approx 0.125$. Note that the above scaling argument for the mixing efficiency is independent of channel geometry. We will further discuss this in §5.4 by comparing this theoretical prediction of the mixing efficiency with the experimental results for both the short and long constriction cases, and examining the empirical efficiency for different aspect ratios and contraction ratios. The analysis does not include the dynamics of mixing in flow features other than steady shear layers (such as hydraulic jumps at the exits from the constriction or at the base of the fall over a weir).

4.5 Prediction of mass transport

Internal hydraulic theory provides a useful tool to predict the maximal transport of water through the channel connecting reservoirs with differing fluid properties. The application of this theory to natural flows is frequently limited by excluding

the possibility of mixing and friction. However, exchange flows through topographic constrictions are subject to internal mixing between the layers and to friction at the bottom and sidewalls. Under certain circumstances these effects may play a significant role in reducing the transport.

Field observations (e.g., Bray *et al.*, 1995; Gregg & Özsoy, 2002) give evidence of the presence of an intermediate layer of finite thickness, suggesting that mixing in an exchange flow cannot be ignored, hence it should be incorporated into prediction of mass transport. The transport reduction (in the presence of mixing) has therefore been the subject of numerous studies. For example, the reduction in volume flux owing to entrainment and mixing has been estimated in numerical models (Winters & Seim, 2000; Stenström, 2003) and the reduced mass transport from the maximal hydraulic solution due to this effect has been quantified in laboratory experiments (Helfrich, 1995).

The influence of friction on topographically constrained flows over a sill has also been examined. It was found that friction shifted the hydraulic control point to a location downstream of the sill (Pratt, 1986). Bottom friction was also found to give rise to asymmetries in the interface profiles, leading to a decrease in layer thickness in the direction of the flow. Bormans & Garret (1989) applied this theoretical work to the Strait of Gibraltar and observed that interfacial friction had little influence on the exchange, but bottom friction had significant effects on the transport. Further development by Gerdes *et al.* (2002) showed that bottom friction may decrease the layer thickness in the same way as topography does, suggesting a greater reduction in the flux as a result of friction.

However, none of the above studies simultaneously estimated the magnitudes of flux reductions due to mixing and frictional effects in a hydraulically controlled exchange flow. We here attempt to separate the flux reductions owing to both effects. In the special case of flow through a pure, short constriction with no barotropic component the flow is symmetric about the mid-point (narrowest section) of the constriction and both the topographic and virtual control points coalesce at only the single control point, which is positioned at the narrowest. For this simple geometry we write the net mass transport normalised by the ideal maximal flux (2.21) as

$$M = 1 - M_{\text{mix}} - M_{\text{fri}}, \tag{4.28}$$

where M_{mix} is the fractional transport reduction owing to interfacial mixing and M_{fri} is the fractional transport reduction owing to bottom and sidewall friction, respectively.

Following Hogg *et al.* (2001*a*) and writing the hydraulic prediction for maximal exchange per unit width as $\mathcal{M}_{\max} = 0.25\Delta\rho\Delta U H$, we perform a simple integration of horizontal mass flux over the depth of the mixed layer (Figure 4.2), and express the normalised transport reduction due to mixing as

$$\begin{aligned} M_{\text{mix}} &= \frac{\int_{H/2}^{(H+\delta)/2} \big(\rho(z) - \rho_1\big)\big(u(z) - U_1\big)\,\mathrm{d}z}{0.25\Delta\rho\Delta U H} \\ &= 2\delta/3H \\ &\approx 0.167, \end{aligned} \tag{4.29}$$

so that the total normalised transport (4.28) becomes

$$M \approx 0.833 - M_{\text{fri}}. \tag{4.30}$$

The influence of mixing on hydraulically controlled exchange flows through a simple contraction is thus predicted to be independent of flow conditions. The magnitude of M_{fri} is expected to depend on the length L_c and width $b(x)$ of the constriction. Here we propose that it depends upon a geometric 'effective width' b_{ef} of the constriction and the cross-sectional area (in a vertical cross-stream plane) taken up by a boundary layer (along the bottom and sidewalls) of thickness $\sigma \sim (\nu\ell/U)^{1/2}$, where ℓ is the alongstream lengthscale and U is the characteristic speed (Prandtl, 1952). We define an effective width b_{ef} of the constriction as the average over the total length of the constriction such that

$$b_{\text{ef}} = \frac{1}{L_c}\int_{-L_c/2}^{L_c/2} b(x)\,\mathrm{d}x. \tag{4.31}$$

This effective width is used to calculate the dimensional mass reduction Φ_{fri}, owing to frictional effects at the bottom and sidewalls defined as

$$\Phi_{\text{fri}} = \sigma\Delta\rho U L_{\text{fri}}, \tag{4.32}$$

where $U = 0.5(g'H)^{1/2}$ is the flow speed and $L_{\text{fri}} = 2H + b_{\text{ef}}$ is the total length of the area in which friction takes place. The fractional mass reduction owing to friction can be obtained by normalising (4.32) with the hydraulic, ideal maximal transport given in (2.21). The normalised frictional reduction M_{fri} can then be estimated as

$$M_{\text{fri}} \sim Re^{-1/2}\left(2\frac{L_c}{b_{\text{ef}}} + \frac{L_c}{H}\right). \tag{4.33}$$

For a given water depth H the transport reduction due to bottom and sidewall

friction is then weakly dependent on the Reynolds number Re, but is proportional to the constriction length L_c and inversely proportional to the effective width b_{ef} of the constriction. We will further discuss this in §5.6 by comparing this theoretical prediction of the mass transport with the experimental results for both the short and long constriction cases, and examining the role of the constriction shape in the exchange.

Chapter 5

Results: Exchange flows through constrictions

5.1 Qualitative observations

Each experiment was initiated by removing a vertical sliding barrier separating the reservoirs of dense and less dense water. Gravity currents with a characteristic head structure (Simpson, 1997) developed after the removal of the barrier, with the dense water flowing to the left and the less dense water flowing to the right (Figure 5.1*a*). The subsequent density-driven exchange flow led to shear instability, a turbulent interfacial layer and extensive mixing, particularly in the vicinity of the contraction (Figure 5.1*b*). Hydraulic jumps occured near the exits of the contraction (Figure 5.1*c*). By frame (*c*) of Figure 5.1, the flow in the constriction had reached a steady mean state. At the early stages of an experiment (Figure 5.1*a*, *b* and *c*), there was an asymmetrical shape between the dense current propagating along the base of the tank and the light current propagating near the surface. This minor asymmetry was a transient character owing to the withdrawal of the barrier, where some initial exchange near the channel base occurred before lateral flow moved to the right near the surface. Such an asymmetry became less obvious as the currents developed (Figure 5.1*d*, *e*).

Kelvin-Helmholtz (KH) billows continuously grew on the strongly sheared and turbulent interface within the contraction (Figure 5.1*d*, *e*), generating overturns and vertical mixing. Each billow grew to a large amplitude (Figure 5.1*e*) as it was carried away from the centre of the constriction and collapsed near the exit from the contraction. The resulting mixed fluid was advected away from the constriction as a part of the gravity current flow (Figure 5.2*a*). There were no persistent billows or large overturning along the density gradient region above the gravity currents

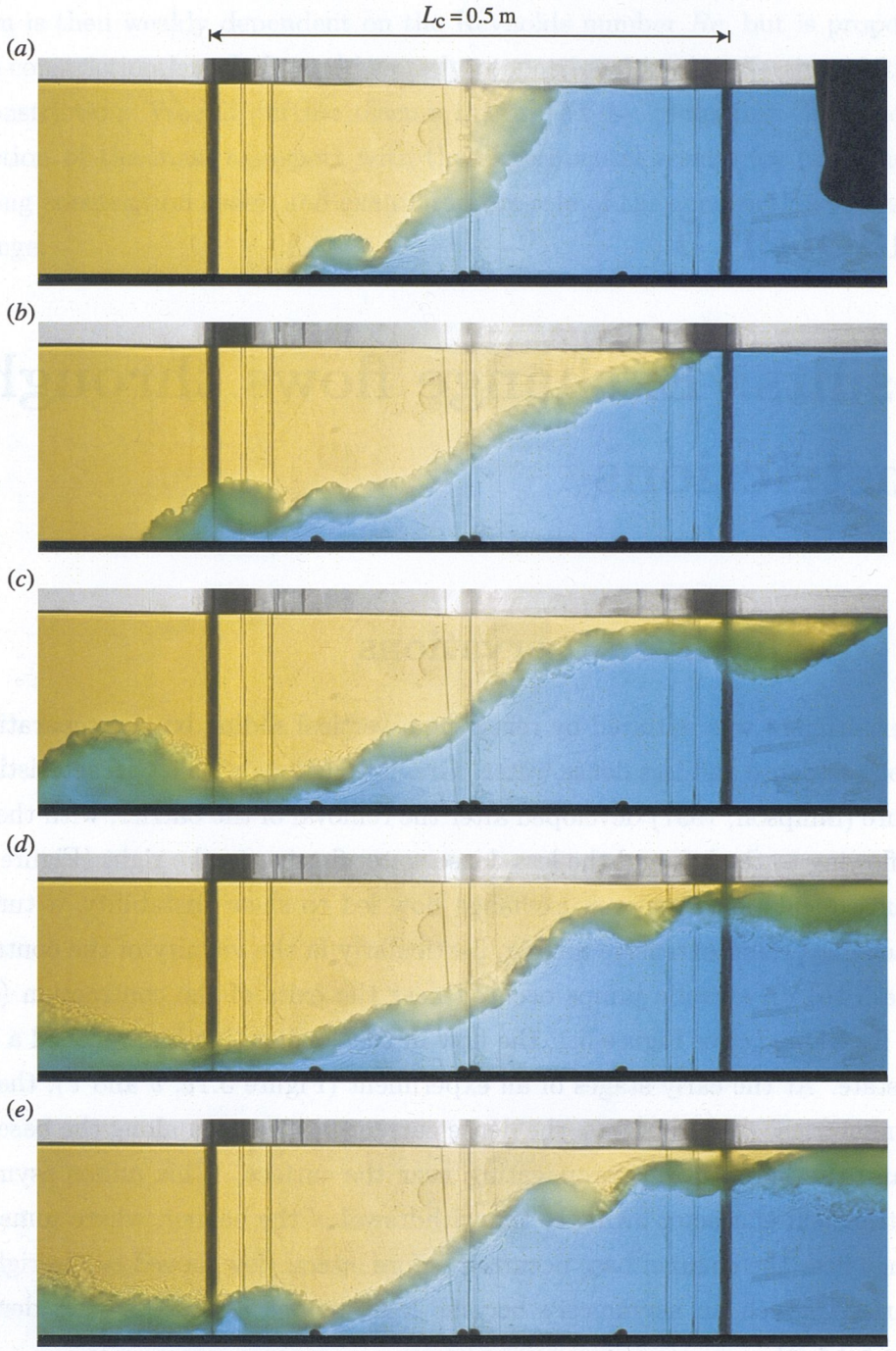

Figure 5.1: A series of photographs showing various stages of an experiment using the short constriction with $b_o = 60$ mm, $\Delta\rho/\rho_2 = 4.8\%$, $H = 0.2$ m and $Re = 7.7 \times 10^4$ (data are not included in Table 3.1). Only the flow within the constriction is shown. Note that two dark vertical lines mark the exits of the constriction. Frames (a) through (e) were taken at about 1.2, 2.2, 3.2, 6.2 and 10.2 seconds after the barrier was withdrawn.

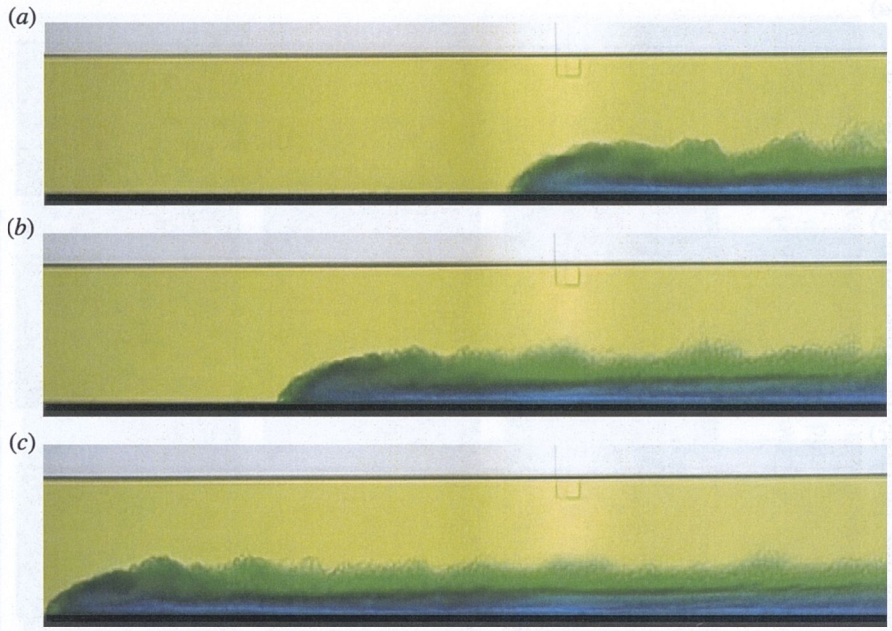

Figure 5.2: Propagating gravity current in the reservoir from experiment $H6$ (Table 3.2) with $b_o = 60$ mm, $\Delta\rho/\rho_2 = 6.7\%$, $H = 0.2$ m and $Re = 18 \times 10^4$. Frames (a) through (c) were taken at an interval of approximately 2.8 seconds.

(Figure 5.2b), apart from the billows on the head of the gravity currents. The exchange flow was effectively stopped as the barrier was rapidly reinserted into the centre of the constriction at a time when the gravity current noses had nearly reached the endwalls (Figure 5.2c). Thus throughout the exchange the mean flow was expected to be in an approximately steady state, and the distant endwalls could have no influence on the flow within the constriction.

After the barrier was replaced the gravity currents were reflected from the far ends of the reservoirs to form large-amplitude waves (Figure 5.3a), which propagated towards the replaced barrier in the constriction (Figure 5.3b). The reflection process produced some additional mixing, but this is argued to be small (see §5.3 for details). Prior to reaching the barrier these waves took the form of internal bores, where some minor mixing, with relatively small amount, occurred at points further downstream of these bores. The bores were eventually reflected back from the barrier, resulting in relatively more smooth interfaces with undulations travelling one after another (Figure 5.3c, d). After the later reflections from the endwalls a complex pattern of wave-wave interactions was observed in each reservoir.

There were no qualitative differences in the flow for all cases where the Reynolds number was sufficiently large. Continuous small-scale turbulence at the sheared interface within the constriction was the dominant feature in these cases. This is

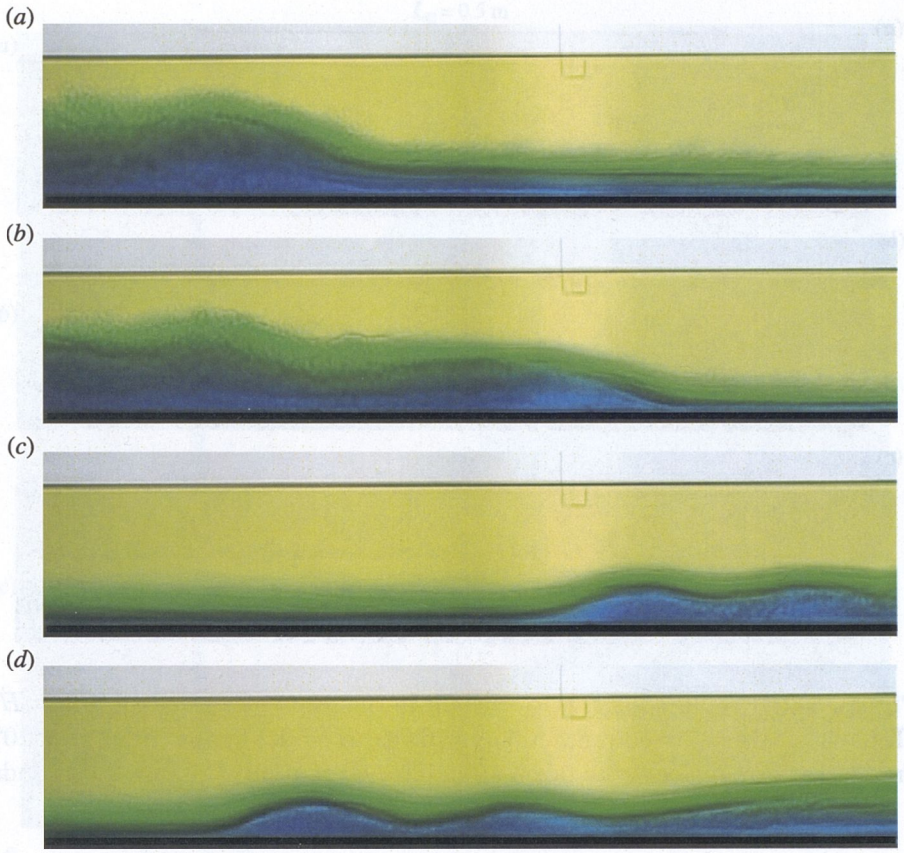

Figure 5.3: Propagating internal bore from experiment $H6$ (Table 3.2) with $b_o = 60$ mm, $\Delta\rho/\rho_2 = 6.7\%$, $H = 0.2$ m and $Re = 18 \times 10^4$. Frames (a) and (b) were taken after the first reflection of the gravity current from the endwall. Frames (c) and (d) were taken when the bore moved away from the replaced barrier (after the first reflection from the barrier).

illustrated by the two experiments having different density contrasts shown in Figure 5.4, and by the two experiments having different constriction geometries shown in Figure 5.5. The flows in Figure 5.4 were very similar with the same steepness of the interface. The interface in a narrow constriction (Figure 5.5f) had approximately the same slope as in a wider constriction (Figure 5.5c). Likewise, the turbulence had the same appearance within the contraction, independent of the constriction width. Naturally, the larger minimum width b_o accommodated a greater mass flux, resulting in deeper gravity currents in the reservoirs. Hence, for a larger b_o a larger proportion of the reservoir volumes had exchanged by the time the currents reached the endwalls.

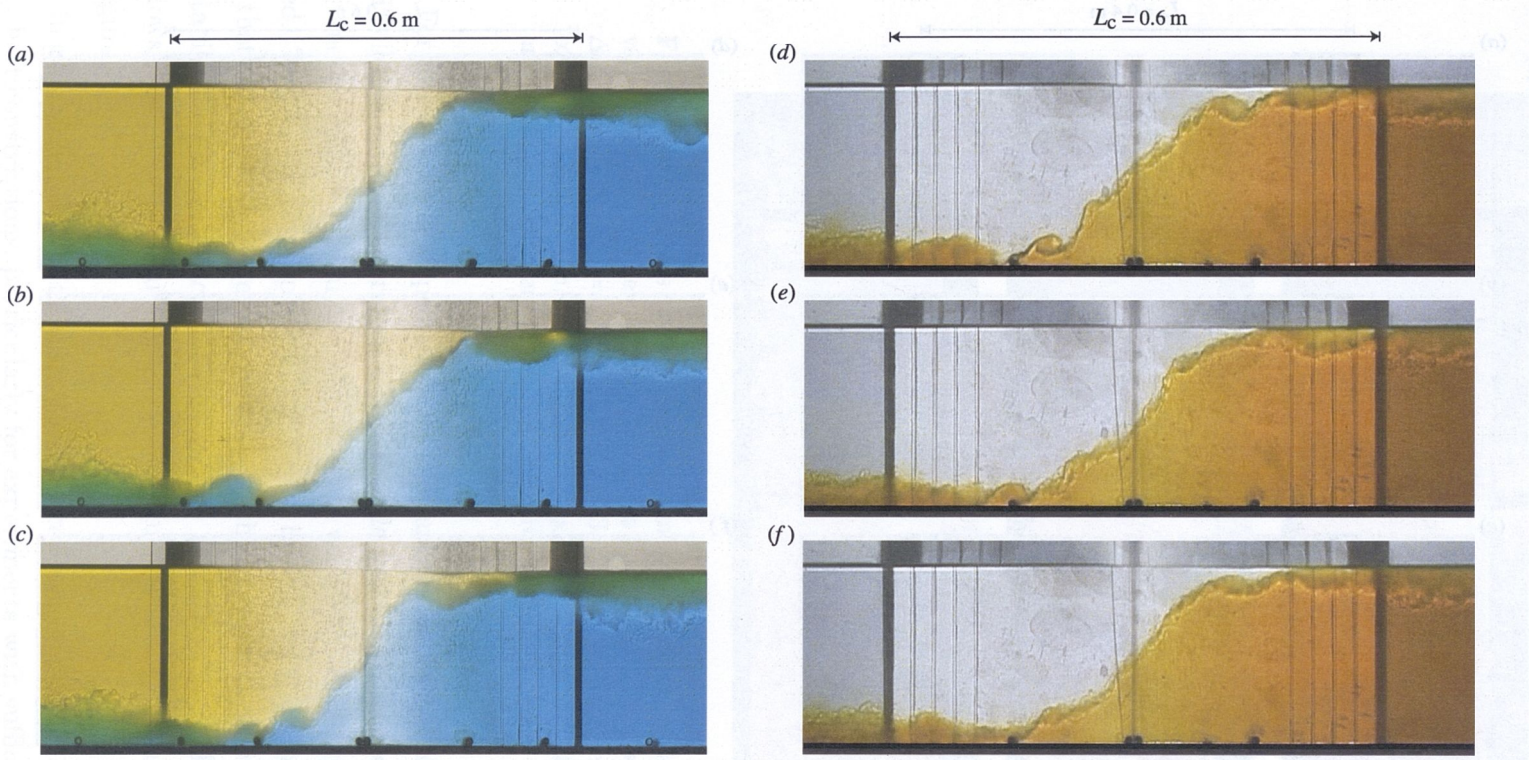

Figure 5.4: Two experiments E2 and E8 (Table 3.1) using the short constriction with the same b_o (20 mm) and H (0.2 m), but with different $\Delta\rho/\rho_2$. Frames (a) through (c), from experiment E2 having $\Delta\rho/\rho_2 = 6.7\%$ and $Re = 11.3 \times 10^4$, were taken at about 5.2, 9.2 and 13.2 seconds after the barrier was withdrawn. Frames (d) through (f), from experiment E8 having $\Delta\rho/\rho_2 = 2.4\%$ and $Re = 6.6 \times 10^4$, were taken at about 10.2, 20.2 and 30.2 seconds after the barrier was withdrawn. Note that a steady-state exchange had been achieved by frame (a) or (d) for each case.

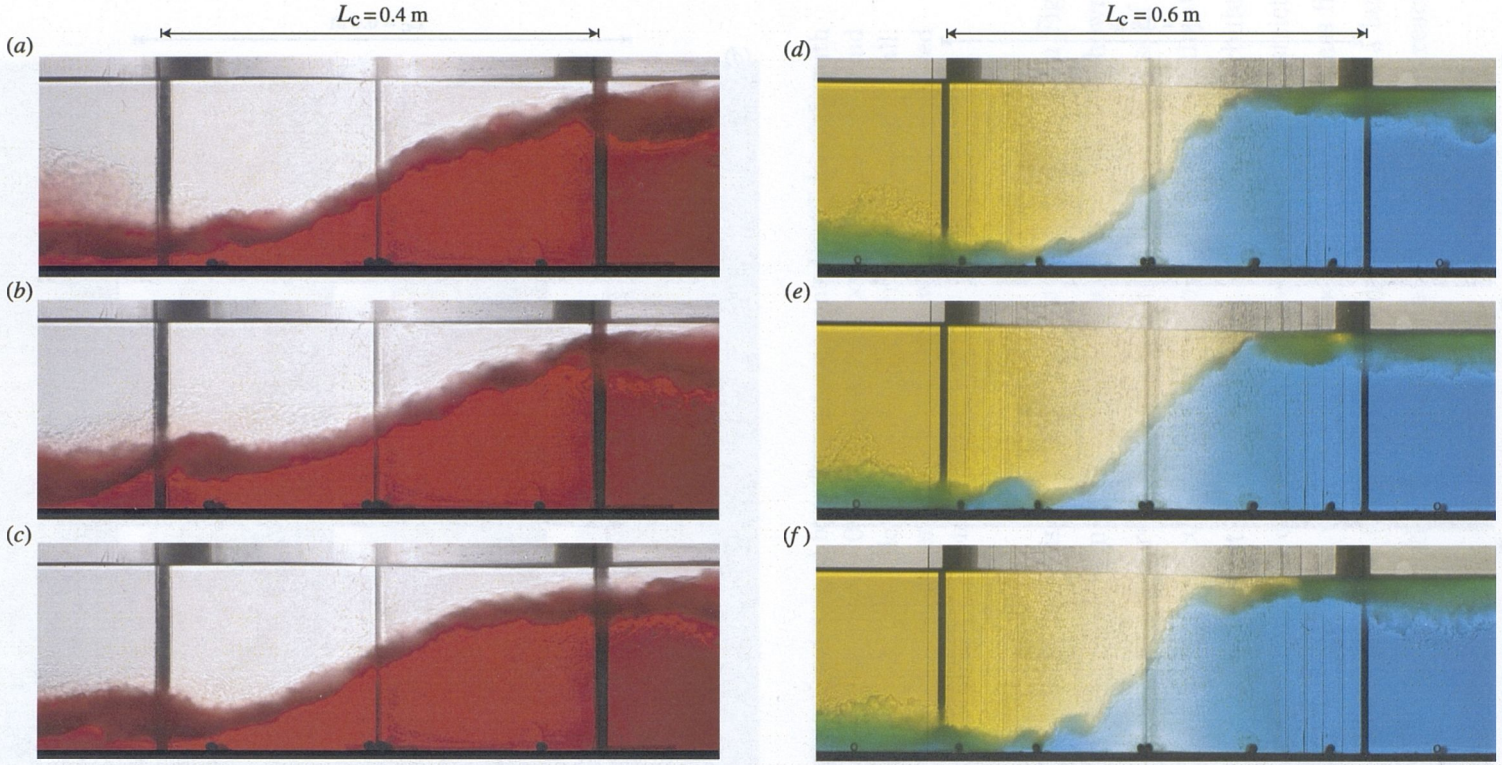

Figure 5.5: Two experiments F6 and E2 (Table 3.1) using the short constriction with the same H (0.2 m) and $\Delta\rho/\rho_2 = 6.7\%$, but with different constriction geometries. Frames (a) through (c), from experiment F6 having $b_o = 100$ mm and $Re = 7.2 \times 10^4$, were taken at about 5.1, 8.1 and 10.1 seconds after the barrier was withdrawn. Frames (d) through (f), from experiment E2 having $b_o = 20$ mm and $Re = 11.3 \times 10^4$, were taken at about 5.2, 9.2 and 13.2 seconds after the barrier was withdrawn. Note that a steady-state exchange had been achieved by frame (a) or (d) for each case.

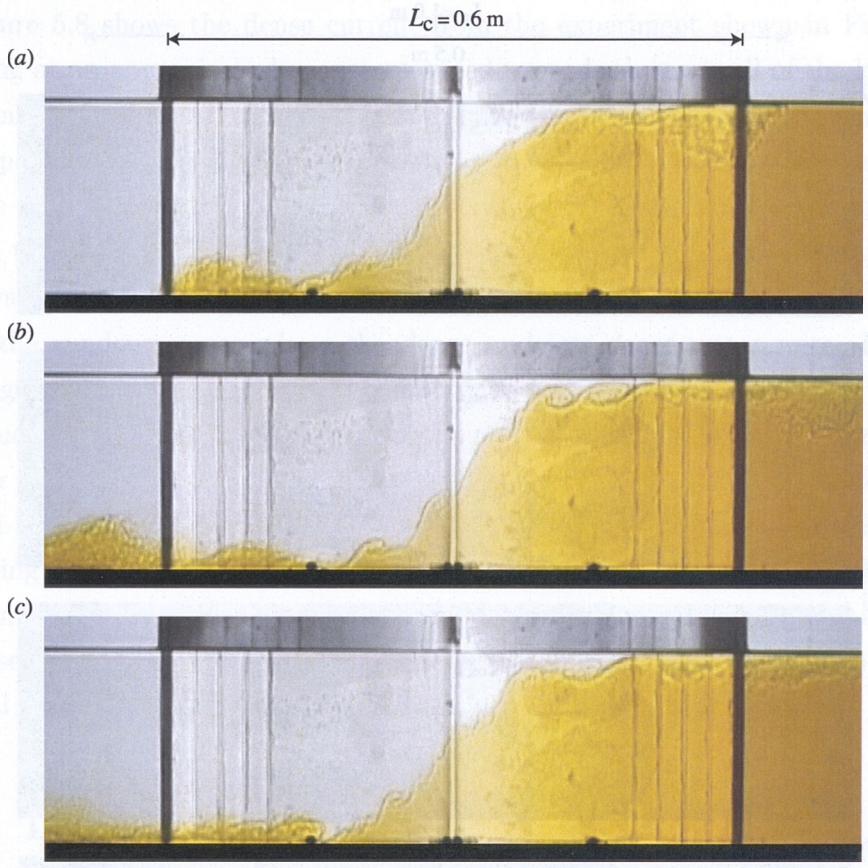

Figure 5.6: A series of photographs from experiment A8 (Table 3.1) showing various stages of the experiment using the short constriction with $b_o = 20$ mm, $\Delta\rho/\rho_2 = 0.7\%$, $H = 0.2$ m and $Re = 3.5 \times 10^4$. Only the flow within the constriction is shown. Frames (a) through (c) were taken at about 8.1, 12.9 and 17.3 seconds after the barrier was withdrawn.

For a given water depth there was a qualitative difference in the formation of KH billows and the generation of small-scale turbulence between experiments with low and high Reynolds numbers, associated with small and large density differences used. The initial development of the flow in the low Re experiments was similar to that in the high Re experiments. In the experiments with low Re the shear instability at the interface appeared to be relatively weak (Figure 5.6a) and the billows were only intermittent with consequently weak mixing between the layers (Figure 5.6b, c).

In general the flow in the long constriction case showed the same behaviour as in the short constrictions, particularly for experiments with sufficiently large Reynolds numbers (Figure 5.7). Once the barrier was withdrawn the characteristic head of the dense current developed (Figure 5.7a), and then propagated along the channel

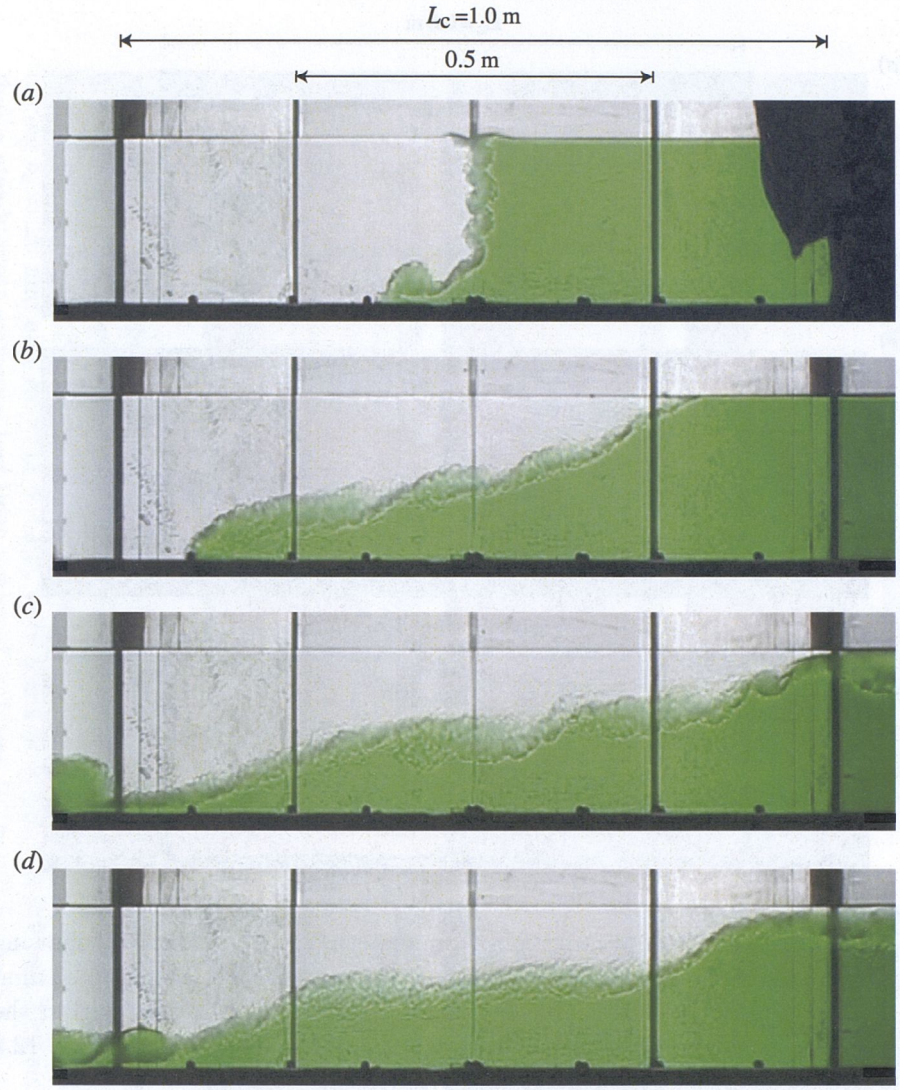

Figure 5.7: A series of photographs from experiment H4 (Table 3.2) showing various stages of the experiment using the long constriction with $b_o = 60$ mm, $\Delta\rho/\rho_2 = 3.0\%$, $H = 0.2$ m and $Re = 12 \times 10^4$. Only the flow within the constriction is shown. Note that two inner-dark vertical lines mark the ends of the constriction central section, while the other two outer-dark vertical lines mark the exits of the constriction. Frames (a) through (e) were taken at about 1.1, 3.5, 6.3 and 11.6 seconds after the barrier was withdrawn.

base with the less dense current propagating in the opposite direction along the surface (Figure 5.7b). The hydraulic jumps seemed to occur near the exits of the constriction (Figure 5.7c). As the flow experienced changes in width only at the exit regions of this constriction, the acceleration of the flow was greater in these regions and hence the interface slope was larger (Figure 5.7d). However, there was a significant interface slope along the straight central section.

Figure 5.8 shows the dense current from the experiment shown in Figure 5.7, traveling at an approximately constant speed towards the endwall of the long tank. Some interfacial mixing was observed to take place above the current head and at the upper surface of the trailing current as it propagated along the channel base (Figure 5.8*a* through *d*), although this mixing was visibly much less intense than that in the vicinity of the constriction. It was also observed that the shape of the head was maintained during the propagation of the current.

In the rundown cases where the dense and less dense water were allowed to exchange all the time, the flow was complicated, particularly at times after the large amplitude waves were reflected back from the endwalls and reached the constriction to alter the exchange flow (Figure 5.9*a*). The exchange was then characterised by a multi-layered flow (Figure 5.9*b*), with shear instability and the associated billows appearing at more than just a single interfacial mixing region (Figure 5.9*c*). At late times in which all motions almost die away, the multi layered flow was achieved and the observed layers at both the surface and the bottom were found to have their original densities unaltered (Figure 5.9*d*).

5.2 Density profiles

Examples of the density profiles from both the left and right reservoirs, measured at the end of an experiment using a short constriction, are plotted in Figure 5.10, where the measured density is normalised by $(\rho(z) - \rho_1)/(\rho_2 - \rho_1)$. As mentioned in §3.2, these density profiles were measured from each reservoir using the sampling tubes spaced vertically at 1 cm intervals throughout the water depth. The same spatial resolution of the sampled density was used in all experiments with different geometries and external parameters. Figure 5.10(*a*, *b*) show the density profiles of three experiments for different constriction minimum widths using the same experimental run time t_r (59 $\pm$ 1 s) and all other variables. The mass transport is found to be greater in experiments with wider constrictions (Figure 5.10*a*, *b*; as expected from the hydraulic solution). Figure 5.10(*c*, *d*) show the density profiles of four experiments for different fractional density differences using the same constriction minimum width b_o (20 mm) and full water depth H (0.2 m). The experimental run times before the currents reached the endwalls in these experiments were 88, 49, 37 and 29 seconds, respectively. From the similar profiles we conclude that, to first order, the net mass transport between the reservoirs scales with the hydraulic prediction (2.21). Small differences in the profile shapes in Figure 5.10(*c*, *d*) reflect a dependence of billow formation and interfacial mixing on Reynolds number in low

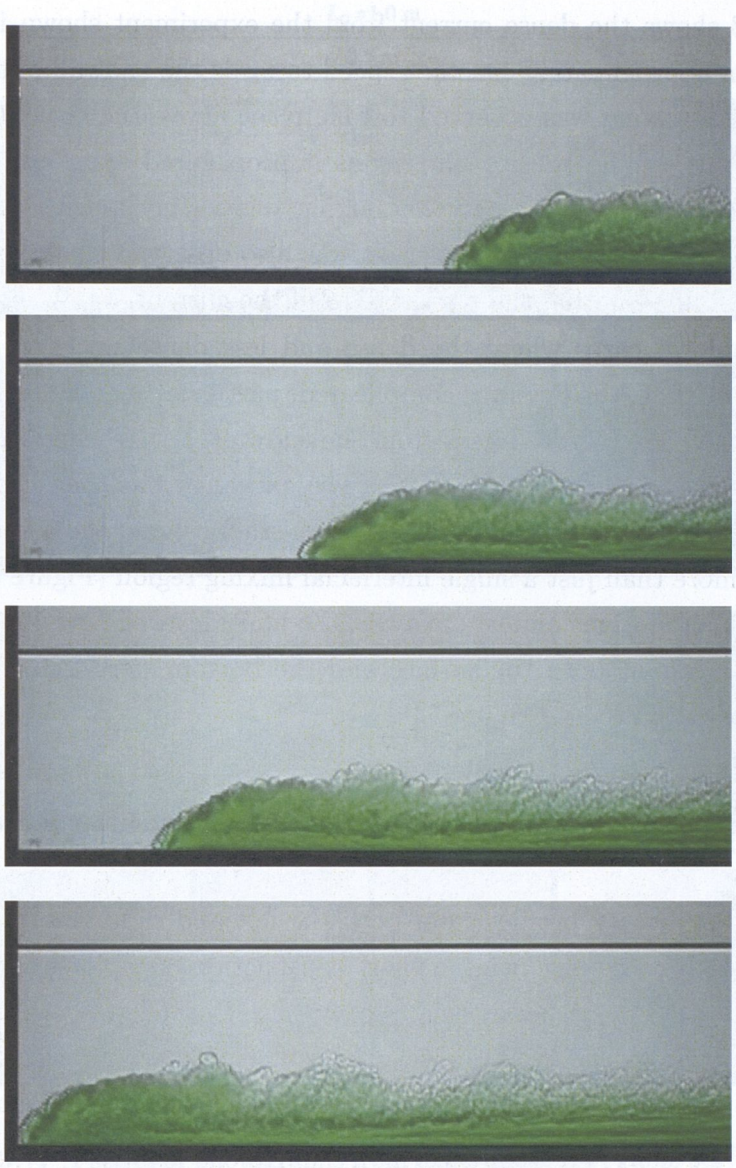

Figure 5.8: Propagating gravity current towards the channel endwall from experiment H4 (Table 3.2) with $b_o = 60$ mm, $\Delta\rho/\rho_2 = 3.0\%$, $H = 0.2$ m and $Re = 12 \times 10^4$. Frames (a) through (d) were taken at an interval of approximately 1.8 seconds. Frame (d) shows the nose of the current reaching the endwall at approximately 30 seconds after the removal of the barrier.

Reynolds number experiments (examined further in §5.3).

Examples of final density profiles from both the left and right reservoirs for experiments with the long constriction are plotted in Figure 5.11, for four cases having different fractional density differences but the same constriction minimum width b_o (60 mm) and total water depth H (0.2 m). The experimental run times in these experiments were again such that the total volume exchanged was similar. As

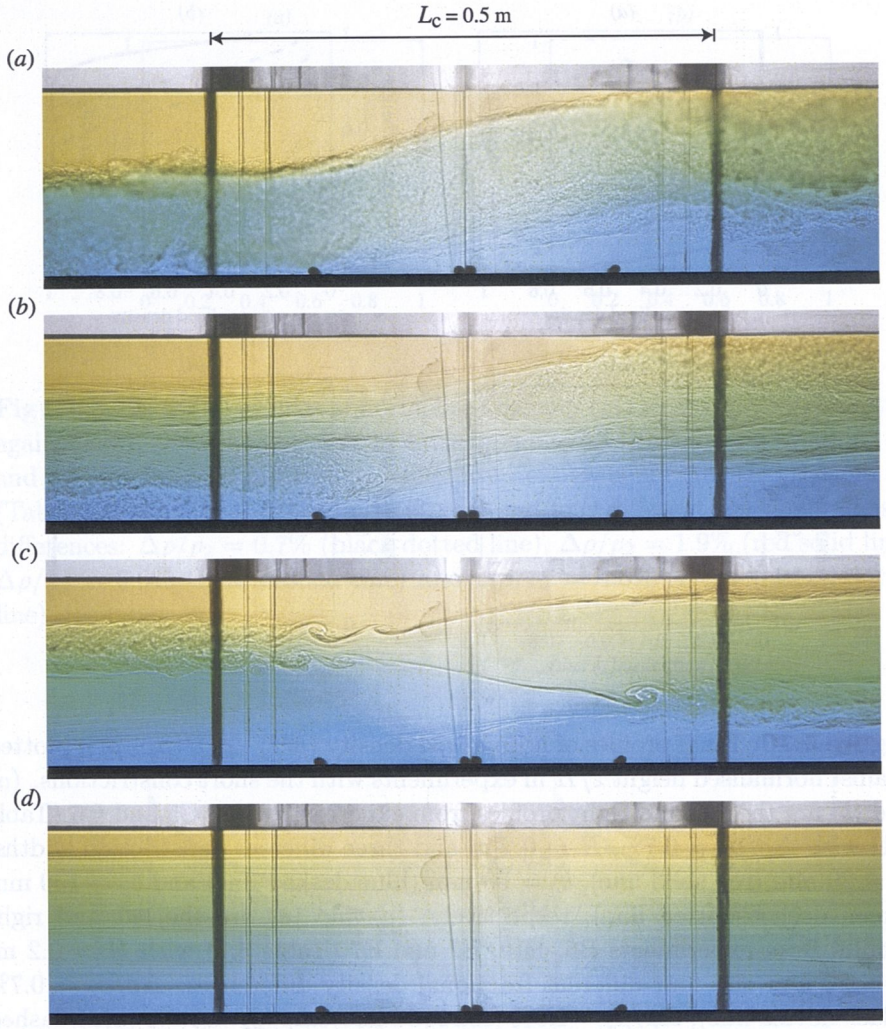

Figure 5.9: Flow in the rundown experiment, using the short constriction with $b_o = 60$ mm, $\Delta\rho/\rho_2 = 4.8\%$, $H = 0.2$ m and $Re = 7.9 \times 10^4$ (data are not included in Table 3.1). Frames (*a*) through (*d*) were taken at about 57.5, 82.5, 120.5 and 262.5 seconds after the barrier was withdrawn.

for the short constrictions, the normalised profiles are indistinguishable from each other. We conclude that the mixing is dynamically similar across these conditions, with the rate of mixing being proportional to $(\Delta\rho/\rho_2)^{1/2}$.

In addition to the above density profiles, we provide final density profiles from the reservoir for rundown cases (described in §3.3.4) using the short constriction with various fractional density differences and constriction minimum widths. These profiles, plotted in Figure 5.12, show that the mixing region spread out the water depth and occupied more than 60% of the full depth. There is no significant differences in the profile shapes between experiments with the same water depth

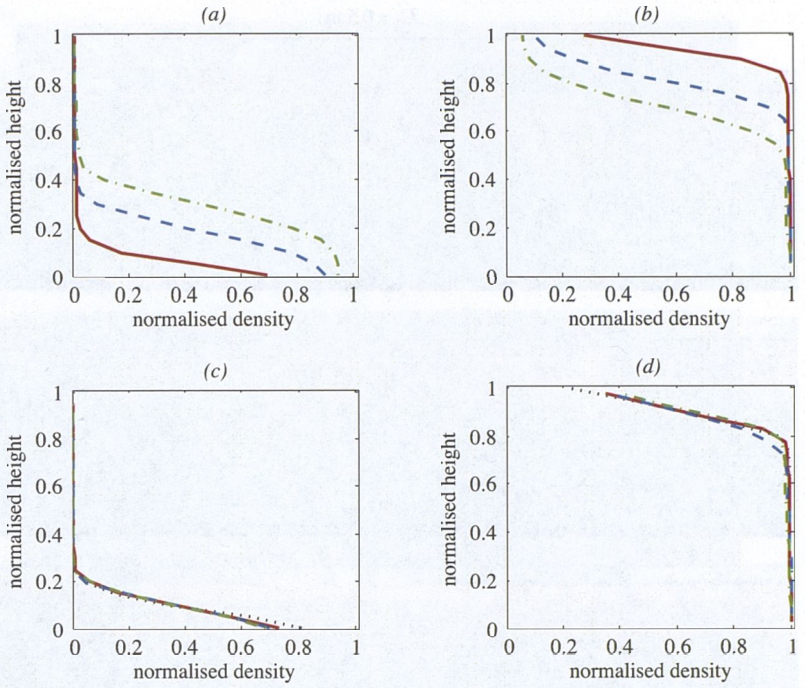

Figure 5.10: Final profiles of normalised density $(\rho(z)-\rho_1)/(\rho_2-\rho_1)$, plotted against normalised height z/H in experiments with the short constrictions. (a) and (b) are the left and right profiles from experiments A8, C5 and C6 (Table 3.1) with $\Delta\rho/\rho_2 = 0.7\%$, $H = 0.2$ m and three different constriction widths: $b_o = 20$ mm (red solid line), $b_o = 60$ mm (blue dashed line) and $b_o = 100$ mm (green dashed-dotted line), respectively; (c) and (d) are the left and right profiles from experiments B6, E16, E1 and E7 (Table 3.1) with $H = 0.2$ m, $b_o = 20$ mm and four different fractional density differences: $\Delta\rho/\rho_2 = 0.7\%$ (black dotted line), $\Delta\rho/\rho_2 = 1.9\%$ (red solid line), $\Delta\rho/\rho_2 = 3.1\%$ (blue dashed line) and $\Delta\rho/\rho_2 = 4.8\%$ (green dashed-dotted line), respectively.

($H = 0.2$ m) and constriction minimum width ($b_o = 20$ mm) but different fractional density differences (Figure 5.12a). The profile shapes were also similar for experiments with again the same water depth ($H = 0.2$ m) and fractional density difference ($\Delta\rho/\rho_2 = 4.8\%$) but different constriction minimum widths (Figure 5.12b). These suggest that mixing processes in the rundown cases were dynamically similar, independent of external parameter and constriction geometry.

5.3 Mixing efficiency

We observed several mechanisms for mixing in these experiments. The most intense mixing was observed in the contraction, and took place over the length of the

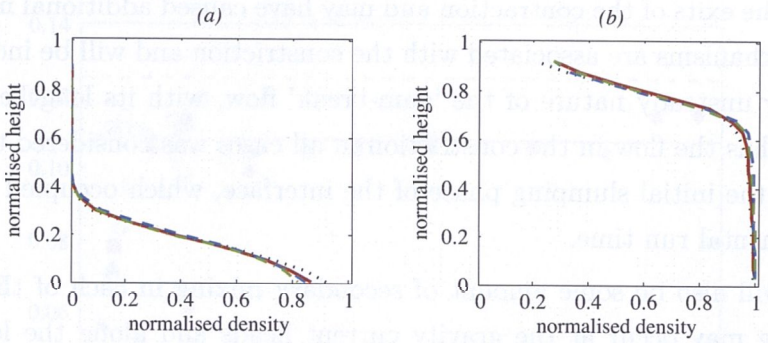

Figure 5.11: Final profiles of normalised density $(\rho(z)-\rho_1)/(\rho_2-\rho_1)$, plotted against normalised height z/H in experiments with the long constriction. (a) and (b) are the left and right profiles from experiments H8, H3, H4 and H5 (Table 3.2) with $H = 0.2$ m, $b_o = 60$ mm and four different fractional density differences: $\Delta\rho/\rho_2 = 0.7\%$ (black dotted line), $\Delta\rho/\rho_2 = 1.9\%$ (red solid line), $\Delta\rho/\rho_2 = 3.0\%$ (blue dashed line) and $\Delta\rho/\rho_2 = 4.8\%$ (green dashed-dotted line), respectively.

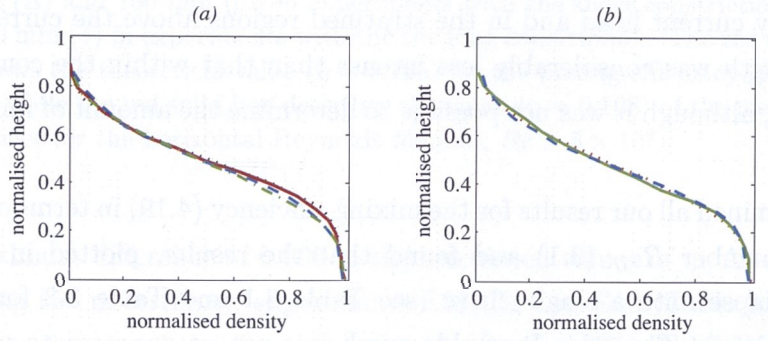

Figure 5.12: Final profiles of normalised density $(\rho(z)-\rho_1)/(\rho_2-\rho_1)$, plotted against normalised height z/H in the rundown cases using the short constriction with $H = 0.2$ m. (a) are the profiles from experiments R1, R2, R3 and R4 (Table 3.7) with $b_o = 20$ mm and four different fractional density differences: $\Delta\rho/\rho_2 = 0.7\%$ (black dotted line), $\Delta\rho/\rho_2 = 1.9\%$ (red solid line), $\Delta\rho/\rho_2 = 3.0\%$ (blue dashed line) and $\Delta\rho/\rho_2 = 4.8\%$ (green dashed-dotted line), respectively; (b) are the profiles from experiments R4, R6 and R7 (Table 3.7) with $\Delta\rho/\rho_2 = 4.8\%$ and three different constriction widths: $b_o = 20$ mm (red dotted line), $b_o = 60$ mm (green solid line) and $b_o = 100$ mm (blue dashed line), respectively.

contraction, where the flow was subject to acceleration. In this region small-scale turbulence occupied an interfacial layer of finite thickness, being overturned by large billows having amplitude about 1/4 of the total water depth. Hydraulic jumps could

be seen at the exits of the contraction and may have caused additional mixing. Both of these mechanisms are associated with the constriction and will be independent of the globally unsteady nature of the 'dam-break' flow, with its lengthening gravity currents. Thus the flow in the constriction in all cases was considered to be steady, apart from the initial slumping phase of the interface, which occupied only 10% of the experimental run time.

There will also be some amount of secondary mixing in each of the reservoirs. This mixing may occur at the gravity current heads and along the length of the trailing currents, where a relatively weak shear instability was possible. Mixing also occurred after the barrier was replaced, as a result of the reflection of the gravity currents at the far ends of the reservoirs, a later reflection of large amplitude gravity waves from the barrier, and subsequent minor wave-related mixing events during the decay of motions throughout the tank. The experiments provided an interpreted measure of all mixing consequent on the exchange flow in a finite volume. In addition, we will later show from the data that only insignificant amounts of mixing occurred after the barrier was replaced. It was also clear that mixing behind each gravity current head and in the stratified regions above the current along the channel length was considerably less intense than that within the contraction (see Figure 5.8), although it was not possible to determine the amount of mixing in those regions.

We examined all our results for the mixing efficiency (4.19) in terms of the vertical Reynolds number Re_H (3.1) and found that the results, plotted in Figure 5.13, do not collapse onto a single curve (see Table 3.1 and Table 3.2 for a listing of flow conditions). Thus this Reynolds number is not an appropriate parameter for this flow. Rather, the parameter found to collapse the mixing efficiency η in these experiments is the horizontal Reynolds number Re based on L_c (3.2), for which the data for different $\Delta\rho/\rho_2$, b_o and L_c collapse to a single curve. The results based on this horizontal Reynolds number are plotted in Figure 5.14, and reveal no significant differences for different constriction minimum widths b_o, constriction lengths L_c and water depths H, suggesting no dependence of mixing efficiency upon the constriction geometry, or the aspect ratios H/L_c and b_o/B. Note that for large Reynolds numbers there is no variation of η with any parameter and it has the value $\eta = 0.108$, with the standard deviation of 0.005 for $Re \gtrsim 5 \times 10^4$.

The uncertainties in the measurements of mixing efficiency were further examined. We compared the results from three experiments (B2, E7 and E9 in Table 3.1), having the same flow variables but different initial conditions: equal bottom pressures in B2, equal surface heights in E7 and equal pressures at mid-depth in E9, and

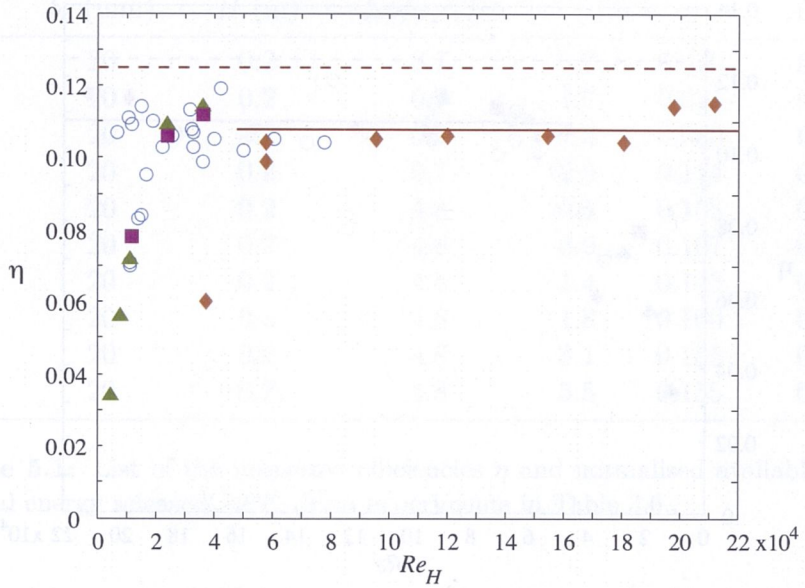

Figure 5.13: The measured mixing efficiencies η as a function of the vertical Reynolds number Re_H for all experiments. Symbols indicate $b_o = 20$ mm ($\circ$), 60 mm ($\triangle$) and 100 mm ($\square$) in experiments with the short constrictions and $b_o = 60$ mm ($\diamond$) in experiments with the the long constriction. The red dashed line shows the theoretical value ($\eta \approx 0.125$) for the mixing efficiency given by (4.27), while the red solid line describes the mean ($\eta = 0.108$) of the measured efficiencies for the horizontal Reynolds number, $Re > 5 \times 10^4$.

found a maximum difference of 0.006 in the calculated values of η. As another test for estimating the uncertainty, experiments E13, B3 and E10 (Table 3.1) were run with the same fractional density difference ($\Delta\rho/\rho_2 = 4.8\%$) and initial condition (equal pressures at the bottom) but different run times (44, 15 and 24 seconds) and water depths (0.1 m, 0.2 m and 0.3 m), and again the measured efficiencies lay within 0.006 of each other. Hence, we conclude that it is appropriate to quote the mixing efficiency for experiments with $Re \gtrsim 5 \times 10^4$ as $\eta = 0.11 \pm 0.01$, where the uncertainty is twice the standard deviation for all such runs. However, at the smaller Re the mixing efficiency was smaller and corresponded to the observation of less small-scale turbulence and only intermittent billows under these conditions.

Apart from Reynolds numbers another parameter examined in the experiments was the experimental run time, t_r. In most cases this was slightly less than the time t_g (defined in §3.3.4), taken for the gravity currents to travel from the exits of the constriction to reach the endwalls. We examined time-dependence of mixing by carrying out experiments with the same constriction minimum width ($b_o = 20$ mm) and water depth ($H = 0.2$ m) but different fractional density differences

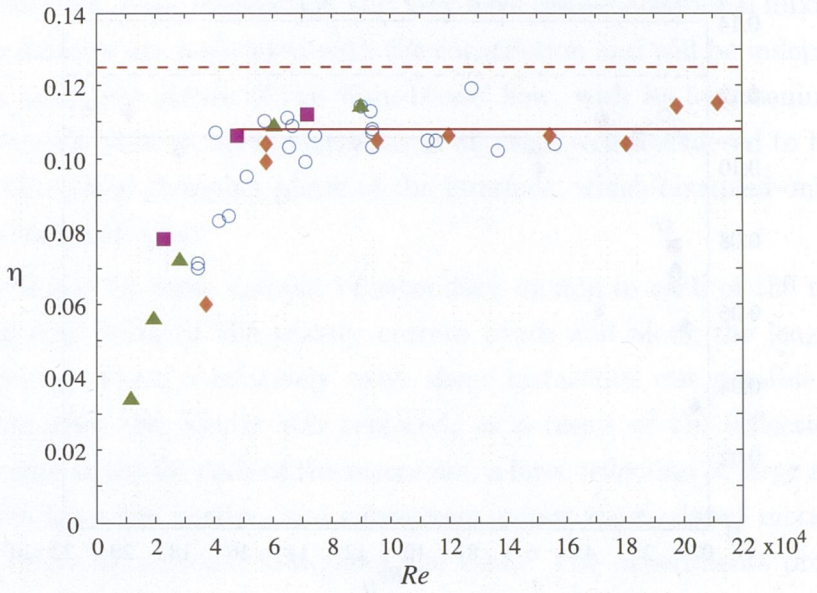

Figure 5.14: The measured mixing efficiencies η as a function of the horizontal Reynolds number Re for all experiments. Symbols indicate $b_o = 20$ mm ($\circ$), 60 mm ($\triangle$) and 100 mm ($\square$) in experiments with the short constrictions and $b_o = 60$ mm ($\diamond$) in experiments with the the long constriction. The red dashed line shows the theoretical value ($\eta \approx 0.125$) for the mixing efficiency given by (4.27), while the red solid line describes the mean ($\eta = 0.108$) of the measured efficiencies for $Re > 5 \times 10^4$.

and dimensionless run times τ (defined in §3.3.4). Here, we define the normalised available potential energy released as $APE_r = P_a/P_t$, where P_a is the available potential energy released to the mean flow (4.18) and P_t is the total available potential energy, which is the difference between the initial potential energy P_i (4.10) and the potential energy that would exist if mixing were not to occur. Note that the total available potential energy corresponds to the idealised, non-mixing configuration of two-layer fluids with the saltwater underlying the freshwater in the reservoir after the experiment.

The results of the above experiments are summarised in Table 5.1. We plot the results for the mixing efficiency in Figure 5.15 and for the normalised available potential energy in Figure 5.16. It is clear from Figure 5.15 that for experiments with $\tau \leq 1.0$ the mixing efficiency is about the same in each case. These confirm that the rate of mixing was constant for the steady exchange flow and also confirm the contention that mixing associated with the starting and ending of the exchange flow by lifting and replacing the barrier had no significant contributions to the overall amount mixing. Using the data in Table 3.1 and a constant c for each constriction geometry (discussed in §3.3.4) we estimate that, for the case of the

Exp	b_o (mm)	H (m)	$\Delta\rho/\rho_2$ (%)	τ	η	APE_r
A8	20	0.2	0.7	0.7	0.070	0.29
B6	20	0.2	0.7	1.0	0.071	0.36
B5	20	0.2	0.7	1.3	0.080	0.49
B4	20	0.2	0.7	2.0	0.114	0.66
B3	20	0.2	4.8	0.5	0.103	0.18
B2	20	0.2	4.8	0.9	0.107	0.31
B1	20	0.2	4.8	1.4	0.143	0.42
A1	20	0.2	4.8	1.8	0.160	0.52
E5	20	0.2	4.8	3.1	0.155	0.77
E4	20	0.2	4.8	5.5	0.155	0.96

Table 5.1: List of the measured efficiencies η and normalised available potential energy released APE_r from experiments in Table 3.6.

narrowest constriction ($b_o = 20$ mm), about 39% of the total available potential energy was released during the exchange flow (i.e., just before the gravity currents reached the endwalls for the first time). Note that measurements of APE_r from small and large density differences summarised in Table 5.1 confirm that between 31% and 36% of the total available potential energy was released to the mean flow by the time the gravity currents reached the endwalls. At the initial stage the proportion of the total available energy released is linearly increasing, but slowly increasing at large times (Figure 5.16). At $\tau = 5.5$ all the total available energy is almost released to the flow for the large density difference case. From theoretical estimates the fraction of the total available energy released increases with constriction minimum width, with approximately 91% of the total available energy being released during the exchange for the case of $b_o = 100$ mm.

In the case of the narrowest constriction less than 6% of the energy released was present as kinetic energy of the mean flow at the time when the barrier was reinserted, hence this small amount of the mean kinetic energy could not lead to further significant mixing (upon reflection from the endwalls or later reflections from the barrier) after the exchange flow was stopped. However, the efficiency appears to increase for $\tau > 1.0$ (Figure 5.15), in which the gravity current had already reflected from the endwalls when the exchange flow was stopped. We will further examine this case in §8.2, in which the mixing efficiency measured is larger than the average value ($\eta = 0.11$) of the efficiency.

In addition, we examined the results for rundown cases (Figure 5.17), where the barrier was not replaced into the constriction. Assuming that the uncertainty in the calculated mixing efficiency is 0.01 (as it is for cases with finite run times), the results

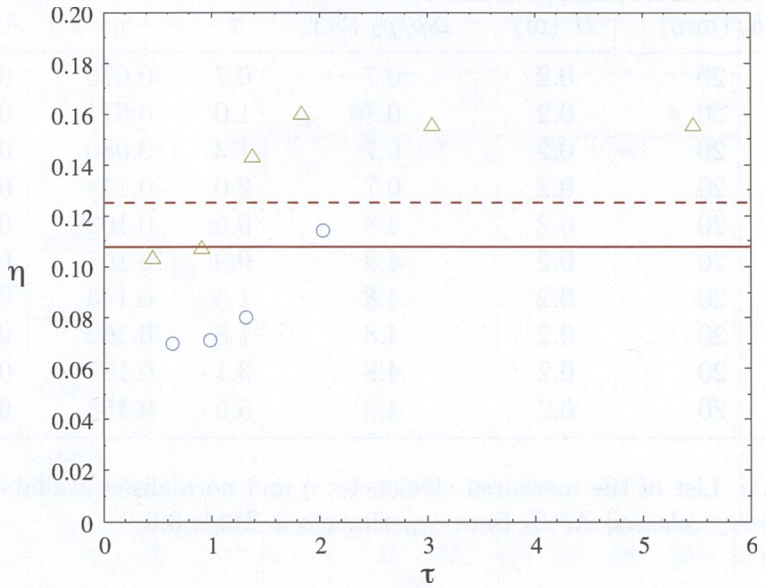

Figure 5.15: The measured mixing efficiencies η as a function of dimensionless run time τ for experiments having $0.5 \leq \tau \leq 5.5$ (Table 3.6) with $b_o = 20$ mm, $H = 0.2$ m and two different fractional density differences: $\Delta\rho/\rho_2 = 0.7\%$ (○) and $\Delta\rho/\rho_2 = 4.8\%$ (△). The red dashed line shows the theoretical value ($\eta \approx 0.125$) for the mixing efficiency given by (4.27), while the red solid line describes the mean ($\eta = 0.108$) of the mixing efficiency.

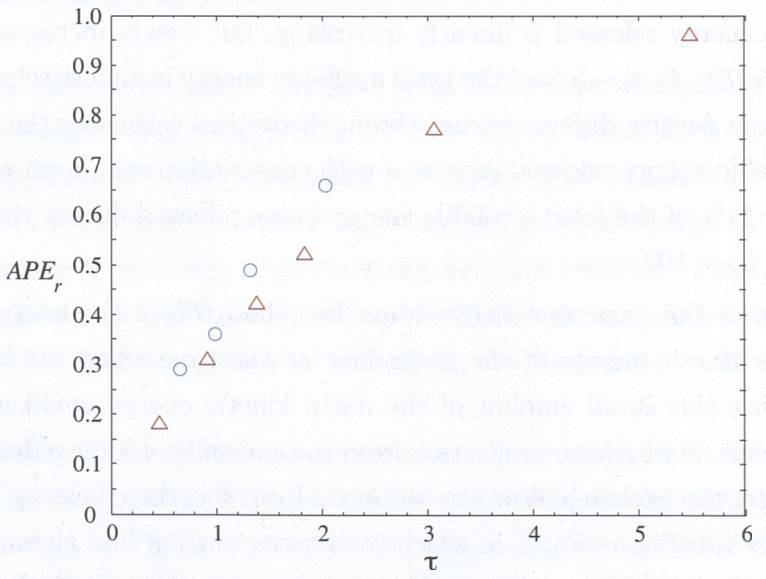

Figure 5.16: Normalised available potential energy released, $APE_r = P_a/P_t$, from experiments in Table 3.6 with two different fractional density differences: $\Delta\rho/\rho_2 = 0.7\%$ (○) and $\Delta\rho/\rho_2 = 4.8\%$ (△). Dimensionless run times used were in the range $0.5 \leq \tau \leq 5.5$.

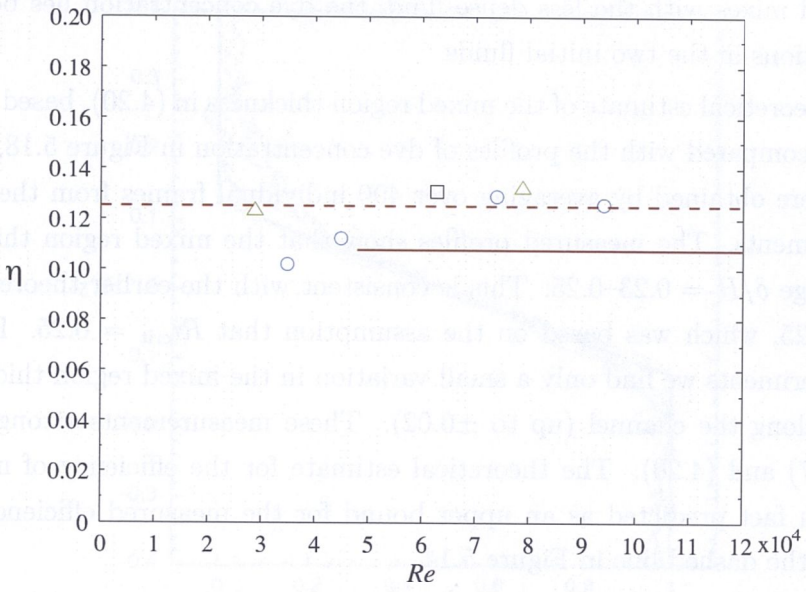

Figure 5.17: The measured mixing efficiencies η as a function of the horizontal Reynolds number for the rundown cases (Table 3.7) with $H = 0.2$ m and three different constriction widths: $b_o = 20$ mm (○), $b_o = 60$ mm (△) and $b_o = 100$ mm (□). The red dashed line shows the theoretical value ($\eta \approx 0.125$) for the mixing efficiency given by (4.27), while the red solid line describes the mean ($\eta = 0.108$) of the mixing efficiency.

reveal no significant differences in the measured efficiencies between the rundown cases, independent of the external parameters. The data show that in general the mixing efficiency in these cases approaches the theoretical value ($\eta = 0.125$), except for two cases using the narrowest constriction and small density differences.

5.4 Comparison with theory

In §4.4 we predicted a simple expression for the mixing efficiency (4.27), which involved an interfacial mixed layer of finite thickness δ (see also 4.20). Here, we examine the interface thickness in the laboratory shear flows. In most experiments a tracing paper screen was placed on the backwall of the tank and uniformly lit from behind to serve as a background diffuse light. Food dye was added to one reservoir and the thickness of the mixed region was measured from profiles of dye concentration near the mid-point of the constriction. These profiles were obtained by averaging light intensity over many frames of the digital video record. The physical principle underlying this method is that light intensity is attenuated by the dye as a ray passes through the flow (see Hacker *et al.*, 1996). In regions where the

dense fluid mixes with the less dense fluid, the dye concentration lies between the concentrations in the two initial fluids.

The theoretical estimate of the mixed region thickness in (4.20), based on a linear profile, is compared with the profiles of dye concentration in Figure 5.18, where the profiles were obtained by averaging over 400 individual frames from the videos for six experiments. The measured profiles show that the mixed region thickness lies in the range $\delta/H = 0.23$–0.25. This is consistent with the earlier theoretical result $\delta/H \approx 0.25$, which was based on the assumption that $Ri_{\rm crit} = 0.25$. For each of these experiments we find only a small variation in the mixed region thickness with position along the channel (up to ± 0.02). These measurements strongly support both (4.27) and (4.20). The theoretical estimate for the efficiency of mixing $\eta \approx 0.125$ is in fact predicted as an upper bound for the measured efficiencies, and is shown as the dashed line in Figure 5.14.

5.5 Effects of a non-linear equation of state

The non-linear equation of state may lead to a reduction of the total fluid volume when mixing occurs. This corresponds to a loss of some turbulent kinetic energy into internal (chemical) potential energy in parallel with the loss of the turbulent kinetic energy to gravitational potential energy. If this volume change effect is large, then errors will be introduced into the calculation of gravitational potential energy. We tested the magnitude of these errors by carrying out a simple experiment, in which a layer of freshwater was placed above a layer of saltwater (total water depth of 0.2 m) with a 4.8% fractional density difference. This configuration corresponds to a hypothetical state that would be attained by a complete 'rundown' (until there was no further motion) in an ideal exchange flow with no mixing. The tank was then stirred until a central region of mixed water occupied approximately one quarter of the total water depth and, therefore, the amount of mixing was comparable to that in the exchange flow experiments. The resulting decrease in the free surface height on mixing was measured to be 0.05 mm. This decreases by 4% the amount of potential energy available for conversion to kinetic energy in the exchange flow with the same density difference, as given by (4.18). Note that the potential energy change P_m given by (4.17) is largely unaffected because P_f and P_h are both reduced by approximately the same amount. The corresponding increase in mixing efficiency (4.19) is 0.005. Therefore, within the uncertainty of our measurements nonlinear mixing has a negligible effect on the measured efficiencies.

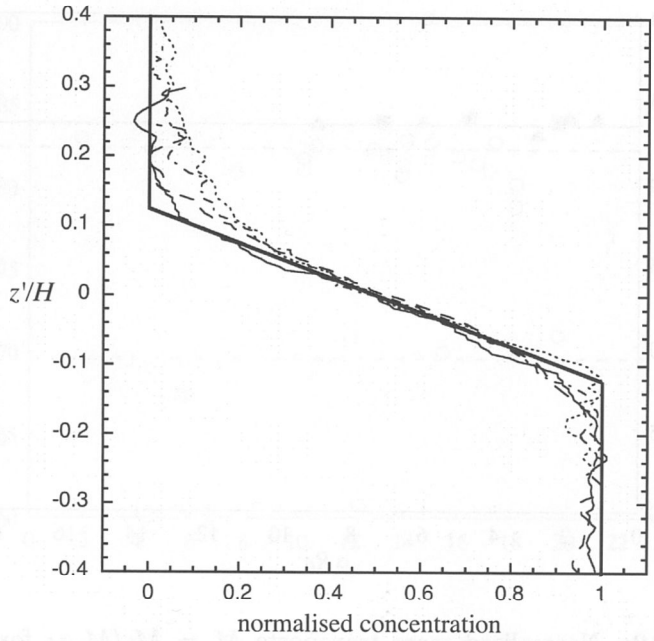

Figure 5.18: Measured profiles of normalised mean dye concentration for four different experiments using a short constriction with $b_o = 20$ mm: A8 with $Re = 3.5 \times 10^4$ (solid line), A6 with $Re = 4.6 \times 10^4$ (dashed line), E7 with $Re = 9.4 \times 10^4$ (dotted line) and E10 with $Re = 11.6 \times 10^4$ (dashed-dotted line). Normalised dye concentrations are defined such that the unmodified upper and lower layers correspond to values of zero and one, respectively. The height is normalised by the total water depth H such that $z' = 0$ corresponds to the centre of the interfacial mixed layer. The normalised thickness of the interfacial mixed layer δ/H is based on the (maximum) concentration gradient at $z' = 0$, and the dark solid line denotes the piecewise linear approximation to a normalised concentration profile with $\delta/H \approx 0.25$.

5.6 Mass transport

5.6.1 Short constrictions

We compare the net mass transport measured in these experiments with the predictions of hydraulic theory. In Figure 5.19 we show the measured transport M_e (4.4) normalised by the maximal hydraulic prediction (2.21) to obtain $M = M_e/M_{\max}$ as a function of the horizontal Reynolds number Re for all experiments with a short constriction. The resulting normalised transport through the short constrictions is approximately constant at $M = 0.82 \pm 0.03$. The uncertainty quoted in the measured transports is predominantly that owing to the uncertainty in the experimental run time, which is estimated at 1 second in each case. This uncertainty is comparable to the scatter in the results (with the standard deviation of 0.013, for which

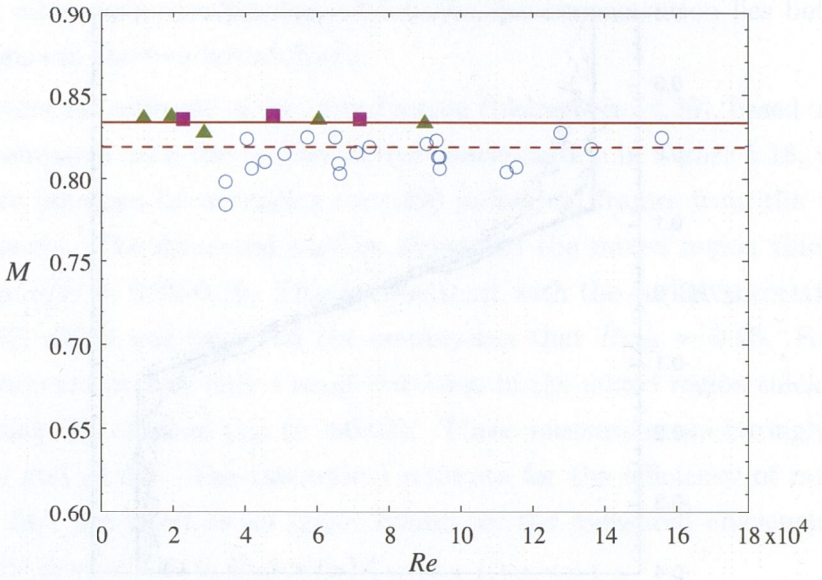

Figure 5.19: Normalised mass transports $M = M_e/M_{\max}$ for all experiments with the short constrictions (Table 3.1), as a function of the horizontal Reynolds number Re. Symbols indicate $b_o = 20$ mm (○), 60 mm (△) and 100 mm (□). The red solid line shows the theoretical estimate for the mass transport through the short constrictions in (4.30) with M_{fri} set to zero, while the red dashed line is the mean ($M = 0.819$) of the measured transports in the experiments.

the uncertainty could be estimated to be twice this standard deviation). Note that the uncertainty could also again be estimated by comparing two experiments (E13 and E19 in Table 3.1) having the same flow variables, but different initial conditions: equal bottom pressures in E13 and equal pressures at mid-depth in E19. We found a difference of 0.022 in the calculated values of the normalised transport M from these experiments. Thus it is justifiable to quote the uncertainty in the measurements of normalised transports through the short constrictions as 0.03.

The above results for the short constriction cases compare well with the hydraulic theory modified by the predicted 17% transport reduction owing to mixing given by (4.29), consistent with the influence of friction in the short constrictions being small. More precisely, in the experiments with the narrowest constriction ($b_o = 20$ mm) the average of the measured transports is $M = 0.813 \pm 0.025$ (with the standard deviation of 0.011 for this case), whereas in the experiments with wider constrictions (60 mm and 100 mm), the observed transport is indistinguishable from the upper bound estimate of 0.833 (Figure 5.19), predicted with mixing but no frictional effects. This small trend with b_o is again consistent with a very small frictional reduction.

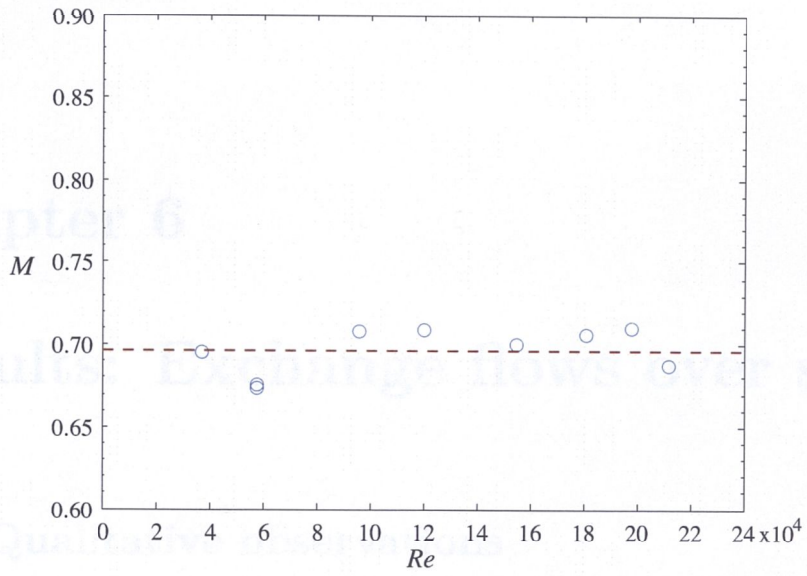

Figure 5.20: Normalised mass transports $M = M_e/M_{\max}$ for all experiments with the long constriction (Table 3.2), as a function of the horizontal Reynolds number Re. The red dashed line is the mean ($M = 0.696$) of the measured transports (blue open circles) in the experiments.

5.6.2 Long constriction

The normalised net mass transports from all experiments with the long constriction are plotted in Figure 5.20. These measured transports are approximately constant at $M = 0.70 \pm 0.03$, thus significantly less than those through the short constrictions (the uncertainty estimate again being dominated by the run time uncertainty of approximately 1 second in each run, and also comparable with the standard deviation of the data, which is 0.014). Hydraulic theory predicts that, in the absence of friction, the two control points for the exchange flow in this geometry occur at either end of the long section of the constant width section. The observed average of the transport shown in Figure 5.20 suggests that the frictional reduction predicted by (4.30) in the long constriction case is about ten times greater than in the short constrictions. The results also suggest that there is no dependence of the transport on the Reynolds number Re for this particular geometry, and that the estimate of the frictional reduction given by (4.33) is no longer applicable. We will further discuss this finding and compare it with the results from other geometries in §8.3.

Chapter 6

Results: Exchange flows over sills

6.1 Qualitative observations

Each exchange flow over a sill was initiated by removing a sliding barrier that had been positioned above the bottom sill and which separated the fresh and saltwater reservoirs. The sill was either a weir (Figure 6.1) or a triangular-shaped sill (Figure 6.2 and Figure 6.3). Once the barrier was withdrawn the less dense fluid moved along the surface into the right reservoir and the dense fluid either plunged down the vertical side of the weir (Figure 6.1*a*) or ran down a slope in the lee side of the sill (Figure 6.2*a* and Figure 6.3*a*). There was an increased flow speed at the crest of the sill (the control point) and consequently the dense fluid of the lower layer on the right reservoir was drawn up to flow over the sill. When the dense overflow reached the bottom of the sill it began to fill up the left reservoir. It was observed that waves with large amplitudes were generated and grew in size (Figure 6.1*c*, Figure 6.2*c* and Figure 6.3*c*). The large amplitude waves were associated with the rapid development of KH billows, which mixed the fluid near the bottom of the sill as they were carried away from the sill (Figure 6.1*d*, Figure 6.2*d* and Figure 6.3*d*). These billows collapsed upon the exit of the constriction, after which the mixed fluid was advected away from the exit region of the constriction by a gravity current. This current had a larger head with more mixing above its head relative to that in flows through the constrictions without a sill (as described in §5.1). The interface between the layers upstream of the sill was almost flat, stretched to the exit region of the constriction in the right reservoir. The KH billows then appeared to roll-up in this region, but with relatively small amplitudes (Figure 6.2*e* and Figure 6.3*e*) compared with those in the left reservoir or those in flows through the constrictions with no sills.

In all cases it was observed that gravity currents travelled away from the topo-

graphic constriction and that interfacial mixing took place above the gravity current heads and in the stratified regions along the channel as the currents propagated in the reservoirs, although it was again visibly much less intense than that in the topographic constriction. These currents were eventually reflected back from the channel endwalls after the barrier was reinserted. The reflection produced a bore that later reached the barrier in the centre of the constriction, and that was reflected again. There followed a period of complicated interactions between internal waves in the reservoirs. The reflections and interactions of these waves caused a further, minor amount of mixing.

In the case of the weir it was observed that at the initial stage of the exchange the dense water spilled over the weir (Figure 6.1*a*), producing very large overturns and vigorous mixing in the vicinity of the bottom of the weir (Figure 6.1*b*) and at the end of the constriction straight central section (Figure 6.1*c*). A bore was initially observed to propagate away from the weir (Figure 6.1*d*) and later passed through the exit of the constriction (Figure 6.1*e*).

For the triangular sill case the downsloping overflow (Figure 6.2*b* and Figure 6.3*b*) again induced shear instability and extensive mixing, particularly near the bottom of the lee side of the sill (Figure 6.2*c* and Figure 6.3*c*). A stationary hydraulic jump occured downstream of the sill (Figure 6.2*d* and Figure 6.3*d*), causing more mixing in that region. After these early stages, the flow had finally achieved a steady mean state by frame (*e*) of Figure 6.2 and Figure 6.3.

6.2 Density profiles

Normalised density profiles from both the left and right reservoirs measured after each exchange with a sill are plotted in Figure 6.4. Figure 6.4(*a*, *b*) show the normalised profiles from experiments with the weir using the same water depth H (0.2 m) for three different fractional density differences. The profiles in each reservoir are similar to each other, suggesting that the measured transport scales with the hydraulic prediction (2.23) and is independent of the density contrast, hence the Reynolds number. Figure 6.4(*c*, *d*) show the normalised profiles for the triangular sill case with the same water depth H (0.2 m) and three different fractional density differences. Again, the profiles in each reservoir are indistinguishable from each other, particularly those on the right reservoir. Small differences in the right profile shapes between experiments with the weir (Figure 6.4*b*) and those with the triangular sill (Figure 6.4*d*) imply that the normalised transport in both cases is almost the same, weakly dependent on the sill geometry. However, there are differences in

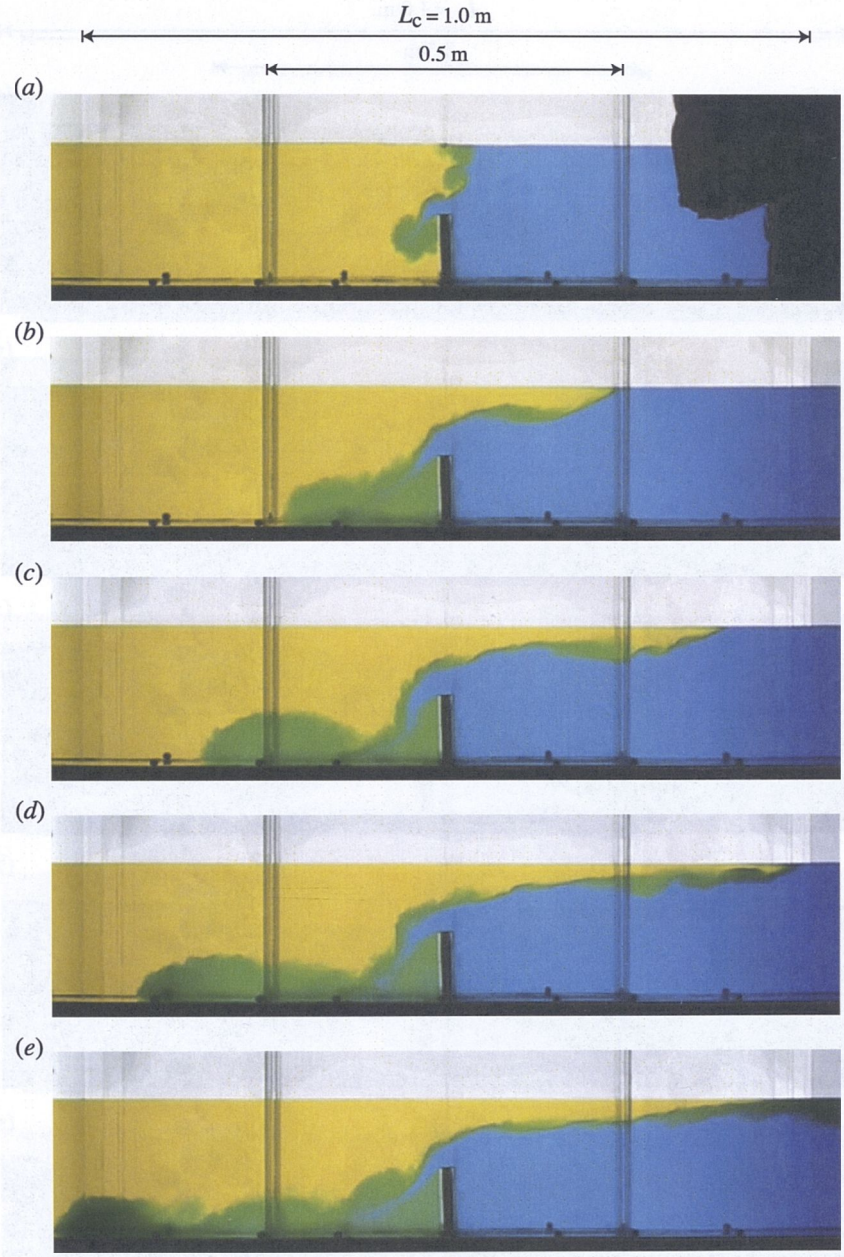

Figure 6.1: A series of photographs from experiment J2 (Table 3.3) showing early stages of the experiment using the weir with $b_o = 60$ mm, $\Delta\rho/\rho_2 = 4.8\%$, $H = 0.2$ m and $Re = 5.4 \times 10^4$. The weir height was $d = 0.1$ m. Frames (a) through (e) were taken at about 1.2, 2.8, 3.8, 4.6 and 8.6 seconds after the barrier was withdrawn.

the left profiles between the weir (Figure 6.4a) and the triangular sill (Figure 6.4c) in regions close to the bottom boundary. This difference suggests that mixing is enhanced in the left reservoir for the triangular sill case, leading to a strong flow asymmetry in this case. We will further examine this asymmetry in §8.2.

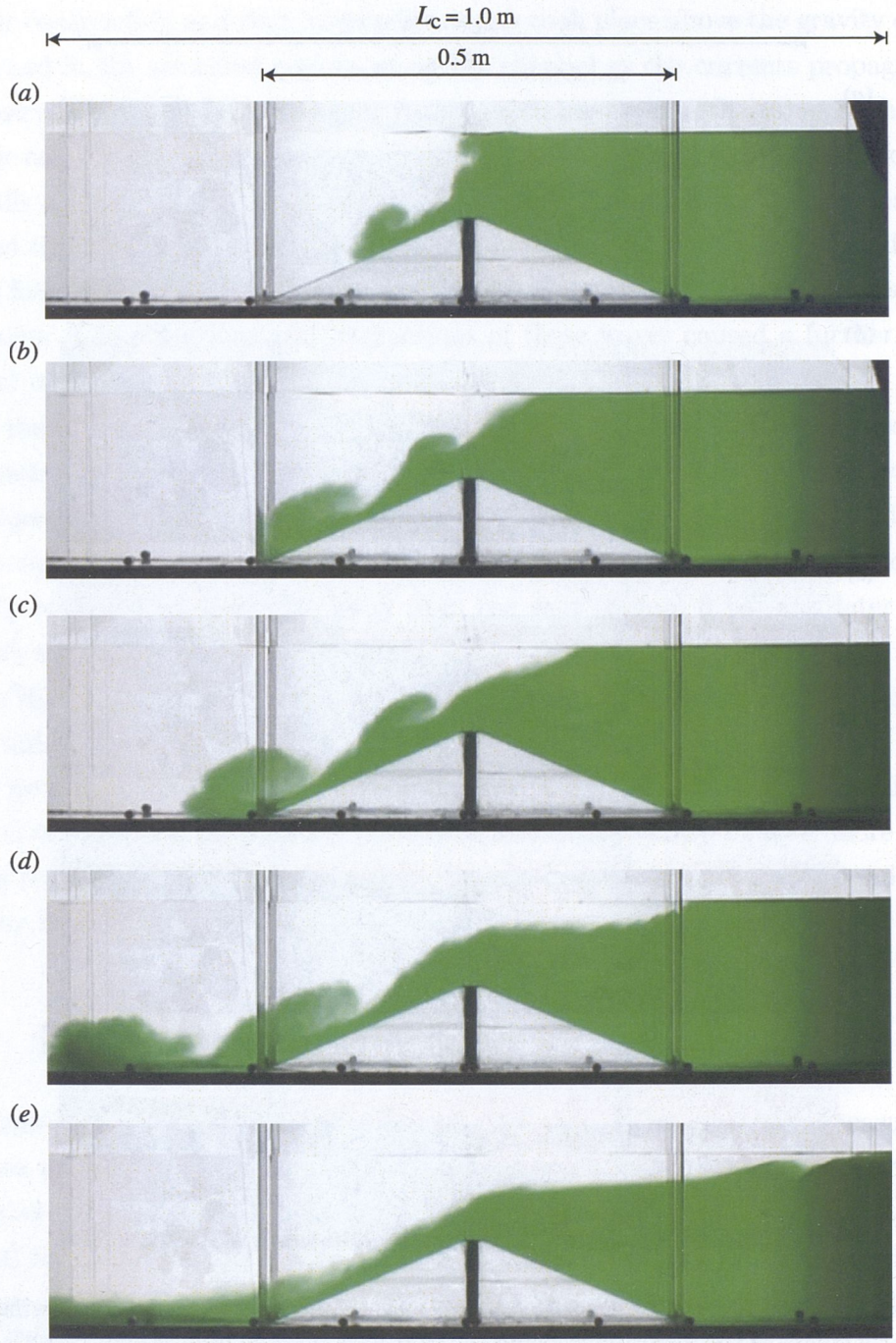

Figure 6.2: A series of photographs from experiment K4 (Table 3.3) showing stages of the experiment using the triangular sill with $b_o = 60$ mm, $\Delta\rho/\rho_2 = 6.7\%$, $H = 0.2$ m and $Re = 12.7 \times 10^4$. The sill length occupied the whole length (0.5 m) of the constriction straight central section and the sill height was $d = 0.1$ m. Frames (a) through (e) were taken at about 1.1, 1.8, 2.3, 3.4 and 10.4 seconds after the barrier was withdrawn.

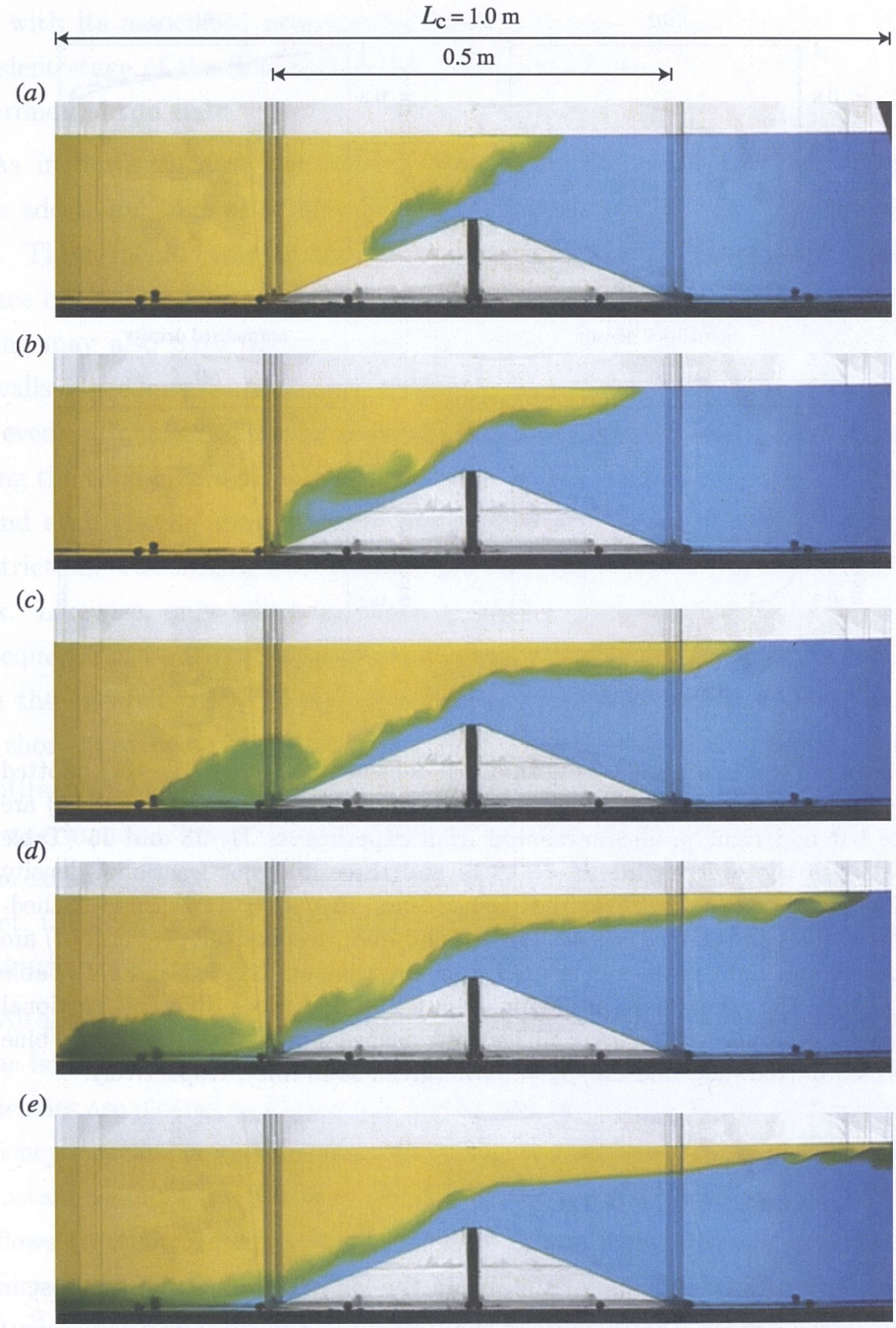

Figure 6.3: A series of photographs from experiment K6 (Table 3.4) showing stages of the experiment using the triangular sill with $b_o = 60$ mm, $\Delta\rho/\rho_2 = 1.9\%$, $H = 0.2$ m and $Re = 6.7 \times 10^4$. The sill length occupied the whole length (0.5 m) of the constriction straight central section and the sill height was $d = 0.1$ m. Frames (a) through (e) were taken at about 2.3, 3.7, 5.3, 7.0 and 13.8 seconds after the barrier was withdrawn.

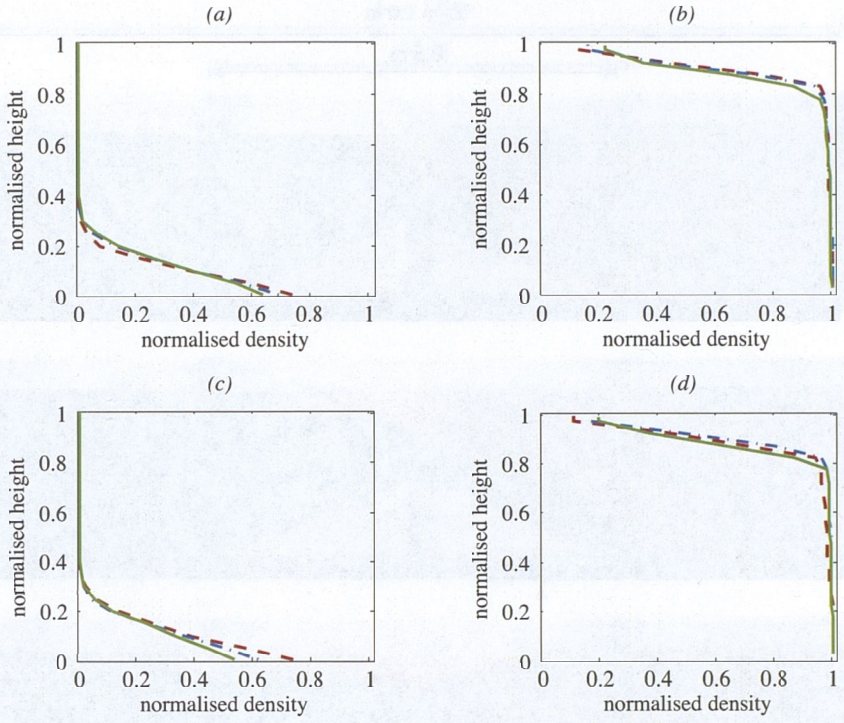

Figure 6.4: Final profiles of normalised density $(\rho(z)-\rho_1)/(\rho_2-\rho_1)$, plotted against normalised height z/H in experiments with the sills. (*a*) and (*b*) are the left and right profiles measured from experiments J1, J3 and J6 (Table 3.3) with the weir having $H = 0.2$ m and three different fractional density differences: $\Delta\rho/\rho_2 = 0.7\%$ (red dashed line), $\Delta\rho/\rho_2 = 3.0\%$ (blue dashed-dotted line) and $\Delta\rho/\rho_2 = 9.4\%$ (green solid line), respectively; (*c*) and (*d*) are the left and right profiles measured from experiments K1, K3 and K7 (Table 3.4) with the triangular sill having $H = 0.2$ m and three different fractional density differences: $\Delta\rho/\rho_2 = 0.7\%$ (red dashed line), $\Delta\rho/\rho_2 = 2.9\%$ (blue dashed-dotted line) and $\Delta\rho/\rho_2 = 9.5\%$ (green solid line), respectively.

6.3 Mixing efficiency

There are several mechanisms for mixing in the sill experiments. The most intense mixing was observed in the vicinity of the bottom of the sill, and took place downstream of the sill crest, where the downslope flow was subject to acceleration leading to increased shear. In this region strong turbulence was characterised by a region of breaking gravity waves with large overturns owing to the rapid growth and decay of KH billows in the strongly-sheared, turbulent interface. A persistent, stationary hydraulic jump was observed at the bottom of the sill, and may have caused more mixing in the left reservoir. These mechanisms are associated with the constriction and bottom sill, and are not transient despite the unsteady nature of the dam-break

flow with its associated propagating gravity current heads. Note that the initial transient stage of the flow within the constriction took only about 5% of the total experimental run time.

As in flows through the constrictions (discussed in detail in §5.3), there are some additional sources of mixing in the reservoirs during and after the exchange flow. These include mixing above the gravity current heads and along the upper surface of the following currents. After the replacement of the barrier some minor mixing may also have occurred due to a reflection of the gravity currents at the endwalls of the long tank with the resulting bores colliding with the replaced barrier, and eventually followed by subsequent minor mixing due to wave-wave interactions during the time before all motions die away. It was clear that mixing in the regions behind each gravity current head was considerably less intense than that in the constriction. The mixing above the length of the gravity currents was also relatively weak. Likewise, only minor amounts of mixing were likely to have occurred as a consequence of breaking internal waves after the reflections of the gravity currents from the endwalls and the replaced barrier, this mixing being limited to isolated and short-lived events. As with the constrictions it was not possible to separate quantitatively the relative contributions of the various processes to mixing. Rather, the experiments allowed measurements of the overall amount of mixing in the whole of the exchange flow. While we consider this overall mixing to be the most important target, the observations above suggest that the results will be indicative of mixing within the constriction.

We again considered mixing efficiency measured from all sill experiments in terms of the horizontal Reynolds number (defined for sill flows, see §3.3.2). The resulting efficiencies are plotted in Figure 6.5. In the case of the weir (open circles) the mixing efficiency increases with increasing Re at low Reynolds numbers, and asymptotes to a constant value of $\eta = 0.109$ at $Re \gtrsim 5 \times 10^4$, in good agreement with the results for flows through the constrictions (see §5.3) where the average measured mixing efficiency is 0.108, provided that $Re > 5 \times 10^4$. In experiments with small Re the turbulence was visibly weak, particularly in the right reservoir, consistent with the smaller measured mixing efficiencies, which may imply that viscous dissipation absorbs a larger proportion of kinetic energy from the mean flow.

For the triangular sill case (triangles in Figure 6.5) the measured mixing efficiency indicates a constant asymptote of $\eta = 0.084 \pm 0.003$ for $Re > 4 \times 10^4$. The uncertainty quoted is the standard deviation of these measurements. We further examined this uncertainty by comparing two identical experiments (K4 and K5 in Table 3.4) having the same conditions and all other flow variables, and found a dif-

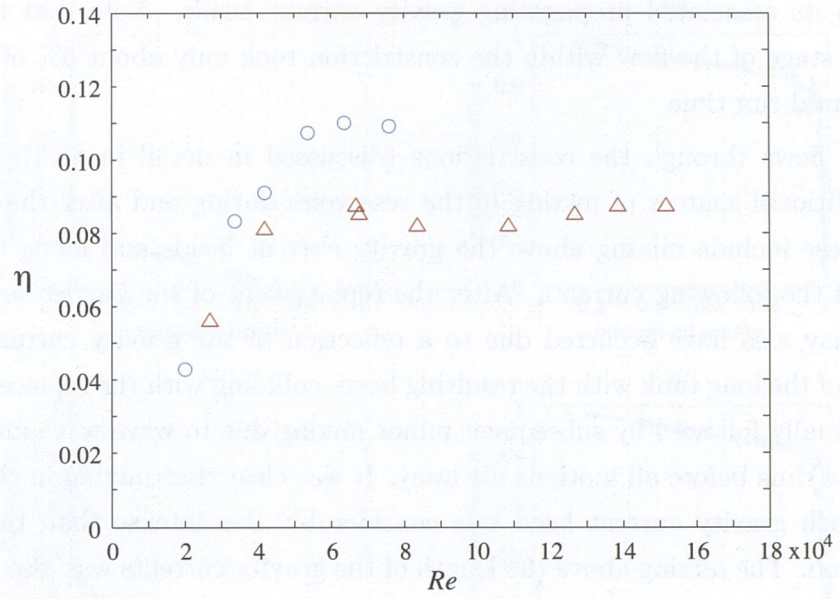

Figure 6.5: The measured mixing efficiencies η as a function of the horizontal Reynolds number Re for all sill experiments (Table 3.3 and Table 3.4) having $H = 0.2$ m, $b_o = 60$ mm and various fractional density differences. Symbols indicate experiments with the weir (○) and with the triangular sill (△).

ference of 0.002 in the calculated efficiencies, which is comparable with the standard deviation of the data.

The above results suggest that the geometry of bottom topography plays a small but significant role in determining the mixing. Most remarkable is that the flows over the weir involve the same mixing efficiency as those through the constrictions with no bottom topography. The slightly smaller mixing efficiencies found for the triangular sill case will later be analysed in terms of the flow asymmetry in §8.2. For both sills the mixing efficiency reaches an asymptotic value at a comparable critical Reynolds number.

6.4 Mass transport

We normalise the net mass transport M_e measured in experiments with the sills by the maximal exchange $M_{\max}$ predicted by hydraulic solution for the sill flow given in (2.23). Thus we have $M = M_e/M_{\max}$ for the sill cases, and plot M as a function of the horizontal Reynolds number Re for all sill experiments in Figure 6.6. The measured normalised net mass transport over the weir is $M = 0.74 \pm 0.01$, and for the triangular sill case the normalised net mass transport is $M = 0.72 \pm 0.01$. The uncertainties quoted in the measured transports are predominantly owing to

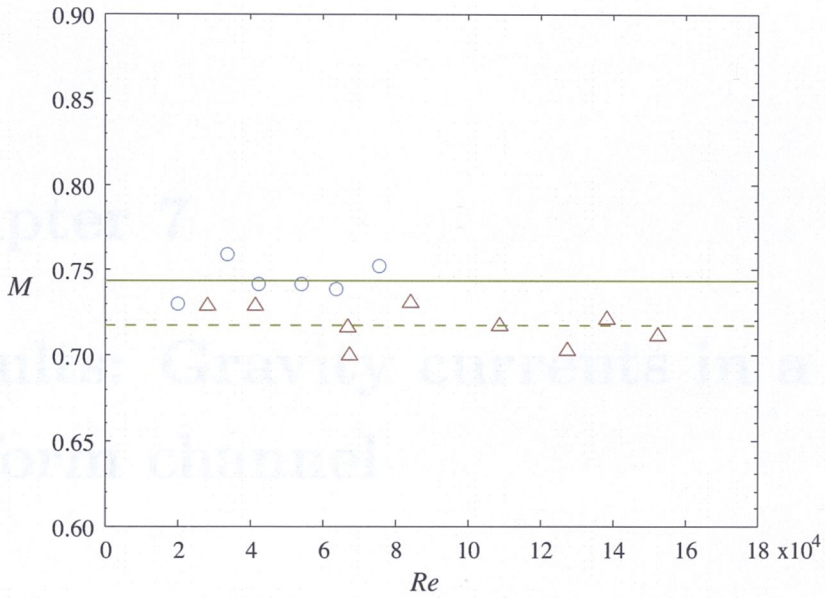

Figure 6.6: Normalised mass transports $M = M_e/M_{\max}$ for all experiments with the sills (Table 3.3 and Table 3.4), as a function of the horizontal Reynolds number Re. Symbols indicate experiments with the weir (○) and with the triangular sill (△). The green solid line shows the mean ($M = 0.744$) of the measured transports with the weir and the green dashed line describes the mean ($M = 0.718$) of the measured transports with the triangular sill.

the uncertainty in the experimental run time, which is 0.5 second in each case. This uncertainty is comparable with the standard deviation of approximately 0.01 for both cases.

The small difference in the measured transports between experiments with the weir and those with the triangular sill may be associated with the different processes of mixing and friction in these cases. The normalised transport in the sill cases is comparable with that in the long constriction (see §5.6.2). Again, as in the long constriction (4.33) is no longer relevant to be used to predict the magnitude of the frictional flux reduction in these cases. We conclude that the normalised transport over the sills is independent on the external parameters used, but is weakly dependent on the geometry of the sill. The introduction of a bottom sill into the long constriction alters the detail of the flow, but does not reduce the normalised flux (compared with the same constriction geometry without a sill). We will further discuss these results in §8.3 in the light of the influence of channel geometry and shape on the transport.

Chapter 7

Results: Gravity currents in a uniform channel

7.1 Qualitative observations

Exchange flows carried out in a uniform channel with no lateral contraction and no bottom topography are here referred to as 'gravity current' experiments, as they are similar to the flows in many previous studies of gravity currents. They differ from the other exchange flows reported in this thesis in that there is no hydraulic control point. Each gravity current experiment was initiated by removing a sliding barrier dividing the fresh and saltwater reservoirs. We provide a series of photographs from a case with $H = 0.2$ m, showing the development of the flows for two different vertical Reynolds numbers, associated with a small (Figure 7.1) and a large (Figure 7.2) density difference. As the barrier was withdrawn the density interface began to adjust and a characteristic gravity current head developed (Figure 7.1*a* and Figure 7.2*a*). Subsequently, the head of the gravity current travelled along the channel and mixing was observed to take place behind the head while the current propagated (Figure 7.1*b* and Figure 7.2*b*). For a short period there appeared KH billows to roll-up on the density interface near the original position of the barrier (Figure 7.1*c* and Figure 7.3*a*). After this stage the gravity currents carried the resulting mixed fluid along the channel (Figure 7.1*d* and Figure 7.2*c*). At later times the interface slope was observed to be flat (Figure 7.1*e*, Figure 7.2*d* and Figure 7.3*b*).

As time progressed the dense current advanced along the base of the channel in the left reservoir and the less dense current propagated in the opposite direction at the surface of the right reservoir. As the gravity currents continued to travel along the channel fluid was continuously supplied to the front of the currents from the relatively unmixed fluid in the reservoirs. In this way sharp fronts of constant

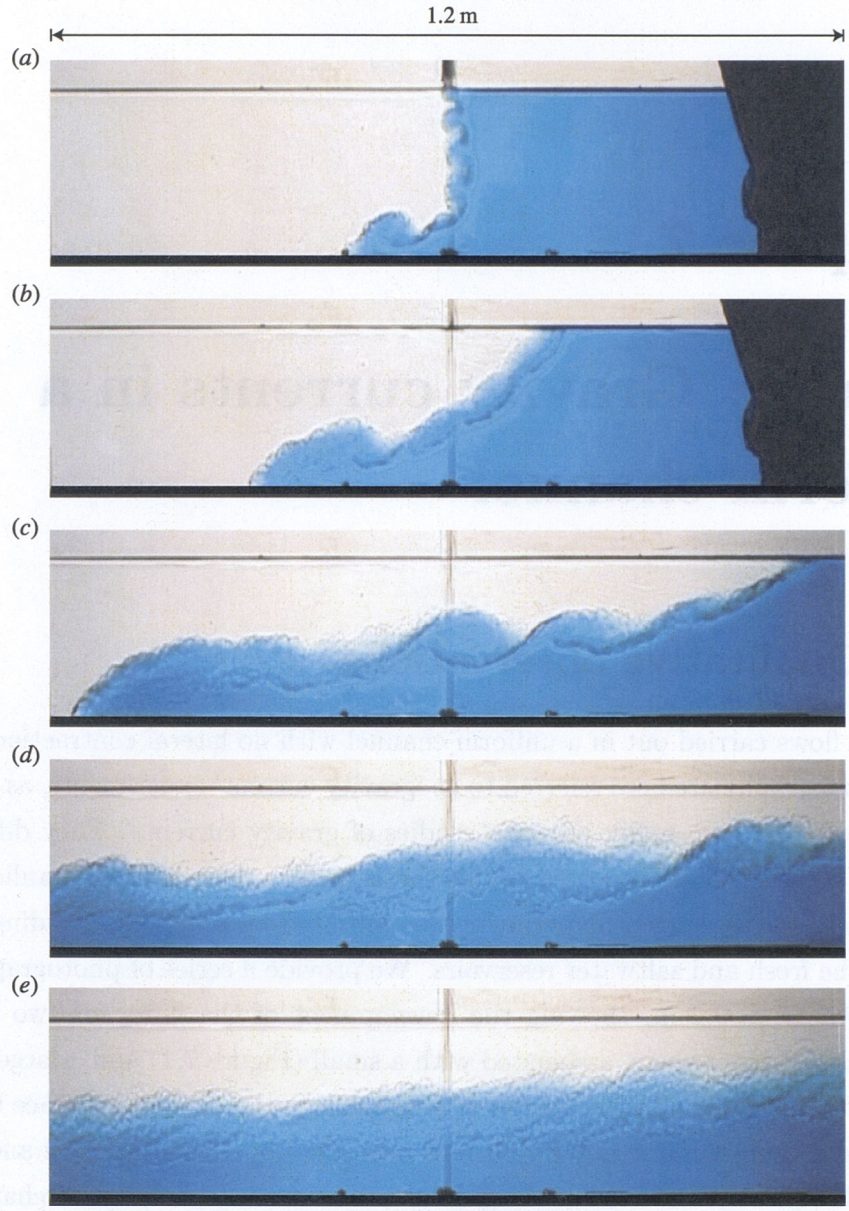

Figure 7.1: A series of photographs showing various stages of experiment G2 (Table 3.5) with $H = 0.2$ m, $\Delta\rho/\rho_2 = 1.9\%$ and $Re_H = 1.9 \times 10^4$. Frames (a) through (e) were taken at 1.6, 3.2, 6.4, 9.6 and 14.5 seconds after the barrier was withdrawn.

shape were maintained and the front speed was nearly constant (Figure 7.4). The exchange was stopped by reinserting the barrier into the channel when the gravity current noses had nearly reached the endwalls (Figure 7.4f).

Experiments were also conducted using a greater water depth of $H = 0.3$ m. In general, the flow development at various stages of the exchange was similar in shallow ($H = 0.2$ m) and deep ($H = 0.3$ m) gravity currents. Figure 7.5 shows a

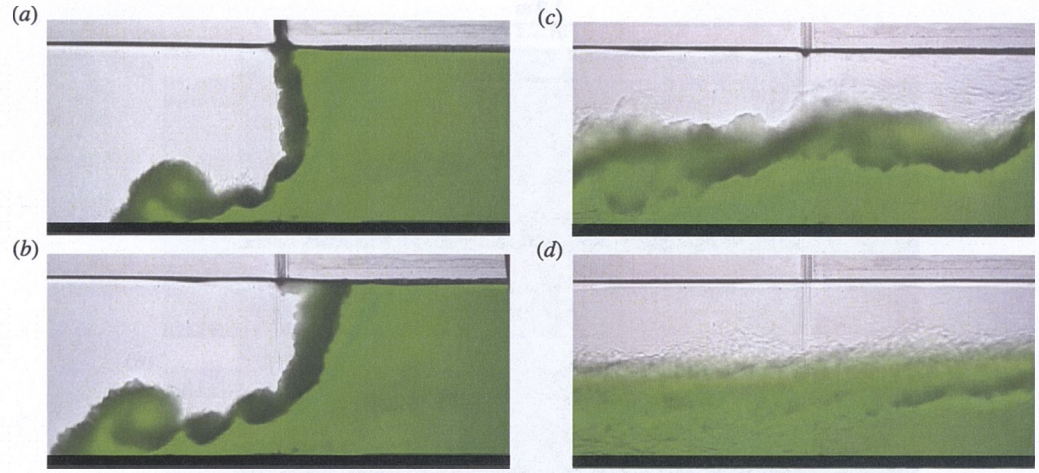

Figure 7.2: A series of photographs showing various stages of experiment G6 (Table 3.5) with $H = 0.2$ m, $\Delta\rho/\rho_2 = 6.7\%$ and $Re_H = 3.6 \times 10^4$. Frames (a) through (d) were taken at 1.2, 1.7, 4.2 and 10.0 seconds after the barrier was withdrawn.

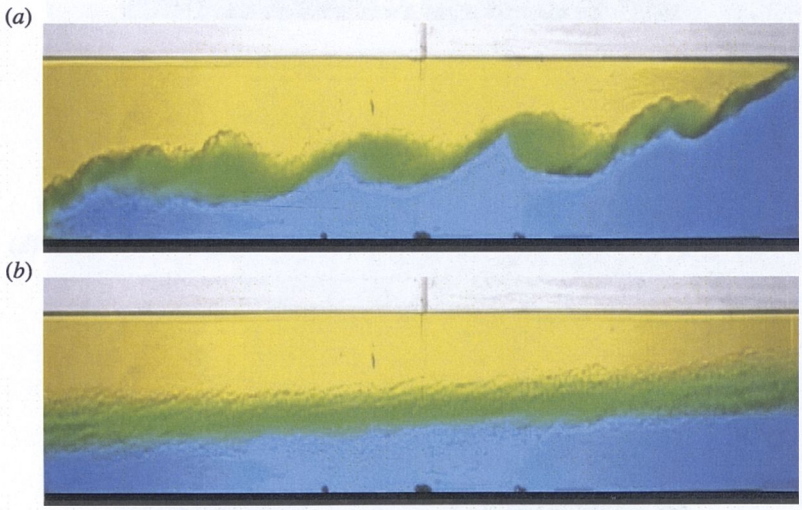

Figure 7.3: Experiment G3 (Table 3.5) with $H = 0.2$ m, $\Delta\rho/\rho_2 = 3.0\%$ and $Re_H = 2.4 \times 10^4$, showing (a) mixing behind the head and in the stratified region behind the head and (b) mixed water on the density interface in the trailing current away from the head. Frames (a) and (b) were taken at times when the current had travelled from the centre of the channel over a distance, which corresponded to 25% and 65% of the total run time, respectively.

series of photographs from a case with $H = 0.3$ m, which had approximately the same vertical Reynolds number as the experiment with $H = 0.2$ m shown in Figure 7.1, but with a smaller fractional density difference. Details of the similarities as well as the differences between the two cases will be further discussed in §7.3.

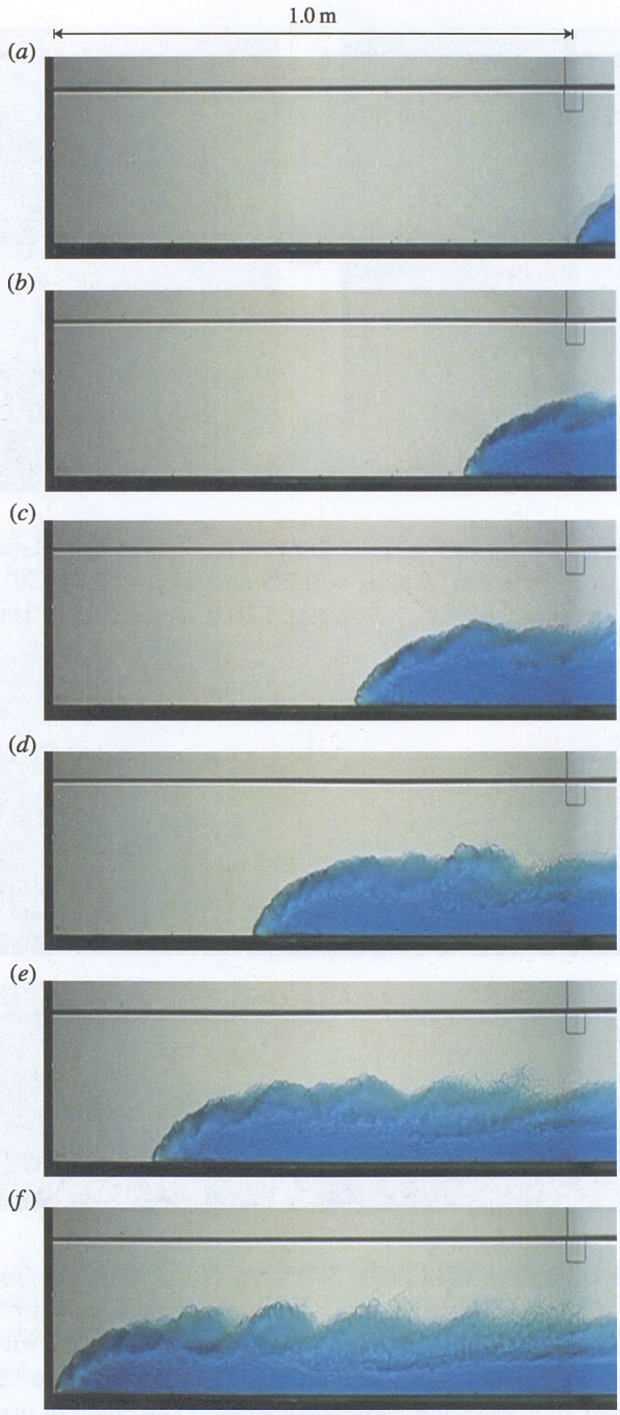

Figure 7.4: Gravity current front propagating towards the channel endwall from an experiment (data are not included in Table 3.5) with $H = 0.2$ m, $\Delta\rho/\rho_2 = 3.0\%$ and $Re_H = 2.4 \times 10^4$. Each frame was taken at an interval of 1.68 s such that the total time taken for the front to propagate 1.0 m was 8.4 s. The distance between two consecutive frames was approximately constant at 0.2 m, suggesting that this front travelled at a constant speed of approximately $0.5\sqrt{g'H}$, as predicted by theory (Benjamin, 1968).

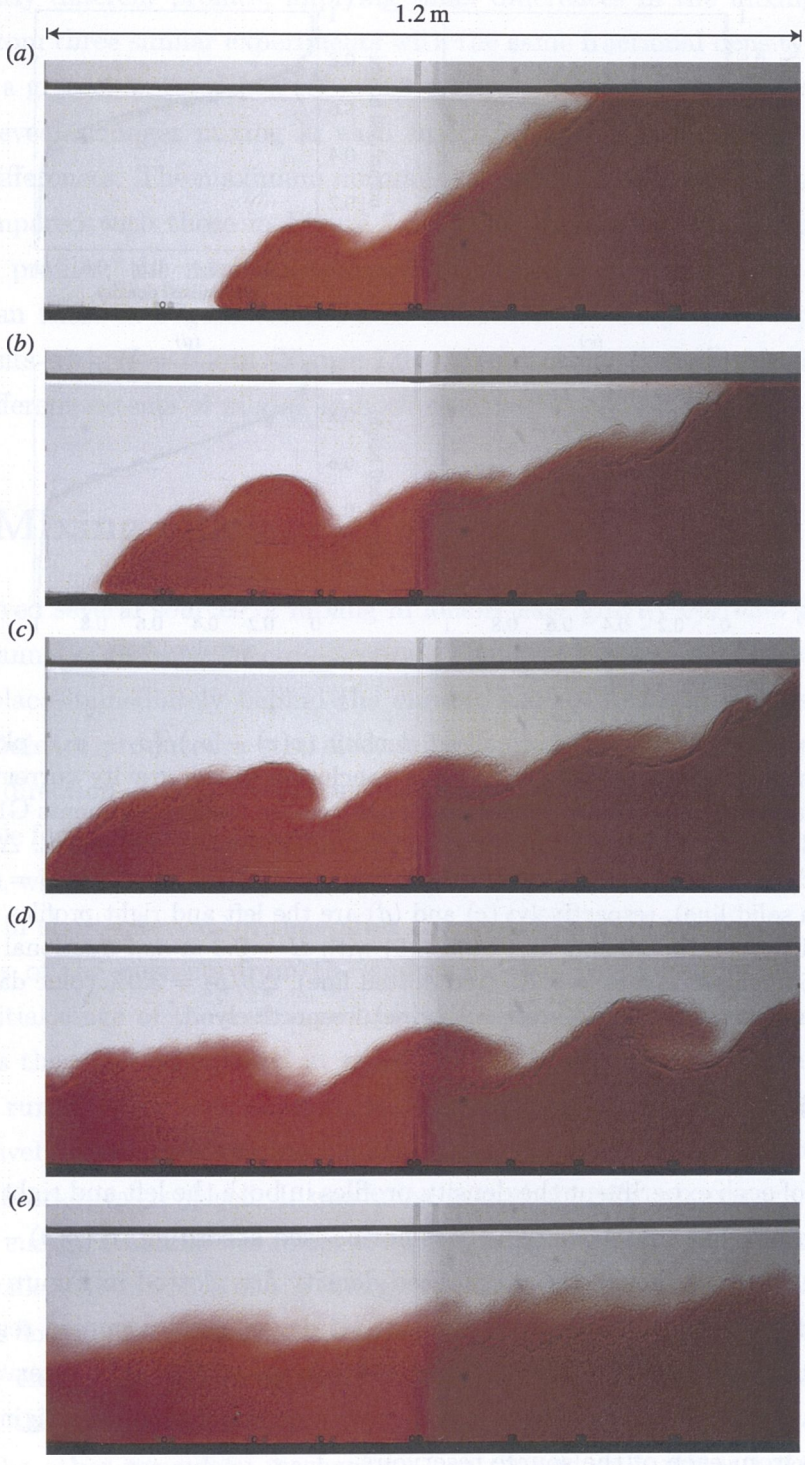

Figure 7.5: A series of photographs showing various stages of experiment G11 (Table 3.5) with $H = 0.3$ m, $\Delta\rho/\rho_2 = 0.7\%$ and $Re_H = 2.1 \times 10^4$. Frames (a) through (e) were taken at 5.6, 7.8, 9.6, 13.2 and 23.8 seconds after the barrier was withdrawn.

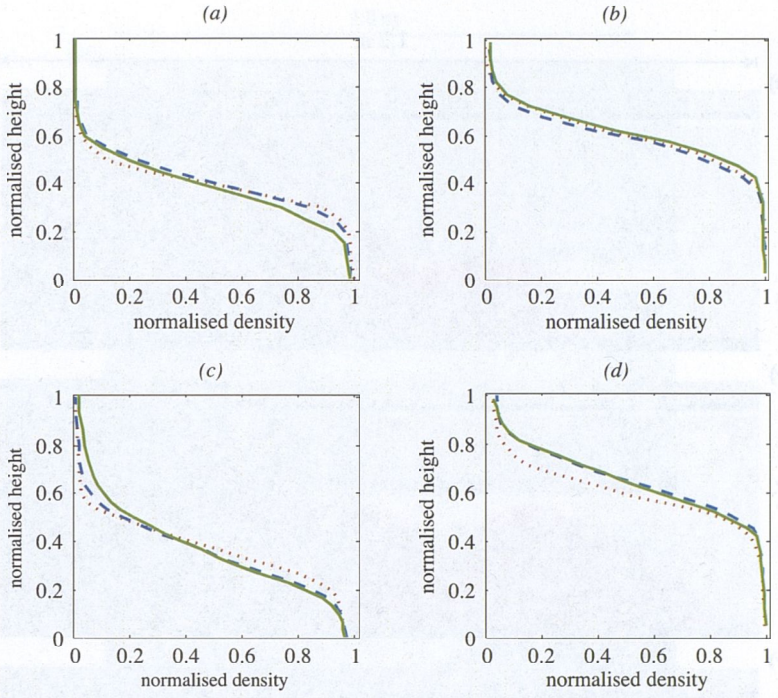

Figure 7.6: Profiles of normalised density $(\rho(z) - \rho_1)/(\rho_2 - \rho_1)$, plotted against normalised height z/H, at the conclusion of the gravity current experiments. (*a*) and (*b*) are the left and right profiles from experiments G1, G3 and G5 (Table 3.5) with $H = 0.2$ m and fractional density differences: $\Delta\rho/\rho_2 = 0.7\%$ (red dotted line), $\Delta\rho/\rho_2 = 3.0\%$ (blue dashed line) and $\Delta\rho/\rho_2 = 4.8\%$ (green solid line), respectively; (*c*) and (*d*) are the left and right profiles from experiments G11, G8 and G9 (Table 3.5) with $H = 0.3$ m and fractional density differences: $\Delta\rho/\rho_2 = 0.7\%$ (red dotted line), $\Delta\rho/\rho_2 = 3.0\%$ (blue dashed line) and $\Delta\rho/\rho_2 = 4.8\%$ (green solid line), respectively.

7.2 Density profiles

At the end of each experiment the density profiles in both the left and right reservoirs were measured. The measured density is normalised according to $(\rho(z) - \rho_1)/(\rho_2 - \rho_1)$, and example profiles of the normalised density are plotted in Figure 7.6. In all cases about 20% of the relatively dense (or less dense) fluid occupied regions close to the bottom of the left reservoir (or at the surface of the right reservoir). This fluid had a density that was almost unaltered, compared with the original density of the fluid from each of the source reservoirs.

Figure 7.6(*a*, *b*) shows profiles from three experiments in Table 3.5 with the same water depth ($H = 0.2$ m), but with different fractional density differences. The similarities in the left and right profile shapes indicate that almost the same amount of mixing occurred in both reservoirs. However, different density differences

give slightly different profiles, implying small differences in the mixing processes. Profiles from three similar experiments with the same fractional density differences, but with a greater water depth ($H = 0.3$ m) are plotted in Figure 7.6(c, d). These profiles reveal stronger mixing in each reservoir, particularly for the two largest density differences. The maximum normalised densities in Figure 7.6c are relatively small compared with those in Figure 7.6a. The opposite results are obtained for the right profiles; the minimum normalised densities in Figure 7.6d are slightly larger than those in Figure 7.6b. These differences in the profile shapes between experiments with $H = 0.2$ m (Figure 7.6a, b) and $H = 0.3$ m (Figure 7.6c, d) also reflect different extents of mixing in both cases.

7.3 Mixing efficiency

We observed several sources of mixing in lock-release gravity currents generated in a long channel of rectangular cross-section. The most vigorous mixing was observed to take place immediately behind the current heads. In these regions the small-scale turbulence produced a stratified, mixed region in which the water moved in the same direction as the currents but with smaller speeds. A secondary mechanism responsible for mixing was associated with shear in the stratified regions well behind the heads, which caused further overturning and thus additional mixing. Mixing also occurred in short intervals of time after the replacement of the barrier and during reflections of the currents from the endwalls. The rapid removal of the barrier at the initial stage of the exchange had no significant contributions to the overall mixing as this step constituted at most (for the largest density difference) 8% of the total run time for each experiment. Another source of mixing, but one which was relatively minor, was the mechanism of wave breaking within the stratification after the barrier was replaced. It was found that about 96%, on average, of the total potential energy available was released by the time the gravity current noses reached the endwalls. About 50% of the energy released was present as kinetic energy of the mean flow at the moment the barrier was replaced, and therefore that portion of kinetic energy could lead to additional mixing after the exchange was stopped. However, the mixing behind the current heads is the primary mixing mechanism and all the other secondary mechanisms contributed only minor amounts to the total mixing in the gravity currents.

We plot the measured mixing efficiencies η from shallow ($H = 0.2$ m) and deep ($H = 0.3$ m) gravity currents against the vertical Reynolds number Re_H in Figure 7.7, but find no clear dependence of the mixing efficiency upon the depth, and in contrast

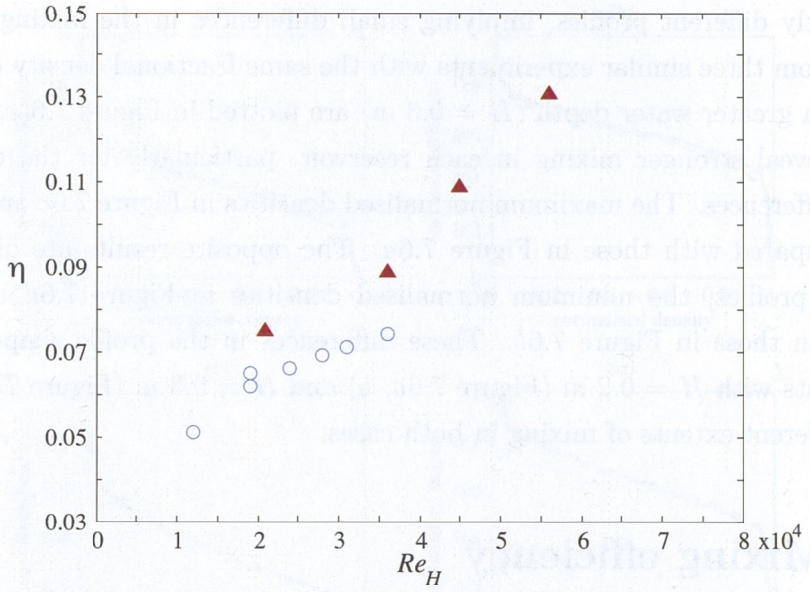

Figure 7.7: The measured mixing efficiencies η plotted against the vertical Reynolds number Re_H for all gravity current experiments. Symbols indicate the experiments with $H = 0.2$ m ($\circ$) and with $H = 0.3$ m ($\triangle$).

to the case of exchange through constrictions, there is no asymptote regime at the Reynolds number achieved. This result remains unexplained, but it is clear that there is a different Reynolds number dependence of mixing efficiency in the gravity currents compared with the hydraulically controlled flows.

We examine a possible role of the flow depth H in the mixing dynamics of the gravity currents by comparing frames from experiments with different water depths. Shown in Figure 7.8 are three pairs of frames from experiments with $H = 0.2$ m and $H = 0.3$ m. Each pair has the same dimensionless x/H, where x represents a distance over which the nose of the current has travelled from the centre of the channel. It is clear from Figure 7.8 that, particularly for the last two pairs (Figure 7.8*b*, *c*), the currents have the same large-scale characteristics in both horizontal and vertical billow scales. However, Figure 7.8(*b*, *c*) reveals differences in the small-scale turbulence occurring at the interface between the layers. These differences may lead to the observed dependence of mixing efficiency on H for a given vertical Reynolds number Re_H.

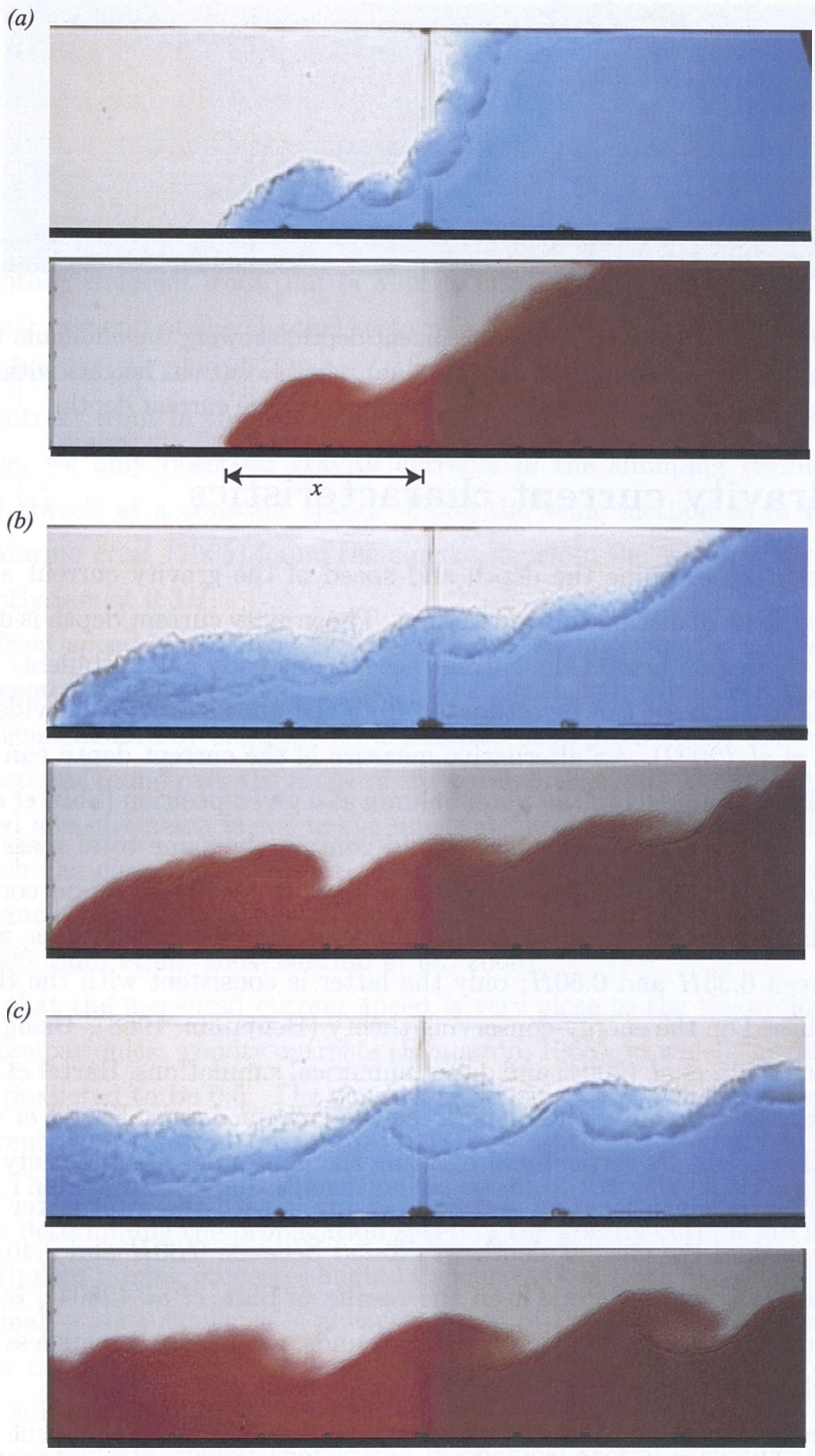

Figure 7.8: Propagating gravity currents having different flow depths from experiment G2 with $H = 0.2$ m and $Re_H = 1.9 \times 10^4$ (blue photos) and experiment G11 with $H = 0.3$ m and $Re_H = 2.1 \times 10^4$ (red photos). Frames (a), (b) and (c) had the dimensionless $x/H = 1.0$, 2.0 and 3.0, respectively, where x was the distance over which the nose had travelled.

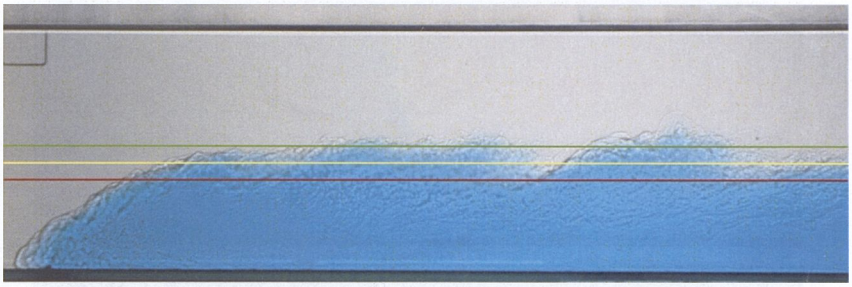

Figure 7.9: Estimate of a gravity current depth, showing the minimum (red solid line) and maximum (green solid line) possible current heights with the average (yellow solid line) being used to represent the current depth.

7.4 Gravity current characteristics

In this section we examine the depth and speed of the gravity current and relate them to the effects of dissipation and mixing. The gravity current depth is difficult to measure as the region behind the current head is unsteady and turbulent. However, the depth of the current can be estimated from the photographic and video record, as in Lowe *et al.* (2002). An alternative measure of the current depth can be based on the total mass anomaly in the water column at a given position (Shin *et al.*, 2004). The depth is taken to be that which would contain the same total mass anomaly if there was no mixing. Using this technique Shin *et al.* (2004) found considerable variations in the current depth across the range of the initial conditions, which was found between $0.35H$ and $0.50H$; only the latter is consistent with the theoretical prediction based on the energy-conserving theory (Benjamin, 1968). Using the same principle as in Shin *et al.* (2004) and direct numerical simulations, Härtel *et al.* (2000) estimated the so-called a 'virtual height' as the current depth. Härtel *et al.* (2000) evaluated this height by vertically integrating the non-dimensional density profile of the flow field at a given location and normalising it with the total water depth H. Using this method the current depth was found between $0.30H$ and $0.40H$. These estimates are not very different from the results of Shin *et al.* (2004), but in part show a fundamental difference on physical grounds, as current heights less than half water depth indicate a loss of energy owing to viscous dissipation.

Here, we use photographs to estimate the depth of the gravity current. For each experiment photographs were taken at times when the nose of the dense current was both far from and nearly at the endwall. We take the the average of the minimum and maximum possible current heights as an estimate for the current depth (Figure 7.9). We compare the depths obtained at different times during an experiment (i.e., in the middle and near the end of the channel) and find that the depth of the current

is approximately constant for a given experiment. For the case of $H = 0.2$ m and $H = 0.3$ m we find that the current depth is estimated between $0.38H$ and $0.47H$, in good agreement with the laboratory results of Shin *et al.* (2004). However, in our experiments the current depths are always less than the half channel depth $H/2$, consistent with expectations for dissipative gravity currents (Härtel *et al.*, 2000).

It is also interesting to note that the experimental set up used in this thesis is fundamentally different from that of Marino *et al.* (2005), in which the barrier was placed near one end of the channel to form a short lock for the saltwater reservoir. While Marino *et al.* (2005) focused on the determination of the characteristics of the gravity current front in the 'self-similar' regime where the current speed decreases with time, we only observed gravity currents in the slumping regime, in which the front travels at a constant speed. Using the same method as in Härtel *et al.* (2000), Marino *et al.* (2005) found the current depth in the self-similar regime to be significantly less at $0.3H$.

The front speed is relatively easily evaluated. As an example, a series of photos of a propagating gravity current (Figure 7.4) show that the dimensionless flow speed (non-dimensionalised by $0.5(g'H)^{1/2}$) is constant at approximately 0.48 ± 0.02. The same speed was found over the range of the parameters used. The uncertainty in the flow speed measurements is due to the uncertainties in measuring both the distance over which the current propagates and the time it takes for the current to travel that distance. The result agrees well with previous laboratory experiments (Hacker *et al.*, 1996; Shin *et al.*, 2004; Marino *et al.*, 2005).

Note that the measured current speed is very close to the theoretical speed for steady, dissipationless gravity currents (Benjamin, 1968), in which the dimensionless speed is predicted to be 0.5. The conditions considered in the present experiments are different from those of Benjamin (1968), owing to the presence of mixing and friction. The nearly constant dimensionless speed of the current indicates that the dynamics determining the propagation speed of the gravity current are independent of the turbulent mixing processes behind the current head and in the trailing current. As the small-scale turbulence is always present in the experiments, there must be some loss of energy associated with turbulent dissipation. Thus the nose speed is not a suitable measure of whether energy is conserved. Instead, the current depth measurements suggest that loss of mechanical energy is significant. The loss of energy is through viscous dissipation and vertical redistribution of density (i.e., mixing). The measured density profiles and calculated mixing efficiencies confirm that a fraction of the potential energy released, on order 10%, is used in irreversibly mixing the two fluids.

Chapter 8

Discussion of results

Vertical mixing plays an important role in maintaining the ocean stratification in the context of the global circulation of ocean waters. In this circulation relatively warm, surface waters are cooled and become dense, then sink in the polar regions. The sinking may be balanced by a broad upward displacement of relatively cold, dense, bottom waters (Munk & Wunsch, 1998; Wunsch & Ferrari, 2004). The upwelling brings the deep waters of the oceans back towards the ocean surface. However, heat must be mixed downwards by turbulence to maintain the interior stratification. The amount of energy required to sustain the mixing, the input of turbulent kinetic energy, is poorly understood and poorly constrained. The fraction of the input used for mixing (i.e., the 'mixing efficiency') is also poorly understood. Thus an understanding of mixing in stably stratified turbulence remains an outstanding and important issue. This thesis has therefore examined a class of flows in which accurate and precise measurements of mixing and mixing efficiency are possible. In the laboratory hydraulic controls (imposed by the topography or geometry) lead to a steady exchange flow and shear-induced mixing, which can be quantified by measuring the change in the density structure. Similar buoyancy-driven exchange flows are commonly found in the oceans, where straits or sills control the exchange of water between adjacent ocean basins. The results will also be more broadly relevant to shear-generated turbulence.

8.1 Mixing efficiency

As mentioned in §2.1, the mixing efficiency is the fraction of the kinetic energy supplied to turbulence, which is in turn irreversibly converted into potential energy of the density field. The remainder of the kinetic energy is dissipated by viscosity.

One measure of the mixing efficiency in stably stratified fluids is the flux Richard-

son number, defined as the ratio of the buoyancy flux to the production of turbulent kinetic energy by shear, or $Ri_f = -\frac{g}{\bar{\rho}}\overline{\rho' w'}/\overline{u_i' w'}\frac{\partial \overline{u}_i}{\partial z}$ (see 2.2). For the case of stably stratified shear flows $Ri_f > 0$, corresponding to a net extraction of turbulent kinetic energy from the mean flow used to irreversibly increase the potential energy of the density distribution. The general results from various studies using theoretical considerations (Linden, 1979), laboratory experiments (Linden, 1980; Rohr *et al.*, 1984) and numerical simulations (Itsweire *et al.*, 1993) show a non-monotonic dependence of the flux Richardson number on the background stratification and vertical shear, suggesting that mixing efficiency is not unique. Current laboratory experiments of turbulent mixing (Monti *et al.*, 2007) have demonstrated that individual turbulent events, associated with the growth and collapse of Kelvin-Helmholtz (KH) billows, in a stratified shear flow lead to time-dependent mixing (see also Patterson *et al.*, 2006). Such a dependence is measured as variations of Ri_f with time (see figure 6 of Monti *et al.*, 2007). Monti *et al.* (2007) found that the mixing efficiency approaches an asymptotic value at large times.

An alternative definition of the mixing efficiency is derived from steady-state energy balance in a turbulent shear flow. Osborn (1980) defined the mixing efficiency as $\Gamma = Ri_f/(1 - Ri_f)$ (see 2.9), which represents the fraction of the total available energy used for mixing relative to that dissipated by viscosity. Osborn (1980) then proposed an asymptotic value of $\sim$0.2 as the upper bound for the mixing efficiency. This value is derived from the critical flux Richardson number of 0.15 (Ellison, 1957), above which the turbulence cannot be sustained. Nevertheless, 0.2 is widely proposed as the mixing efficiency of stratified turbulence, and is used in many previous studies to estimate the total power input required to achieve a designated rate of mixing in the interior of the ocean (Munk & Wunsch, 1998; Webb & Suginohara, 2001; Wunsch & Ferrari, 2004; St. Laurent & Simmons, 2006).

Another definition of the mixing efficiency is proposed by Caulfield & Peltier (2000) and Peltier & Caulfield (2003) for stratified shear flows. Using numerical simulations they have considered a detailed sequence of mixing events that occur during a flow transition from a laminar to a fully turbulent state by examining a full life-cycle of the evolution of KH billows. For a particular time period of the events they defined an 'instantaneous' mixing efficiency as the ratio of mixing rate to the total rates of mixing and dissipation (the same ratio as used in this thesis). This definition is in particular associated with mixing by which the potential energy of the density field is irreversibly increased, and therefore the mixing efficiency defined in this way is always positive. On the other hand, the flux Richardson number Ri_f may be, by definition, positive or negative depending upon the value of the

(reversible) buoyancy flux. While this instantaneous definition provides insight into the physics of mixing, a 'cumulative' mixing efficiency is also of interest as it is more appropriate for practical purposes. The cumulative measure of mixing efficiency corresponds to a sufficiently long integration of mixing rate with respect to time, eliminating contributions that do not correspond to irreversible mixing. Caulfield & Peltier (2000) found that at late times the cumulative mixing efficiency approaches a value of 0.15, somewhat less than the proposed value of ~0.2 (Osborn, 1980).

However, other studies (Stigebrand & Aure, 1989; Arneborg, 2002) have suggested that smaller efficiencies of order 0.1 are possible. In particular, Arneborg (2002) has theoretically investigated turbulent mixing generated in a basin containing an initially linearly stratified fluid. As a result of a mixing event, mixed water is locally produced but eventually spreads out. There is an irreversible increase in potential energy of the fluid. The potential energy increase is used to calculate the flux Richardson number, Ri_f. Arneborg (2002) defined two different flux Richardson numbers to describe the whole mixing process. One of these is used to characterise localised mixing within the turbulent patch and is referred to as the small-scale flux Richardson number. As time proceeds, the mixed fluid in the patch spreads out laterally until the fluid reaches an equilibrium state. In this state the increase in potential energy attributable to mixing is approximately only half of that calculated for the localised patch. The mixing efficiency based on this potential energy increase is defined as the large-scale flux Richardson number, and is a more appropriate quantity with which to compare our results. Thus Arneborg (2002) found that the large-scale flux Richardson number was about half of the small-scale flux Richardson number. Arneborg (2002) has argued that the previously observed larger flux Richardson numbers of order 0.2 should be seen as the small-scale flux Richardson number based on localised turbulent mixing within a patch, and that this is consistent with a large-scale flux Richardson number of $Ri_f = 0.11$ (which corresponds to a bulk mixing efficiency of 0.12).

There have been no previous studies of which we are aware that have directly measured the cumulative (or bulk) efficiency of mixing in stratified exchange flows. To this end we have performed laboratory experiments to determine the mixing efficiency for a range of flow geometries that include lateral contractions and bottom sills. For completeness and comparison, we have also measured the cumulative mixing efficiency in lock-release gravity currents in a uniform channel. The most obvious effect of mixing in all cases is the substantial volume of mixed water in the reservoirs after the experiment. The experimental method provides a measure of the cumulative, irreversible mixing that leads to calculation of the bulk mixing efficiency

in these buoyancy-driven exchange flows (see 4.19), which is similar to the cumulative mixing efficiency used by Caulfield & Peltier (2000) and Peltier & Caulfield (2003) in their numerical simulations for stratified shear flows. However, they did not measure the potential energy of the mean flow in a manner suitable for direct comparison. On the other hand, the method developed here does not allow measurements of the mixing attributable to individual mechanisms or to different localities within the flow. We have, however, observed that the development and maintenance of the turbulence in these flows is due to KH instability and the breakdown into turbulence of the resulting large amplitude vortical structures at the sheared interface. The source of this turbulent kinetic energy is the kinetic energy of the mean shear, in turn sourced from the release of available potential energy.

We have examined the sensitivity of mixing to contraction geometry in the experiments with a constriction, and found only small effects of the geometry on mixing. The measured bulk efficiency of mixing is $\eta = 0.11$ (± 0.01), provided that the horizontal Reynolds number, $Re > 5 \times 10^4$. The primary mechanisms responsible for mixing in the exchange flow are shear instability and hydraulic jumps that are associated with the constriction. The secondary sources include KH billows behind the head of propagating gravity currents in each reservoir, reflections of these currents at the endwalls of the long tank, subsequent reflections of the associated internal bores at the endwalls and replaced barrier and subsequent mixing events due to wave-mean shear and wave-wave interactions in the reservoirs. Many of these processes are generic to the strait-basin configuration, and thus may be present in exchange flows in geophysical environments (although gravity current heads will be absent in the case of steady exchange flows). In addition, observations indicate that the most intense mixing in a controlled exchange flow takes place within the constriction and near the exits of the constriction. Hence, we suggest that the efficiency measured here will characterise mixing more generally in exchange flows. Moreover, the measured bulk efficiency may also characterise mixing in a broader range of two-layer stratified shear flows, where KH billows are again the dominant mechanism causing mixing. In experiments with low Reynolds numbers we find that the shear instability is less efficient at mixing, owing to the absence of continuous small-scale turbulence at the interface.

In exchange flows over simple bottom topography we have found that the mixing efficiency is weakly dependent on the sill geometry. In the extreme case of a weir geometry the measured efficiency is found to increase with horizontal Reynolds number, the Reynolds number based on the horizontal length of the region of flow acceleration, towards an asymptote of approximately $\eta = 0.11$. The highest effi-

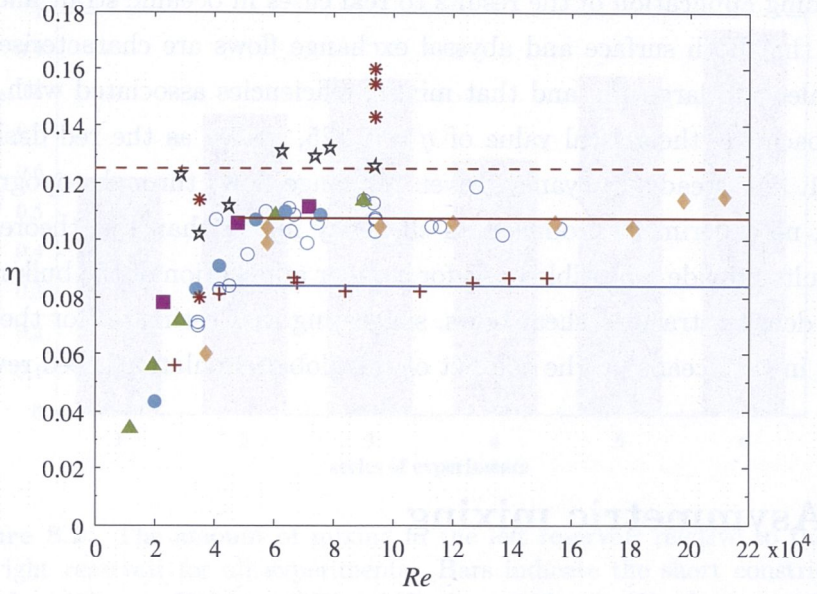

Figure 8.1: The measured mixing efficiencies η as a function of the horizontal Reynolds number Re for all experiments. Symbols indicate $b_o = 20$ mm (blue open $\circ$), 60 mm (green $\triangle$) and 100 mm (pink $\square$) for the short constrictions, $b_o = 60$ mm (yellow $\diamond$) for the the long constriction, experiments with the weir (blue closed $\circ$), with the triangular sill (red $+$), with various run times $\tau > 1.0$ (red $*$) and the rundown cases (black $\star$). The red dashed line shows the theoretical value ($\eta = 0.125$) for the mixing efficiency given by (4.27), the red solid line describes the mean ($\eta = 0.108$) of the measured efficiencies for flows through the constrictions with $\tau \leq 1.0$ and $Re > 5 \times 10^4$ and the blue solid line describes the mean ($\eta = 0.084$) of the measured efficiencies for flows over the triangular sill with $\tau \leq 1.0$ and $Re > 4 \times 10^4$.

ciencies are reached for sufficiently large Reynolds numbers (i.e., $Re > 5 \times 10^4$), in a manner similar to results for exchange flows through constrictions. However, for exchange flows over a triangular sill geometry a smaller asymptotic efficiency of $\eta = 0.08$ has been measured for $Re > 4 \times 10^4$. These results are consistent with the scaling analysis that predicts an upper bound on the mixing efficiency of $\eta = 0.125$, as given in (4.27).

We provide an overview of all experiments conducted in this thesis by plotting in Figure 8.1 the mixing efficiency η for all experiments with topographic constrictions, including those with dimensionless run time $\tau > 1.0$. Larger η were measured for the experiments with $\tau > 1.0$, where endwall reflections cause the meanflow to be unsteady, and possible reasons for this are discussed in §8.2. In the remainder of this section we focus on the results from runs with $\tau \leq 1.0$, in which the exchange flow is steady.

Regarding application of the results to real cases in oceanic strait and sill flows, we argue that both surface and abyssal exchange flows are characterised by large length scales and large Re, and that mixing efficiencies associated with such flows will approach the theoretical value of $\eta = 0.125$, shown as the red dashed line in Figure 8.1. For steady, buoyancy-driven exchange flows through topographic constrictions, no experiment produced an efficiency higher than this theoretical limit. These results provide a possible basis for a wider application of the bulk mixing efficiency to density-stratified shear flows, suggesting that estimates for the energetics of mixing in the oceans, in the context of the global circulation, need revisiting.

8.2 Asymmetric mixing

In this section we re-examine in greater detail the turbulent mixing occurring in each reservoir for all experiments with the topographic constrictions. In general, the exchange flow was either slightly asymmetric about the mid-point of the constriction owing to bottom friction at the channel base and in the left reservoir, or substantially asymmetric as a result of the bottom sill at the centre of the constriction. Here we ask whether asymmetries in the flow lead to asymmetries in mixing behaviour.

The contribution of each reservoir to the overall mixing efficiency in the flow cannot be identified as the available potential energy released P_a (the denominator in 4.19) cannot be unambiguously determined for the separate reservoirs. However, the measured bulk amount of mixing (4.17) can be separated into contributions from each reservoir. The amounts of mixing, P_{m_1} and P_{m_2} in the left and right reservoirs, respectively, can then be written as

$$P_{m_1} = g\int_0^{h_1'} A\rho_1'(z)z\,\mathrm{d}z - g\int_0^{h_{s1}} A\rho_2 z\,\mathrm{d}z - g\int_{h_{s1}}^{h_1'} A\rho_1 z\,\mathrm{d}z \tag{8.1}$$

and

$$P_{m_2} = g\int_0^{h_2'} A\rho_2'(z)z\,\mathrm{d}z - g\int_0^{h_{s2}} A\rho_2 z\,\mathrm{d}z - g\int_{h_{s2}}^{h_2'} A\rho_1 z\,\mathrm{d}z, \tag{8.2}$$

where all flow variables are the same as those previously defined in §4.3. The left reservoir in all cases initially contained less dense water, and the right reservoir contained denser salt solution. We here aim to compare (8.1) with (8.2). For this purpose we define the relative amount of mixing P_{m_r} as

$$P_{m_r} = \frac{P_{m_1}}{P_{m_2}}. \tag{8.3}$$

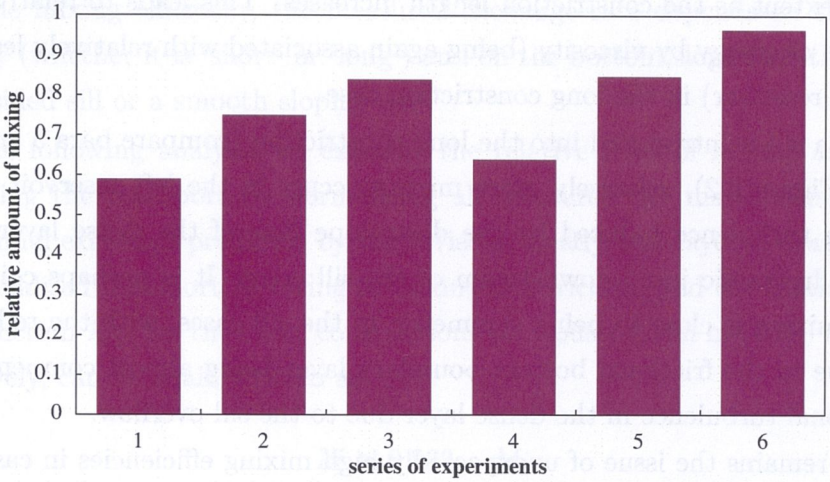

Figure 8.2: The amount of mixing in the left reservoir relative to that in the right reservoir for all experiments. Bars indicate the short constriction with $b_o = 20$ mm (1), $b_o = 60$ mm (2), $b_o = 100$ mm (3), the long 60 mm wide constriction (4), the weir (5) and the triangular sill (6). Data include all experiments listed in Tables 3.1 through Table 3.4.

We plot P_{m_r} for six different types of experiments with $\tau \leq 1.0$ as bar diagrams in Figure 8.2. The diagrams show the results for the average of this mixing ratio across many experiments and over the ranges of the Reynolds number used for each type of experiment.

It is clear from Figure 8.2 that the mixing in all cases is asymmetric with relatively less mixing in the left reservoir. The greatest relative difference in mixing is found in the narrowest constriction ($b_o = 20$ mm), where mixing in the left reservoir is about 60% of that in the right reservoir. The most symmetric case is the triangular sill, where approximately the same amount of mixing occurs in each reservoir.

The asymmetric mixing in the short constriction case is most likely associated with the frictional boundary layer at the bottom of the left reservoir, where a greater fraction of the turbulent kinetic energy is viscously dissipated, leading to a smaller amount of mixing in the left reservoir (compared with the right reservoir). The effect of the asymmetric boundary condition is found to be greater in the narrower constriction (see bars 1, 2 and 3 in Figure 8.2). For the short constrictions the flow is thinner when the constriction is narrower, leading to relatively more viscous dissipation, hence a relatively less amount of mixing in the left reservoir.

For the case of constrictions having the same minimum width ($b_o = 60$ mm) but different geometries (bars 2 and 4 in Figure 8.2), the greater mixing asymmetry occurs in the long constriction (bar 4) because all frictional boundary layers grow to

a greater extent as the constriction length increases. This leads to relatively more dissipation of energy by viscosity (being again associated with relatively less mixing in the left reservoir) in the long constriction case.

When a sill is introduced into the long constriction (compare bars 5 and 6 with bar 4 in Figure 8.2), relatively more mixing occurs in the left reservoir owing to the strong turbulence induced by the downslope flow of the dense layer and the persistent hydraulic jump downstream of the sill crest. It is perhaps coincidental that the mixing is close to being symmetric in the sill cases, with the reduction of mixing due to the frictional bottom boundary layer being almost compensated for by additional turbulence in the dense layer due to the sill overflow.

There remains the issue of unexpectedly high mixing efficiencies in cases where $\tau > 1.0$ (see red asterisks in Figure 8.1). A complete understanding of the complexities of these unsteady exchange flows is beyond the scope of this thesis. However, we offer some speculative explanation. When the dense current from the right reservoir enters the left reservoir through the constriction, this current is mixed with the bottom water of the left reservoir to form weakly stratified layers. If the flow is allowed to continue after the first reflection from the endwalls, the current flows beneath a much weaker stratification (i.e., a region of small values of N^2). If we assume this current has the same speed as in experiments with shorter run times (i.e., $\tau \leq 1.0$), and note that flow at the constriction cannot change for $\tau \lesssim 2$, then we may expect the rate of the turbulent dissipation ε to be unchanged. If we further assume the turbulent Froude number previously defined in (2.12) is such that $Fr_T \approx 1$, then the turbulent Reynolds number Re_T can be written as $Re_T \approx \varepsilon/\nu N^2$ (see 2.13), leading to a larger value of Re_T in these cases. The larger turbulent Reynolds number may explain the higher efficiencies, with the highest efficiency being in the order of 0.16 (red asterisks in Figure 8.1). These results are also consistent with the measurement of Ivey & Nokes (1989) (see also figure 7 of Ivey & Imberger, 1991). In addition, the reflected bore, now propagating upstream against the gravity current, will locally increase velocity gradients.

8.3 Mass transport

In this section we focus on the effects of turbulent mixing on the rate of exchange of water. As a by product of the mixing efficiency measurements we have also measured the rate at which water of different density is exchanged through the channel. When mixing occurs the horizontal transport is reduced from the maximum possible value predicted by the idealised, steady, two-layer hydraulic theory. We have found that,

unlike the mixing efficiency, the measured exchange rate depends on the channel geometry (whether it is 'short' or 'long') and on the bottom slope (whether there is a steep-sided sill or a smooth sloping sill).

In the following analysis we examine the relative roles of mixing and friction in reducing the transport by normalising all measured net mass transports with the maximal exchange predicted by the inviscid, steady, two-layer hydraulic theory. The normalised transport M owing to mixing and friction, and the frictional transport reduction M_{fri} for the short constrictions previously given in (4.30) and (4.33), respectively, can be again written as

$$M \approx 0.833 - M_{\text{fri}} \tag{8.4}$$

and

$$M_{\text{fri}} \sim Re^{-1/2} \left(2\frac{L_c}{b_{\text{ef}}} + \frac{L_c}{H} \right). \tag{8.5}$$

Equation (8.4) predicts the transport in an exchange flow through a simple geometry, with a single control point only. The normalised transport is, in the absence of friction, $M \approx 0.833$ with a further reduction by frictional effects given by (8.5), which is, for a given water depth H, weakly dependent on the Reynolds number but strongly dependent on the channel geometry and shape.

We plot the results of the measured net mass transports for all experiments in Figure 8.3. The theoretical upper bound on the transports ($M = 0.833$) predicted for an exchange flow with mixing (but neglecting friction) is shown as the red solid line. In the case of the short constrictions the measured transport is reduced to approximately $M = 82\%$ (red dashed line) of the maximal hydraulic solution (2.21), independent of the external parameters used. As noted earlier this is, to first order, well predicted by just the first term on the right-hand side of (8.4). The implication of this result is that mixing is primarily responsible for the decrease in flux, with a relatively small reduction in the transport of up to 2%, owing to friction. These measurements are in good agreement with the laboratory measurements of Helfrich (1995). The normalised transport corresponds to a 13% volume flux reduction, consistent with the 15% reduction in the volume flux in previous numerical simulations (Winters & Seim, 2000; Stenström, 2003).

It should be noted that the scaling arguments in (8.4) and (8.5) have been developed for the special case in which the topographic and virtual control points are effectively located at the same (narrowest) point in the constriction, as is the case for our short constrictions. For the long constriction and sill cases we have found that the normalised transports lie somewhat below the upper bound (see

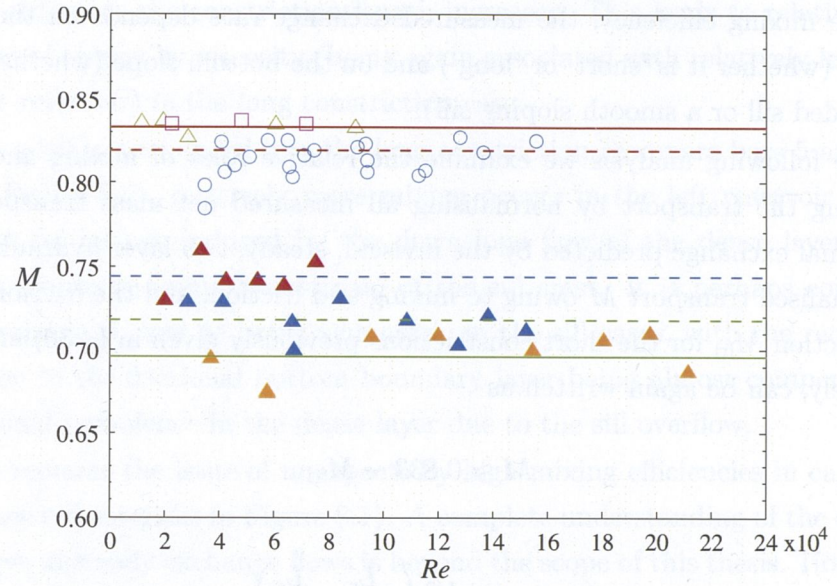

Figure 8.3: The normalised transport M as a function of the horizontal Reynolds number Re for all experiments. Open symbols correspond to experiments with a short constriction and closed symbols correspond to those with a long constriction. All triangular ($\triangle$) symbols describe experiments with $b_o = 60$ mm (regardless of channel geometry). For the short constrictions symbols represent $b_o = 20$ mm ($\circ$), $b_o = 60$ mm ($\triangle$) and $b_o = 100$ mm ($\square$). For the long constriction symbol indicates $b_o = 60$ mm (yellow $\triangle$). For the sill flows symbols describe the weir (red $\triangle$) and the triangular sill (blue $\triangle$). The red solid line shows the theoretically predicted value ($M = 0.833$) with mixing but no friction for the normalised transport through the short constrictions (8.4), and all other lines describe the mean of the measured transports: the red dashed line ($M = 0.819$) for the short constrictions, the green solid line ($M = 0.696$) for the long constriction, the blue dashed line ($M = 0.744$) for the weir and the green dashed line ($M = 0.718$) for the triangular sill.

Figure 8.3). These findings raise two crucial questions. How much do frictional effects contribute to the total transport reduction? And what is the role of channel geometry (or shape) in the transport reduction?

For the long constriction the measured transport is reduced to approximately $M = 70\%$ (green solid line in Figure 8.3) of the idealised hydraulic solution (2.21). The role of bottom topography in reducing the transport has also been examined by placing the weir or the triangular sill at the centre of the long constriction. It is shown in Figure 8.3 that for the weir and triangular sill the measured transports are $M = 74\%$ (blue dashed line) and $M = 72\%$ (green dashed line), respectively, relative to the maximal exchange for the sill flows (2.23). If this reduction in flux is to be explained by (8.4), then M_{fri} must be of $\sim$10%. However, (8.5) predicts a

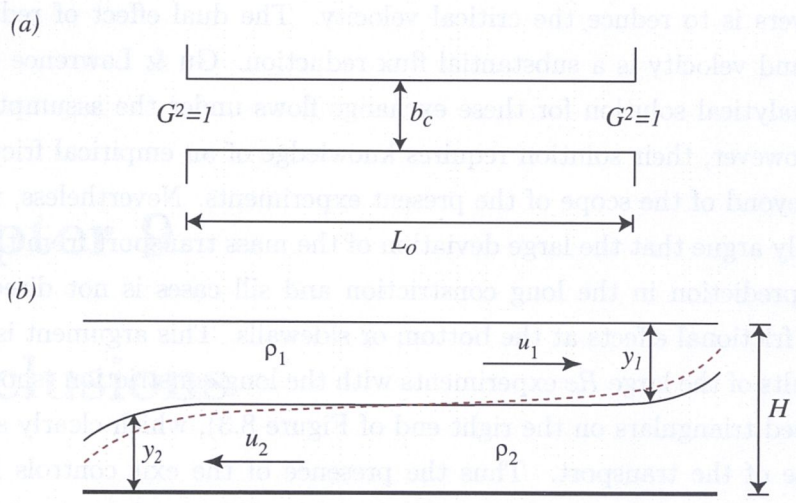

Figure 8.4: (*a*) Plan view of the constant width channel in frictional exchange flows of Gu & Lawrence (2005), where b_c and L_o are the minimum width and length of the channel, respectively. (*b*) Side view of the flow configuration, showing the altered interface (dashed line) along the constriction straight central section and the interface for the inviscid, steady, two-layer hydraulic solution (solid line).

Re dependence of the transport which is not present in the data from cases with a long constriction. The implication is that (8.4) and (8.5) do not fully explain the transport reduction observed in these cases. We thus hypothesise that the larger transport reduction in cases with a long constriction (compared with the short constrictions) is due to the geometry of the channel, as well as the influence of friction.

The inviscid hydraulic solution for the ideal case of steady, two-layer exchange flows is independent of channel length, meaning that transcritical conditions occur at the exit points of the straight section in the long constriction case (the so-called 'exit controls'). The influence of friction in flows with exit controls has been recognised by Anati *et al.* (1977) and further examined in detail by Gu & Lawrence (2005). Here we discuss only the laboratory experiments of Gu & Lawrence (2005). Using a constricted channel of constant width and depth (Figure 8.4*a*) they demonstrate that a significant component of the reduction in mass transport is associated with the loss of energy in the constant width section of the constriction (between the separate control points), which alters the interface height at each of the exit controls (Figure 8.4*b*). The interface heights change in such a way as to reduce layer thickness at both of these exit control points, but the critical condition (the composite Froude number $G^2 = 1$) is unchanged. Thus, (2.17) implies that the secondary effect of

thinner layers is to reduce the critical velocity. The dual effect of reducing layer thickness and velocity is a substantial flux reduction. Gu & Lawrence (2005) also gave an analytical solution for these exchange flows under the assumption of zero mixing. However, their solution requires knowledge of an empirical friction factor, which is beyond of the scope of the present experiments. Nevertheless, we can still qualitatively argue that the large deviation of the mass transport from the maximal hydraulic prediction in the long constriction and sill cases is not directly due to additional frictional effects at the bottom or sidewalls. This argument is supported by the results of the large Re experiments with the long constriction (shown as three yellow closed triangulars on the right end of Figure 8.3), which clearly show no Re dependence of the transport. Thus the presence of the exit controls in the long constriction and sill cases is, in combination with mixing and friction, the primary mechanism for the large reduction in the transport.

Chapter 9

Conclusions

9.1 Mixing efficiency

The primary aim of this thesis is to determine the amount of turbulent mixing, hence the overall efficiency of the mixing, in hydraulically-controlled, two-layer exchange flows through topographic constrictions between two large reservoirs of water with different densities. These constrictions include lateral contractions and bottom sills (described in §3.1). In addition, we have also measured the mixing efficiency in lock-release gravity currents produced in a uniform channel of constant width and depth.

In experiments with a controlled flow we have found that the steady shear at the interface between the layers led to the generation of Kelvin-Helmholtz (KH) billows and persistent, small-scale turbulence within the constriction. The source of energy for the turbulence is the available potential energy in the initial density field. A fraction of this turbulent kinetic energy is used to irreversibly mix the two fluids, thereby reducing the loss of potential energy. The proportion of the turbulent kinetic energy that goes into mixing is known as the mixing efficiency.

The sensitivity of both the mixing efficiency and the mass exchange flux to constriction geometry was examined. The overall mixing efficiency for flows through the lateral contractions (discussed in §5.3) and flow over the weir (discussed in §6.3) is found to asymptote a constant value of $\eta = 0.11 \pm 0.01$ at high Re, independent of the external parameters and initial conditions. For the triangular sill case (discussed in §6.3) the bulk mixing efficiency is measured to be $\eta = 0.08$ at high Re, again independent of the parameters used. These results are consistent with the theoretical prediction for the mixing efficiency, $\eta = 0.125$ given in (4.27) as the upper bound of the efficiency for the steady exchange flows (shown as the red dashed line in Figure 8.1). The measured efficiencies are also significantly less than 0.2, the widely

proposed value of the mixing efficiency for steady, stratified turbulence (Osborn, 1980). Smaller mixing efficiencies are observed in relatively low Re experiments, owing to intermittent turbulence and greater viscous dissipation. The results for the bulk efficiency in the limit of large Re is thought to be relevant to the large-scale ocean strait flows.

Several possible mixing mechanisms contribute to the bulk mixing rate in these experiments, and hence determine the overall mixing efficiency. These include shear instability and hydraulic jumps as the principal mechanisms and all other secondary sources associated with propagating gravity currents in the reservoirs and gravity current reflections at the endwalls. We observe that the most energetic mixing takes place within the constriction, owing to shear instability and hydraulic jumps. We argue that the bulk efficiency measured here is a useful and relevant characterisation of mixing in buoyancy-driven exchange flows.

The results are expected to be applicable to oceanic strait flows as these flows are in the limit of large Re. Hence, the mixing efficiency in such flows will approach the theoretical upper bound of the efficiency, $\eta = 0.125$, fairly close to 0.15 obtained from numerical computations (Caulfield & Peltier, 2000; Peltier & Caulfield, 2003). As the development of KH billows is observed to be the dominant mixing mechanism in the oceans, the results also provide insight into a broader range of density-stratified shear flows and may also be applicable to a wider range of oceanographic settings. While the results are supported by theoretical work (Arneborg, 2002), there remains discrepancies between the current results and those of previous studies (Rohr *et al.*, 1984; Imberger & Ivey, 1991; Monti *et al.*, 2007). These studies have mostly found that the mixing efficiency asymptotes to the canonical value of $\sim$0.2, which is frequently used in estimating the energy budget of the ocean circulation. For example, it is often assumed that 20% of the turbulent kinetic energy in the abyssal ocean is irreversibly converted into potential energy of the density field (Munk & Wunsch, 1998; Webb & Suginohara, 2001; Wunsch & Ferrari, 2004). However, the smaller asymptotic mixing efficiency obtained here, along with computational results (Caulfield & Peltier, 2000; Peltier & Caulfield, 2003), raises the possibility that the average mixing efficiency in the oceans may not be as large as widely assumed.

9.2 Mass transport

In the process of determining the mixing efficiency we have also measured the rate at which water of different density is exchanged through a constriction. In the

limit of inviscid, two-layer hydraulic theory no mixing occurs. A departure from the maximum possible exchange flux predicted by the idealised hydraulic solution occurs when mixing and friction are present in the flow. We find that, unlike the mixing efficiency, the transport is dependent on the channel geometry.

We have developed scaling arguments to predict the reduction of net mass transport owing to both mixing and friction in (4.30). The prediction is applicable to cases with a single control point only, such as the short constrictions in the present experiments. In the absence of friction the predicted upper bound on the transport is 83.3% of the maximal hydraulic transport (red solid line in Figure 8.3). For the short constrictions the observed transport is approximately constant at 82% of the maximal hydraulic solution (2.21), independent of the external parameters and initial conditions. This suggests that the additional reduction in the transport owing to friction is relatively small – up to 2% in the short constrictions. The result agrees well with the laboratory work of Helfrich (1995). For the long constriction the transport is much less than the theoretical upper bound of 83.3%, owing to the combined influence of friction and the spatially separated control points. In this geometry the measured transport is reduced to approximately 70% of the maximal hydraulic solution (2.21), again independent of the parameters used.

Similar results for the transport are obtained for other geometries. The measured transport over the weir is 74% of the maximal hydraulic value, slightly larger than the 72% measured over the triangular sill. The transport reduction below that predicted with mixing alone is, again, presumably due to the combined effects of friction and exit controls. A full solution to the question of what role channel geometry plays in governing the transport remains unresolved. However, the theoretical prediction of the hydraulically-controlled transport (4.30), including mixing and friction, can be used to estimate the transport in cases with a simple geometry, such as a pure, lateral constriction.

9.3 Further work

Many questions remain unanswered regarding the dynamics of mixing in buoyancy-driven exchange flows generated in the laboratory. In particular, how widely applicable are the mixing efficiency measurements to density-stratified shear flows commonly found in the oceans. The laboratory tank, which has been used for the measurements of the mixing presented here, could be utilised to examine exchange flows over a pure sill (hence no lateral contraction) in order to test further the sensitivity of the mixing process to channel geometry. The scaling analysis developed

here for prediction of mixing efficiency in flows through a constriction can serve as a starting point to predict the results for such a sill flow. As the theoretical prediction of the mixing efficiency is independent of channel geometry, equation (4.27) is expected to work reasonably well if the sill is full-width. This hypothesis needs to be clarified in further work.

Another issue that needs to be addressed in future studies is the physical reasons behind the large reduction in the transport for flows with exit controls. This seems difficult to do in the laboratory, but may be possible to handle using a combination of theoretical development and numerical simulations. It needs to be determined whether an increase in viscosity (or friction) could separate the coincident control points (originally at the narrowest or shallowest point), and whether spatially separated control points alter the characteristics of turbulence in the region of the constriction.

There is scope to utilise the present measurement and analysis methods to more fully examine the energetics of gravity current flows. We have studied only the case of two equal reservoirs. However, the more general cases of differing lock sizes and differing release volumes can be explored. Finally, it may be possible to reach a better understanding of controlled exchange flows and the contributions to mixing by the gravity current within each reservoir through a study of the energetics of gravity currents in the uniform channel. The mixing owing to the gravity currents in the reservoirs might then be separated from the mixing more directly associated with flow through the constriction.

Appendix A

Energy balance in stratified turbulent shear flows

In this appendix we examine kinetic energy budgets and the energetics of mixing, from which the steady-state energy balance in a stratified turbulent shear flow is obtained. This balance is important as it provides insight into how kinetic and potential energies are exchanged in the flow, and provides a basis for the definition of mixing efficiencies. As mentioned in §2.1 several definitions of mixing efficiency have been used in previous studies (e.g., Osborn, 1980; Ivey & Imberger, 1991; Strang & Fernando, 2001*b*).

We here consider a Boussinesq fluid in which density variations in a flow can be neglected except in the terms that give rise to buoyancy forces. Thus the effect of such density variations enters only in the vertical momentum equation. In such a flow the equation of continuity can be written in, for simplicity, a Cartesian coordinate system as follows,

$$\frac{\partial \rho}{\partial t} + \nabla . \rho \mathbf{u} = 0, \tag{A.1}$$

where $\mathbf{u} = (u,\ v,\ w)$ is the velocity vector, ρ is the density at a given space and time, and an operator ∇ is defined as

$$\nabla = \hat{\mathbf{x}}\frac{\partial}{\partial x} + \hat{\mathbf{y}}\frac{\partial}{\partial y} + \hat{\mathbf{z}}\frac{\partial}{\partial z}. \tag{A.2}$$

Note that symbols in bold are vectors, whereas italic symbols denote scalars.

The continuity equation represents mass conservation, and can also be written in the form of

$$\frac{D\rho}{Dt} + \rho \nabla . \mathbf{u} = 0, \tag{A.3}$$

where we have used the definition of the material derivative,

$$\frac{D}{Dt} = \frac{\partial}{\partial t} + \mathbf{u}.\nabla. \tag{A.4}$$

The fluid can commonly be assumed incompressible, hence the density remains constant following the motion, namely $D\rho/Dt = 0$. This, along with (A.3), leads to

$$\nabla.\mathbf{u} = 0, \tag{A.5}$$

implying that volume is conserved in the flow.

A.1 Kinetic energy budgets

A full-detailed description of the dynamics of turbulence is given in ch.3 of Tennekes & Lumley (1972). Here, we discuss kinetic energy budgets in a stratified fluid and derive the steady-state energy balance for stratified turbulence (Osborn, 1980), from which an alternative definition of mixing efficiency previously described in (2.9) is introduced.

We decompose both vector and scalar fields into ensemble-mean and fluctuating components to account for the effects of turbulent motion on the mean flow as follows,

$$u = \overline{u} + u', \qquad v = \overline{v} + v', \qquad w = \overline{w} + w', \tag{A.6}$$

and

$$\rho = \overline{\rho} + \rho', \qquad p = \overline{p} + p', \qquad b = \overline{b} + b', \tag{A.7}$$

where symbols with overbars are used for ensemble-mean values and prime symbols denote time-fluctuating parts with zero mean.

A.1.1 Kinetic energy of the mean flow

We write the momentum equation for the mean flow as

$$\frac{\partial \overline{\mathbf{u}}}{\partial t} + (\overline{\mathbf{u}}.\nabla)\overline{\mathbf{u}} + \overline{(\mathbf{u}'.\nabla)\mathbf{u}'} = -\frac{1}{\rho_o}\nabla\overline{p} + \nu\nabla^2\overline{\mathbf{u}} + \overline{b}\hat{\mathbf{z}} - f\hat{\mathbf{z}} \times \overline{\mathbf{u}}, \tag{A.8}$$

where p is the pressure, ν is the kinematic viscosity, $\overline{b} = -g(\overline{\rho} - \rho_o)/\rho_o$ is the buoyancy, g is the acceleration due to gravity, ρ_o is the reference density, f is the Coriolis frequency and $\hat{\mathbf{z}}$ is the unit vector in the vertical direction. Note that the rotation axis is assumed to be in the vertical direction. The x-component of (A.8)

is

$$\frac{\partial \overline{u}}{\partial t} + (\overline{\mathbf{u}}.\nabla)\overline{u} + \overline{(\mathbf{u}'.\nabla)u'} = -\frac{1}{\rho_o}\frac{\partial \overline{p}}{\partial x} + \nu\nabla^2\overline{u} + f\overline{v}, \tag{A.9}$$

where we have used $\overline{\mathbf{u}} = \hat{\mathbf{x}}\overline{u} + \hat{\mathbf{y}}\overline{v} + \hat{\mathbf{z}}\overline{w}$ to calculate $\hat{\mathbf{z}} \times \overline{\mathbf{u}} = \hat{\mathbf{y}}\overline{u} - \hat{\mathbf{x}}\overline{v}$. Multiplying (A.9) by $\overline{u}$ yields

$$\overline{u}\frac{\partial \overline{u}}{\partial t} + \overline{u}(\overline{\mathbf{u}}.\nabla)\overline{u} + \overline{u}\overline{(\mathbf{u}'.\nabla)u'} = -\frac{\overline{u}}{\rho_o}\frac{\partial \overline{p}}{\partial x} + \nu\overline{u}\nabla^2\overline{u} + f\overline{u}\,\overline{v}. \tag{A.10}$$

Substituting the identity relations below,

$$\overline{u}\frac{\partial \overline{u}}{\partial t} = \frac{\partial}{\partial t}\left(\frac{\overline{u}^2}{2}\right), \tag{A.11}$$

$$\overline{u}(\overline{\mathbf{u}}.\nabla)\overline{u} = \overline{\mathbf{u}}.\overline{u}\nabla\overline{u} = \overline{\mathbf{u}}.\nabla\left(\frac{\overline{u}^2}{2}\right) \tag{A.12}$$

and

$$\overline{u}\overline{(\mathbf{u}'.\nabla)u'} = \nabla.(\overline{\mathbf{u}'u'}\,\overline{u}) - \overline{u'\mathbf{u}'}.\nabla\overline{u} \tag{A.13}$$

into (A.10) gives

$$\left(\frac{\partial}{\partial t} + \overline{\mathbf{u}}.\nabla\right)\frac{\overline{u}^2}{2} = -\frac{\overline{u}}{\rho_o}\frac{\partial \overline{p}}{\partial x} + \nu\overline{u}\nabla^2\overline{u} + f\overline{u}\,\overline{v} - \nabla.(\overline{\mathbf{u}'u'}\,\overline{u}) + \overline{u'\mathbf{u}'}.\nabla\overline{u}. \tag{A.14}$$

Then applying simple relations,

$$\frac{1}{\rho_o}\frac{\partial}{\partial x}\overline{p}\,\overline{u} = \frac{\overline{p}}{\rho_o}\frac{\partial \overline{u}}{\partial x} + \frac{\overline{u}}{\rho_o}\frac{\partial \overline{p}}{\partial x} \tag{A.15}$$

and

$$\nabla^2\left(\frac{\overline{u}^2}{2}\right) = \overline{u}\nabla^2\overline{u} + \nabla\overline{u}.\nabla\overline{u} \tag{A.16}$$

to (A.14) results in the x-component contribution of the velocity field to the kinetic energy of the mean flow as follows,

$$\begin{aligned}\frac{D}{Dt}\left(\frac{\overline{u}^2}{2}\right) = -\frac{1}{\rho_o}\frac{\partial}{\partial x}\overline{p}\,\overline{u} + \frac{\overline{p}}{\rho_o}\frac{\partial \overline{u}}{\partial x} + \nu\nabla^2\left(\frac{\overline{u}^2}{2}\right) - \nu\nabla\overline{u}.\nabla\overline{u} \\ + f\overline{u}\,\overline{v} - \nabla.(\overline{\mathbf{u}'u'}\,\overline{u}) + \overline{u'\mathbf{u}'}.\nabla\overline{u}.\end{aligned} \tag{A.17}$$

The other contributions to the kinetic energy of the mean flow are associated with the y and z components of the velocity field. The y-component contribution of the velocity field to the kinetic energy of the mean flow can be obtained using the same

technique, and is written as

$$\frac{D}{Dt}\left(\frac{\overline{v}^2}{2}\right) = -\frac{1}{\rho_o}\frac{\partial}{\partial y}\overline{p}\,\overline{v} + \frac{\overline{p}}{\rho_o}\frac{\partial \overline{v}}{\partial y} + \nu\nabla^2\left(\frac{\overline{v}^2}{2}\right) - \nu\nabla\overline{v}.\nabla\overline{v} - f\overline{u}\,\overline{v} - \nabla.(\overline{\mathbf{u}'v'}\,\overline{v}) + \overline{v'\mathbf{u}'}.\nabla\overline{v}. \tag{A.18}$$

Note that the Coriolis term in (A.18) is the opposite sign to that in (A.17), canceling each other, hence the planetary rotation has no contributions to the total kinetic energy of the mean flow. The z-component contribution of the velocity field to the the mean flow has a different form from the other two (x and y) component contributions as the Coriolis force is absent in the vertical direction. Rather, a buoyancy term is now introduced as the gravity is aligned with the vertical. Therefore we have

$$\frac{D}{Dt}\left(\frac{\overline{w}^2}{2}\right) = -\frac{1}{\rho_o}\frac{\partial}{\partial z}\overline{p}\,\overline{w} + \frac{\overline{p}}{\rho_o}\frac{\partial \overline{w}}{\partial z} + \nu\nabla^2\left(\frac{\overline{w}^2}{2}\right) - \nu\nabla\overline{w}.\nabla\overline{w} + \overline{w}\,\overline{b} - \nabla.(\overline{\mathbf{u}'w'}\,\overline{w}) + \overline{w'\mathbf{u}'}.\nabla\overline{w}, \tag{A.19}$$

where $\overline{wb}$ is the buoyancy transport term, through which the large-scale potential energy is converted into kinetic energy of the mean flow.

The full form of the kinetic energy equation for the large-scale (mean) flow is obtained by summing up (A.17) through (A.19) and writing the result in the form of summation indices as follows,

$$\frac{D}{Dt}\left(\frac{\overline{u_i}^2}{2}\right) = \frac{\partial}{\partial x_j}\left(-\frac{1}{\rho_o}\overline{p}\,\overline{u_i}\delta_{ij} + \nu\frac{\partial}{\partial x_j}\frac{\overline{u_i}^2}{2} - \overline{u_j'u_i'}\,\overline{u}_i\right) - \nu\left(\frac{\partial \overline{u_i}}{\partial x_j}\right)^2 + \overline{u_j'u_i'}\frac{\partial \overline{u_i}}{\partial x_j} + \overline{w}\,\overline{b}, \tag{A.20}$$

where δ_{ij} is the Kronecker delta ($\delta_{ij} = 1$ for $i = j$ and $\delta_{ij} = 0$ for $i \neq j$) and we have used $\partial\overline{u}/\partial x + \partial\overline{v}/\partial y + \partial\overline{w}/\partial z = 0$. Note that the first term on the right-hand side of (A.20) represents work done by pressure gradient. The second and third terms are transports by viscous and Reynolds stresses, respectively. The fourth term is viscous dissipation and the fifth term is shear production, representing transfer of kinetic energy from the mean flow to the turbulent flow. The last term is the large-scale buoyancy production.

A.1.2 Kinetic energy of the turbulent flow

Although the kinetic energy budget of the mean flow offers insight into the dynamics of the large-scale motion, it gives no more information than the momentum equation

does for the mean flow. For this reason we consider kinetic energy of the turbulent flow. We use the same technique as in §A.1.1 to consider the contribution of each velocity component to the turbulent kinetic energy. The x-component contribution is obtained by first writing

$$\frac{\partial u'}{\partial t} = \frac{\partial u}{\partial t} - \frac{\partial \overline{u}}{\partial t}. \tag{A.21}$$

Multiplying (A.21) by u' yields

$$u'\frac{\partial u'}{\partial t} = u'\frac{\partial u}{\partial t} - u'\frac{\partial \overline{u}}{\partial t}. \tag{A.22}$$

Then taking the average of (A.22) gives

$$\overline{u'\frac{\partial u'}{\partial t}} + \overline{u'(\overline{\mathbf{u}}.\nabla)u'} + \overline{u'(\mathbf{u}'.\nabla)u'} = -\overline{\frac{u'}{\rho_o}\frac{\partial p'}{\partial x}} + \nu\overline{u'\nabla^2 u'} + f\overline{u'v'}. \tag{A.23}$$

Following the same procedure as described in §A.1.1 (which give us A.11 through A.16) and using simple relations below,

$$\overline{\frac{\partial u}{\partial x}} = \frac{\partial \overline{u}}{\partial x}, \qquad \overline{\frac{\partial u'}{\partial x}} = \frac{\partial \overline{u}'}{\partial x} = 0, \qquad \frac{\partial \overline{u'u'}}{\partial x} \neq 0, \tag{A.24}$$

we obtain the contribution from the x-component of the velocity field to the turbulent kinetic energy of the flow,

$$\begin{aligned}\frac{D}{Dt}\left(\frac{\overline{u'^2}}{2}\right) = &-\frac{1}{\rho_o}\frac{\partial}{\partial x}\overline{p'u'} + \frac{1}{\rho_o}\overline{p'\frac{\partial u'}{\partial x}} + \nu\nabla^2\left(\frac{\overline{u'^2}}{2}\right) - \nu\overline{\nabla u'.\nabla u'} \\ &+ f\overline{u'v'} - \nabla.\left(\frac{\overline{\mathbf{u}'u'^2}}{2}\right) - \overline{u'\mathbf{u}'}.\nabla\overline{u},\end{aligned} \tag{A.25}$$

the y-component contribution of the velocity field to the turbulent kinetic energy of the flow,

$$\begin{aligned}\frac{D}{Dt}\left(\frac{\overline{v'^2}}{2}\right) = &-\frac{1}{\rho_o}\frac{\partial}{\partial y}\overline{p'v'} + \frac{1}{\rho_o}\overline{p'\frac{\partial v'}{\partial y}} + \nu\nabla^2\left(\frac{\overline{v'^2}}{2}\right) - \nu\overline{\nabla v'.\nabla v'} \\ &- f\overline{u'v'} - \nabla.\left(\frac{\overline{\mathbf{u}'v'^2}}{2}\right) - \overline{v'\mathbf{u}'}.\nabla\overline{v},\end{aligned} \tag{A.26}$$

and the z-component contribution,

$$\frac{D}{Dt}\left(\frac{\overline{w'^2}}{2}\right) = -\frac{1}{\rho_o}\frac{\partial}{\partial z}\overline{p'w'} + \frac{1}{\rho_o}\overline{p'\frac{\partial w'}{\partial z}} + \nu\nabla^2\left(\frac{\overline{w'^2}}{2}\right) - \nu\overline{\nabla w'.\nabla w'} + \overline{w'b'} - \nabla.\left(\frac{\overline{\mathbf{u}'w'^2}}{2}\right) - \overline{w'\mathbf{u}'}.\nabla\overline{w}. \qquad \text{(A.27)}$$

After summing up (A.25) through (A.27), we obtain the full turbulent kinetic energy equation as follows,

$$\frac{D}{Dt}\left(\frac{\overline{u_i'^2}}{2}\right) = \frac{\partial}{\partial x_j}\left(-\frac{1}{\rho_o}\overline{p'u_i'}\delta_{ij} + \nu\frac{\partial}{\partial x_j}\frac{\overline{u_i'^2}}{2} - \overline{u_j'u_i'u_i'}\right) - \nu\overline{\left(\frac{\partial u_i'}{\partial x_j}\right)^2} - \overline{u_j'u_i'}\frac{\partial\overline{u_i}}{\partial x_j} + \overline{w'b'}, \qquad \text{(A.28)}$$

which complements that in (A.20). Note that the first three terms on the right-hand side of (A.28) are similar to those in (A.20). The first term is pressure work, the second and third terms represent the transports via viscous and Reynolds stresses, respectively. The fourth term shows viscous dissipation, which is always negative representing a loss of turbulent kinetic energy. The fifth term is, again, the shear production but has the opposite sign to that in (A.20), implying no net loss of total kinetic energy, but an exchange between the mean and turbulent flows. The last term is the buoyancy production, representing conversion from potential energy to turbulent kinetic energy.

A.2 Energetics of mixing

The relative importance of the terms in (A.28) is examined in detail by rewriting each term into a much simpler form as follows,

$$\frac{D}{Dt}\left(\frac{\overline{u_i'^2}}{2}\right) = \left(\frac{\partial}{\partial t} + \overline{\mathbf{u}}.\nabla\right)\frac{\overline{u_i'^2}}{2} = -(E_1 + E_4), \qquad \text{(A.29)}$$

$$-\frac{\partial}{\partial x_j}\left(\frac{1}{\rho_o}\overline{p'u_i'}\delta_{ij}\right) = E_3, \qquad -\frac{\partial}{\partial x_j}\overline{u_j'u_i'u_i'} = E_2, \qquad \frac{\partial}{\partial x_j}\left(\nu\frac{\partial}{\partial x_j}\frac{\overline{u_i'^2}}{2}\right) = E_6, \qquad \text{(A.30)}$$

and

$$-\overline{u_j'u_i'}\frac{\partial\overline{u_i}}{\partial x_j} = E_5, \qquad \nu\overline{\left(\frac{\partial u_i'}{\partial x_j}\right)^2} = \varepsilon, \qquad \overline{w'b'} = -B. \qquad \text{(A.31)}$$

After rearranging the terms in (A.28), along with the equations (A.29) through (A.31), (A.28) simply becomes

$$E = B + \varepsilon, \tag{A.32}$$

where $E = E_1 + E_2 + E_3 + E_4 + E_5 + E_6$ is the total mechanical energy required to maintain the turbulence, B is the buoyancy flux and ε is the turbulent dissipation rate.

Note that ε is always positive as viscous dissipation is present in a flow, and B can be either positive or negative, depending upon whether kinetic energy is lost or generated. As we are dealing with mixing where a net extraction of turbulent kinetic energy from the mean flow occurs and irreversibly increases the background potential energy of the density stratification, then B is, in a time-averaged sense, taken to be positive (although instantaneous values of B can be negative). Thus we can write

$$B = -\overline{w'b'} = \frac{g}{\rho_o}\overline{\rho' w'} > 0, \tag{A.33}$$

where ρ' is the density perturbation from its mean. Note, however, that because B represents the (reversible) buoyancy flux, great care must be taken in using B as a measure of irreversible mixing. Often both spatial integration over a fluid volume and temporal integration over the lifetime of a mixing event are required for this purpose.

Here we consider the mechanical energy balance in a stratified, turbulent shear flow assuming that the turbulence is stationary in the long term, time-averaged sense, i.e., $E_1 + E_4 = 0$. To simplify further we integrate E_2, E_3 and E_6 in (A.30) spatially over a closed control volume where there is no flux of fluid across the boundary. These terms make no contributions to the overall kinetic energy budget because they can only redistribute the turbulent energy within the control volume. Therefore the remaining terms from (A.32) are the shear production E_5, the buoyancy flux B and the rate of turbulent dissipation ε (Osborn, 1980). Hence, the simplified, steady-state energy balance can be written as

$$-\overline{u_i' w'}\frac{\partial \overline{u}_i}{\partial z} = \frac{g}{\rho_o}\overline{\rho' w'} + \varepsilon, \tag{A.34}$$

where ρ', u_i' $(i = 1, 2)$ and w' are the fluctuating components of the density, horizontal velocities and vertical velocity, respectively. If the reference density ρ_o is taken to be the mean density $\overline{\rho}$, then the expression in (A.34) is the same as in (2.1).

Appendix B

Pressure equalisation at mid-depth

Differences between the initial and final free surface heights of the fresh and saltwater reservoirs imply a net barotropic component to the flow, which may influence the exchange flow and associated mixing. In order to produce a purely baroclinic exchange, the initial free surface heights were adjusted to produce no net (barotropic) mass exchange between the reservoirs. This is to a good approximation equivalent to equalising pressures at mid-depth in the initial state. This appendix describes the procedure used to make this adjusment.

We write the differences in the free surface heights before and after the experiment as $\Delta_i = h_1 - h_2$ and $\Delta_f = h_1' - h_2'$, where i and f refer to the initial and final states, respectively. Here, h_1 and h_2 are the initial heights of the fresh and saltwater reservoirs, respectively, and h_1' and h_2' are the final heights of the fresh and saltwater reservoirs, respectively. Although these height differences (i.e., both Δ_i and Δ_f) are relatively small compared with the total water depth H, they affect the calculated value of mixing efficiency. We estimate the additional change in potential energy PE_{bar} associated with the barotropic component of the flow as

$$\begin{aligned} PE_{\text{bar}} &= \frac{1}{2} g A \rho_1 (\Delta_i^2 - \Delta_f^2) \\ &= \frac{1}{2} g A \rho_1 \left((h_1 - h_2)^2 - (h_1' - h_2')^2 \right), \end{aligned} \tag{B.1}$$

where g is acceleration due to gravity, A is the horizontal cross-sectional area of each reservoir and ρ_1 is the initial density of the freshwater reservoir. For a purely baroclinic exchange $PE_{\text{bar}} = 0$, or

$$h_1 - h_2 = h_1' - h_2'. \tag{B.2}$$

In solving (B.2) we refer to Figure B.1, where an 'intermediate' state (Figure B.1*a*)

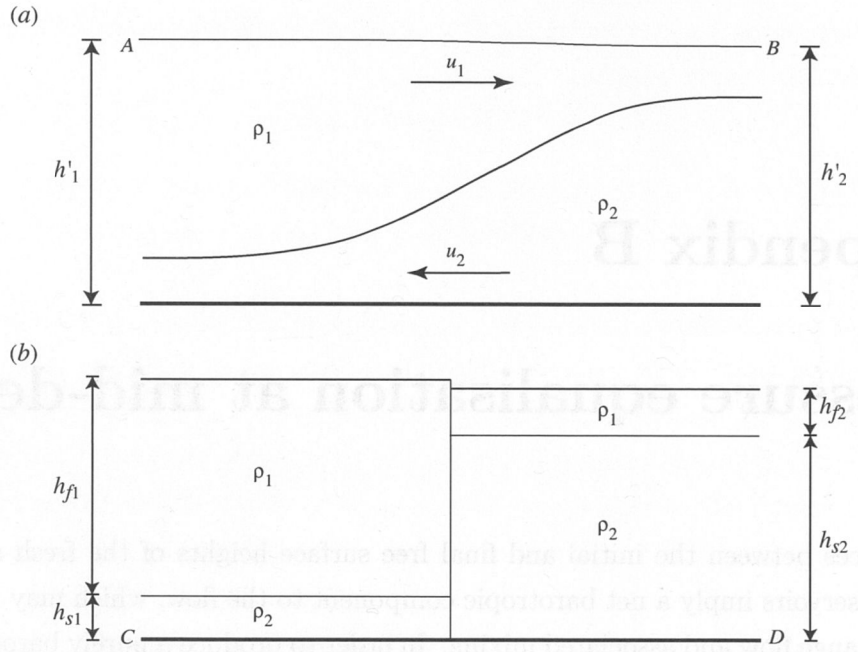

Figure B.1: Steady baroclinic exchange flow with (*a*) intermediate state and (*b*) hypothetical two-layer state.

is defined as a state at any time between the initial and final states. We consider a two-layer exchange flow with the less dense fluid flowing at the surface and the dense fluid flowing in the opposite direction along the base of the channel. The density and velocity of each layer are denoted by ρ_i and u_i, where $i = 1, 2$ refers to the upper layer and lower layer, respectively. We then assume that there are two points in the intermediate state: A and B, located near the surface (at the same height above the channel base), and the other two points in the hypothetical two-layer state: C and D at the bottom. These points are used to determine the horizontal pressure differences along the channel in steady baroclinic exchange, defined as the difference in pressures between the points on the left and those on the right.

The pressure difference at the surface Δp_t is due to the free surface height difference between A and B,

$$\Delta p_t = \rho_1 g(h'_1 - h'_2). \tag{B.3}$$

The pressure difference at the bottom Δp_b is determined by the hydrostatic pressure difference between C and D. For simplicity we evaluate this using the hypothetical two-layer state (assuming that the fluid is immiscible). Thus we can write

$$\Delta p_b = \rho_1 g h_{f1} + \rho_2 g h_{s1} - \rho_1 g h_{f2} - \rho_2 g h_{s2}, \tag{B.4}$$

where ρ_2 is the initial density of the saltwater reservoir, and h_{fi} and h_{si} $(i = 1, 2)$ are the depths of the fresh and saltwater layers, respectively (Figure B.1*b*). Assuming that top and bottom boundaries are stress-free and rigid, then the exchange is driven by the pressure differences on the top Δp_t and at the bottom $-\Delta p_b$. For a steady-state baroclinic exchange flow there must be a balance between these pressure differences such that $-\Delta p_b = \Delta p_t$, or

$$h_1' - h_2' = h_{f2} - h_{f1} + \frac{\rho_2}{\rho_1}(h_{s2} - h_{s1}). \tag{B.5}$$

Assuming that the flow is incompressible and that the Boussinesq approximation, hence volume conservation, holds, then (B.5) becomes

$$h_1' - h_2' = (h_2' - h_{s2}) - (h_1' - h_{s1}) + \left(1 + \frac{\Delta\rho}{\rho_1}\right)(h_{s2} - h_{s1}), \tag{B.6}$$

where $\Delta\rho/\rho_1 = (\rho_2 - \rho_1)/\rho_1$. Rearranging the terms in (B.6) gives us a simple expression for the height difference between the reservoirs,

$$h_1' - h_2' = \frac{\Delta\rho}{2\rho_1}(h_{s2} - h_{s1}). \tag{B.7}$$

The terms on the left-hand side of (B.7) are quantities we control. In order to solve this equation one of the two variables (i.e., h_{s1} or h_{s2}) must be eliminated. Assuming conservation of volume in (B.7) leads to

$$\begin{aligned} h_1' - h_2' &= \frac{\Delta\rho}{2\rho_1}(h_2' - h_{f2} - h_{s1}) \\ &= \frac{\Delta\rho}{2\rho_1}(h_2' - 2h_{s1}), \end{aligned} \tag{B.8}$$

where we have taken $h_{f2} = h_{s1}$ for simplicity. Note that in each experiment the total water depth H can be simply written as

$$H = \frac{1}{2}(h_1 + h_2) = \frac{1}{2}(h_1' + h_2'), \tag{B.9}$$

which gives us

$$H - h_2' = \frac{1}{2}(h_1' - h_2'). \tag{B.10}$$

We use (B.10) to quantify the height difference in the reservoirs by substituting

(B.10) into (B.8) to obtain

$$h_1' - h_2' = \frac{\Delta\rho}{2\rho_1}\left(H - \frac{1}{2}(h_1' - h_2') - 2h_{s1}\right), \tag{B.11}$$

from which, after rearranging the terms, we have

$$h_1' - h_2' = \frac{\Delta\rho/\rho_1(H - 2h_{s1})}{2 + 0.5\Delta\rho/\rho_1}. \tag{B.12}$$

The remaining unknown variable in the above equation is h_{s1}, which represents the hypothetical depth of the saltwater layer on the left reservoir and will be determined below.

We argue that the flow is marginally stable to shear so that, in a time-averaged sense, the gradient Richardson number Ri_g (defined as δ/H in 4.20) is characterised by the critical Richardson number $Ri_{\text{crit}} = 0.25$ (Howard, 1961; Miles, 1961). Thus $\delta/H \approx 0.25$ for this flow. Using this value and following the methods used by Hogg *et al.* (2001*a*) we can write the normalised volume transport Q owing to mixing and friction for flows through a simple contraction as

$$\begin{aligned} Q &= 1 - \delta/2H - Q_{\text{fri}} \\ &\approx 0.875 - Q_{\text{fri}}. \end{aligned} \tag{B.13}$$

If frictional effects are negligible but mixing is still present, then volume transport Q_i ($i = 1, 2$) in each layer for the baroclinic exchange is

$$Q_i \approx \frac{0.875 b_o g'^{1/2} H^{3/2}}{4}, \tag{B.14}$$

where we have invoked Q_i as the product of Q (with Q_{fri} on the right-hand side of B.13 being set to zero) and $Q_{\max} = 1/4 b_o g'^{1/2} H^{3/2}$ as the maximal volume transport predicted by the inviscid, two-layer hydraulic theory (2.22). The above equation is useful for estimating h_{s1} as

$$\begin{aligned} h_{s1} &= \frac{Q_i t_r}{A} \\ &\approx \frac{0.875 b_o g'^{1/2} H^{3/2} t_r}{4A}, \end{aligned} \tag{B.15}$$

where t_r is the experimental run time. Note that h_{s1} in (B.15) depends upon the external parameters that include the constriction minimum width b_o, the density difference $\Delta\rho$ (as implied by the reduced gravity g'), the full water depth H and the

run time t_r. We estimate this run time by dividing the half-length $L/2$ of the tank by the flow speed U, defined as $U = 0.5(g'H)^{1/2}$ in each experiment.

The difference in the heights between the left and right reservoirs can be obtained by substituting (B.15) into (B.12),

$$h_1' - h_2' = h_1 - h_2 = \frac{\Delta\rho/\rho_1 \left(H - 0.875 b_o g'^{1/2} H^{3/2} t_r/2A\right)}{2 + 0.5\Delta\rho/\rho_1}, \tag{B.16}$$

which we use as the initial condition for equalising pressures in the reservoirs at approximately mid-depth. Whereas (B.16) was utilised in each run to calculate the required height difference, we note that for typical flow conditions in the present experiments the initial height difference, $h_1 - h_2$, can be approximated by $H\Delta\rho/2\rho_1$ to within 17%.

Appendix C

Calibration of the density meter

An Anton Paar digital density meter (DMA 60) was used to measure the density of samples taken from early experiments to an accuracy of ± 0.01 kgm^{-3}. This instrument determines the density of an approximately 1 ml sample by measuring the natural period of oscillation of a quartz glass U-tube containing the sample. To minimise systematic errors, the DMA 60 was frequently calibrated using the following procedure.

First, the oscillation period T_a for room air was found. The density ρ_a of room air at the time of measurement can be written as

$$\rho_a = 0.004635 \times (p - 0.3783 \times \mathcal{R} \times \mathcal{P})/(T_c + 272.47956), \tag{C.1}$$

where p is the barometric pressure (in cmHg), $\mathcal{R}$ is the relative humidity at room temperature, $\mathcal{P}$ is the saturation vapour pressure for water at room temperature (in cmHg) and T_c is the cell temperature (in °C). Second, the oscillation period T_w for distilled water at 20°C was measured. The calibration constant K for the DMA 60 could then be calculated as

$$K = (\rho_w - \rho_a)/(T_w^2 - T_a^2), \tag{C.2}$$

where ρ_w is the density of water at 20°C, taken to be 998.234 kgm^{-3}. This calibration constant K can be used to calculate the density ρ of a sample from a measurement of the oscillation period T_s, according to the formula

$$\rho = \rho_w + K(T_s^2 - T_w^2). \tag{C.3}$$

At a later stage of the project an Anton Paar DMA 5000 density meter was used to measure the densities to a precision of ± 0.005 kgm^{-3}. The DMA 5000 instrument

was self-calibrating. To ensure conformity the DMA 5000 was used together with the DMA 60 in a number of experiments (i.e., H9, J5, J6, K5, K6, K7 and K8). It was found that both density meters provided consistent results.

Bibliography

ANATI, D. A., ASSAF, G. & THOMPSON, R. O. R. Y. 1977 Laboratory models of sea straits. *J. Fluid Mech.* **81**, 341–351.

ARMI, L. 1986 The hydraulics of two flowing layers with different densities. *J. Fluid Mech.* **163**, 27–58.

ARMI, L. & FARMER, D. 1988 The flow of Mediterranean Water through the Strait of Gibraltar. *Prog. Oceanogr.* **21**, 1–105.

ARMI, L. & FARMER, D. M. 1986 Maximal two-layer exchange through a contraction with barotropic net flow. *J. Fluid Mech.* **164**, 27–51.

ARMI, L. & FARMER, D. M. 1987 A generalization of the concept of maximal exchange in a strait. *J. Geophys. Res.* **92**, 14679–14680.

ARNEBORG, L. 2002 Mixing efficiencies in patch turbulence. *J. Phys. Oceanogr.* **32**, 1496–1506.

BENJAMIN, T. B. 1968 Gravity currents and related phenomena. *J. Fluid Mech.* **31**, 209–248.

BORMANS, M. & GARRET, C. 1989 The effects of non-rectangular cross section, friction, and barotropic fluctuations on the exchange through the Strait of Gibraltar. *J. Phys. Oceanogr.* **19**, 1543–1557.

BRAY, N., OCHOA, W. J. & KINDER, T. 1995 The role of the interface in exchange through the Strait of Gibraltar. *J. Geophys. Res.* **100**, 10755–10776.

BRYDEN, H. L. & NURSER, A. J. G. 2003 Effects of strait mixing on ocean stratification. *J. Phys. Oceanogr.* **33**, 1870–1872.

BRYDEN, H. L. & STOMMEL, H. M. 1984 Limiting processes that determine basic features of the circulation in the Mediterranean Seas. *Ocean. Acta* **7**, 289–296.

CARPENTER, J. R., LAWRENCE, G. A. & SMYTH, W. D. 2007 Evolution and mixing of asymmetric Holmboe instabilities. *J. Fluid Mech.* **582**, 103–132.

CAULFIELD, C. P. & PELTIER, W. R. 2000 The anatomy of the mixing transition in homogeneous and stratified free shear layers. *J. Fluid Mech.* **413**, 1–47.

CUSHMAN-ROISIN, B. 1994 *Introduction to Geophysical Fluid Dynamics*. Englewood Cliffs, NJ: Prentice Hall.

DALZIEL, S. B. 1991 Two layer hydraulics: a functional approach. *J. Fluid Mech.* **223**, 135–163.

DALZIEL, S. B. 1992 Maximal exchange in channels with non-rectangular cross sections. *J. Phys. Oceanogr.* **22**, 1188–1206.

DALZIEL, S. B. 1993 Rayleigh-Taylor instability: experiments with image analysis. *Dyn. Atmos. Ocean.* **20**, 127–153.

DALZIEL, S. B. & LANE-SERFF, G. F. 1991 The hydraulics of doorway exchange flows. *Bldg. Environ.* **26**, 121–135.

DALZIEL, S. B., LINDEN, P. F. & YOUNGS, D. L. 1999 Self-similarity and internal structure of turbulence induced by Rayleigh-Taylor instability. *J. Fluid Mech.* **399**, 1–48.

DICKSON, R. R. & BROWN, J. 1994 The production of North Atlantic Deep Waters: sources, rates and pathways. *J. Geophys. Res.* **99**, 12319–12341.

DUNCAN, L. M., BRYDEN, H. L. & CUNNINGHAM, S. A. 2003 Friction and mixing in the Faroe Bank Channel outflow. *Ocean. Acta* **26**, 473–486.

ELLISON, T. H. 1957 Turbulent transport of heat and momentum from an infinite rough plane. *J. Fluid Mech.* **2**, 456–466.

FARMER, D. & ARMI, L. 1988 The flow of Atlantic Water through the Strait of Gibraltar. *Prog. Oceanogr.* **21**, 1–105.

FARMER, D. M. & ARMI, L. 1986 Maximal two-layer exchange flow over a sill and through the combination of a sill and contraction with barotropic flow. *J. Fluid Mech.* **164**, 53–76.

FERNANDO, H. J. S. 1991 Turbulent mixing in stratified fluids. *Ann. Rev. Fluid Mech.* **23**, 455–493.

FERNANDO, H. J. S. & HUNT, J. C. R. 1996 Some aspects of turbulence and mixing in stably stratified layers. *Dyn. Atmos. Ocean.* **23**, 35–62.

FINNIGAN, T. D. & IVEY, G. N. 2000 Convectively driven exchange flow in a stratified sill-enclosed basin. *J. Fluid Mech.* **418**, 313–338.

GANACHAUD, A. & WUNSCH, C. 2000 Improved estimates of global ocean circulation, heat transport and mixing from hydrographic data transport. *Nature* **408**, 453–457.

GARCÍA, M. H. & PARSONS, J. D. 1996 Mixing at the front of gravity currents. *Dyn. Atmos. Ocean.* **24**, 197–205.

GARGETT, A. E. & MOUM, J. N. 1995 Mixing efficiencies in turbulent tidal fronts: results from direct and indirect measurements of density flux. *J. Phys. Oceanogr.* **25**, 2583–2608.

GERDES, F., GARRET, C. & FARMER, D. 2002 On internal hydraulics with entrainment. *J. Phys. Oceanogr.* **32**, 1106–1111.

GORDON, A. R., GIULIVI, C. F. & ILAHUDE, A. G. 2003 Deep topographic barriers within the Indonesian seas. *Deep-Sea Res. II* **50**, 2205–2228.

GRECO, S. L. 1998 Two-layer exchange flow through the Burlington Ship Canal. Master's thesis, University of British Columbia.

GREGG, M. C. 1989 Scaling turbulent dissipation in the thermocline. *J. Geophys. Res.* **94**, 9686–9698.

GREGG, M. C. & ÖZSOY, E. 2002 Flow, water mass changes, and hydraulics in the Bosphorus. *J. Geophys. Res.* **107**, 10.1029/2000JC000485.

GREGG, M. C., ÖZSOY, E. & LATIF, M. A. 1999 Quasi-steady exchange flow in the Bosphorus. *Geophys. Res. Lett.* **26**, 83–86.

GRIGG, N. J. & IVEY, G. N. 1997 A laboratory investigation into shear-generated mixing in a salt wedge estuary. *Geophys. Astrophys. Fluid Dyn.* **85**, 65–95.

GRIMM, T. & MAXWORTHY, T. 1999 Buoyancy-driven mean flow in a long channel with a hydraulically constrained exit condition. *J. Fluid Mech.* **398**, 155–180.

GU, L. 2001 Frictional exchange flow through a wide channel with application to the Burlington Ship Canal. PhD thesis, University of British Columbia.

GU, L. & LAWRENCE, G. A. 2005 Analytical solution for maximal frictional two-layer exchange flow. *J. Fluid Mech.* **543**, 1–17.

HACKER, J., LINDEN, P. F. & DALZIEL, S. B. 1996 Mixing in lock release gravity currents. *Dyn. Atmos. Ocean.* **24**, 183–195.

HALLWORTH, M. A., PHILIPS, J. C., HUPPERT, H. E. & SPARKS, R. S. J. 1993 Entrainment in turbulent gravity currents. *Nature* **362**, 829–831.

HÄRTEL, C., MEIBURG, E. & NECKER, F. 2000 Analysis and direct numerical simulation of the flow at a gravity-current head: Part 1. flow topology and front speed for slip and no-slip boundaries. *J. Fluid Mech.* **418**, 189–212.

HELFRICH, K. L. 1995 Time-dependent two-layer hydraulic exchange flow. *J. Phys. Oceanogr.* **25**, 359–373.

HOGG, A. M., IVEY, G. N. & WINTERS, K. B. 2001*a* Hydraulics and mixing in controlled exchange flows. *J. Geophys. Res.* **106**, 959–972.

HOGG, A. M., WINTERS, K. B. & IVEY, G. N. 2001*b* Linear internal waves and the control of stratified exchange flows. *J. Fluid Mech.* **447**, 357–375.

HOGG, N., BISCAYE, P., GARDNER, W. & SCHMIDTZ, W. J. 1982 On the transport and modification of Antarctic Bottom Water in the Vema Channel. *J. Mar. Res.* **40**, 231–263.

HOLFORD, J. M. & LINDEN, P. F. 1999 Turbulent mixing in a stratified fluid. *Dyn. Atmos. Ocean.* **30**, 173–198.

HOWARD, L. N. 1961 Note on a paper of John W. Miles. *J. Fluid Mech.* **10**, 509–512.

HUNKINS, K. & WHITEHEAD, J. A. 1992 Laboratory simulation of exchange through Fram Strait. *J. Geophys. Res.* **97**, 11299–11321.

HUNT, G. R. & LINDEN, P. F. 1999 The fluid mechanics of natural ventilation – displacement ventilation by buoyancy-driven flows assisted by wind. *Bldg. Environ.* **34**, 707–720.

IMBERGER, J. & IVEY, G. N. 1991 On the nature of turbulence in a stratified fluid. Part 2: application to lakes. *J. Phys. Oceanogr.* **21**, 659–680.

ITSWEIRE, E. C., KOSEFF, J. R., BRIGGS, D. A. & FERZIGER, J. H. 1993 Turbulence in stratified shear flows: implications for interpreting shear-induced mixing in the ocean. *J. Phys. Oceanogr.* **23**, 1508–1522.

IVEY, G. N. 2004 Stratification and mixing in sea straits. *Deep-Sea Res. II* **51**, 441–453.

IVEY, G. N. & IMBERGER, J. 1991 On the nature of turbulence in a stratified fluid. Part I: energetics of mixing. *J. Phys. Oceanogr.* **21**, 650–658.

IVEY, G. N. & NOKES, R. I. 1989 Vertical mixing due to the breaking of critical internal waves on sloping boundaries. *J. Fluid Mech.* **204**, 479–500.

KOOP, C. G. & BROWAND, F. K. 1979 Instability and turbulence in a stratified fluid. *J. Fluid Mech.* **93**, 135–160.

KÖSTERS, F., KÄSSE, R. H., SCHMITTNER, A. & HERRMANN, P. 2005 The effect of Denmark Strait overflow on the Atlantic Meridional Overturning Circulation. *Geophys. Res. Lett.* **32**, LO4602.

KUNZE, E. & SANFORD, T. B. 1996 Abyssal mixing: where it is not. *J. Phys. Oceanogr.* **26**, 2286–2296.

LAWRENCE, G. A. 1990 On the hydraulics of Boussinesq and non-Boussinesq two-layer flows. *J. Fluid Mech.* **215**, 457–480.

LAWRENCE, G. A. 1993 The hydraulics of steady two-layer flow over a fixed obstacle. *J. Fluid Mech.* **254**, 605–633.

LEDWELL, J. R., MONTGOMERY, E. T., POLZIN, K. L., ST. LAURENT, L. C., SCHMITT, R. W. & TOOLE, J. M. 2000 Evidence for enhanced mixing over rough topography in the abyssal ocean. *Nature* **403**, 179–182.

LEDWELL, J. R., WATSON, A. J. & LAW, C. S. 1993 Evidence for slow mixing across the pycnocline from an open-ocean tracer release experiment. *Nature* **364**, 701–703.

LEDWELL, J. R., WATSON, A. J. & LAW, C. S. 1998 Mixing of a tracer in the pycnocline. *J. Geophys. Res.* **103**, 21499–21529.

LIN, Y. J. P. & LINDEN, P. F. 2002 Buoyancy-driven ventilation between two chambers. *J. Fluid Mech.* **463**, 293–312.

LINDEN, P. F. 1979 Mixing in stratified fluids. *Geophys. Astrophys. Fluid Dyn.* **13**, 3–23.

LINDEN, P. F. 1980 Mixing across a density interface produced by grid turbulence. *J. Fluid Mech.* **100**, 691–703.

LINDEN, P. F. 1999 The fluid mechanics of natural ventilation. *Ann. Rev. Fluid Mech.* **31**, 201–238.

LONG, R. R. 1956 Long waves in a two fluid system. *J. Meteorol.* **13**.

LOWE, R. J., LINDEN, P. F. & ROTMAN, J. W. 2002 Mixing in lock release gravity currents. *J. Fluid Mech.* **456**, 33–48.

MARINO, B. M., THOMAS, L. P. & LINDEN, P. F. 2005 The front conditions for gravity currents. *J. Fluid Mech.* **536**, 49–78.

MCDONAGH, E. L., ARHAN, M. & HEYWOOD, K. J. 2002 On the circulation of bottom water in the region of Vema Channel. *Deep-Sea Res. I* **49**, 1119–1139.

MCEWAN, A. 1983 Internal mixing in stratified fluids. *J. Fluid Mech.* **128**, 59–80.

MILES, J. W. 1961 On the stability of heterogeneous shear flows. *J. Fluid Mech.* **10**, 496–508.

MONTI, P., QUERZOLI, G., CENEDESE, A. & PICCININI, S. 2007 Mixing properties of a stably stratified parallel shear layer. *Phys. Fluids* **19**, 085104.

MOUM, J. N. 1996 Efficiency of mixing in the main thermocline. *J. Geophys. Res.* **101**, 12057–12069.

MUNCHOW, A. & GARVINE, R. W. 1993 Dynamical properties of a buoyancy-driven coastal current. *J. Geophys. Res.* **98**, 20063–20077.

MUNK, W. & WUNSCH, C. 1998 Abyssal recipes II: energetics of tidal and wind mixing. *Deep-Sea Res. I* **45**, 1977–2010.

MUNK, W. H. 1966 Abyssal recipes. *Deep-Sea Res.* **13**, 707–730.

MURRAY, S. P. & JOHN, W. 1997 Direct observation of seasonal exchange through the Bab el Mandab Strait. *Geophys. Res. Lett.* **24**, 2557–2560.

OĞUZ, T. 2005 Hydraulic adjusments of the Bosphorus exchange flow. *Geophys. Res. Lett.* **32**, 10.1029/2005GL022353.

OĞUZ, T., ÖZSOY, E., LATIF, M. A., SUR, H. I. & ÜNLÜATA, U. 1990 Modeling of hydraulically controlled exchange flow in the Bosphorus Strait. *J. Phys. Oceanogr.* **20**, 945–965.

OSBORN, T. R. 1980 Estimates of the local rate of vertical diffusion from dissipation measurements. *J. Phys. Oceanogr.* **10**, 83–89.

PARK, Y. G., WHITEHEAD, J. A. & GNANADESIKAN, A. 1994 Turbulent mixing in stratified fluids: layer formation and energetics. *J. Fluid Mech.* **279**, 279–311.

PATTERSON, M. D., CAULFIELD, C. P., MCELWAINE, J. N. & DALZIEL, S. B. 2006 Time dependent mixing in stratified Kelvin-Helmholtz billows: experimental observations. *Geophys. Res. Lett.* **33**, L15608.

PELTIER, W. R. & CAULFIELD, C. P. 2003 Mixing efficiency in stratified shear flows. *Ann. Rev. Fluid Mech.* **35**, 135–167.

POLZIN, K. L., TOOLE, J. M., LEDWELL, J. R. & SCHMIDT, R. W. 1997 Spatial variability of turbulent mixing in the abyssal ocean. *Science* **276**, 93–96.

PRANDTL, L. 1952 *Essentials of Fluid Dynamics*. Blackie and Sons.

PRATT, L. J. 1986 Hydraulic control of sill flow with bottom friction. *J. Phys. Oceanogr.* **16**, 1970–1980.

PRATT, L. J., JOHNS, W., MURRAY, S. P. & KATSUMATA, K. 1999 Hydraulic interpretation of direct velocity measurements in the Bab al Mandab. *J. Phys. Oceanogr.* **29**, 2769–2784.

PRATT, L. J. & LUNDBERG, P. A. 1991 Hydraulics of rotating strait and sill flow. *Ann. Rev. Fluid Mech.* **23**, 81–106.

REDONDO, J. M., SANCHEZ, M. A. & CANTALAPIEDRA, I. R. 1996 Turbulent mechanism in stratified fluids. *Dyn. Atmos. Ocean.* **24**, 107–115.

ROHR, J. J., ITSWEIRE, E. C. & ATTA, C. W. 1984 Mixing efficiency in stably stratified decaying turbulence. *Geophys. Astrophys. Fluid Dyn.* **29**, 221–236.

RUDDICK, B., WALSH, D. & OAKEY, N. 1997 Variations in apparent mixing efficiency in the North Atlantic Central Water. *J. Phys. Oceanogr.* **27**, 2589–2605.

RUDDICK, B. R. & SHIRTCLIFFE, T. G. L. 1979 Data for double diffusers: physical properties of aqueous salt-sugar solutions. *Deep-Sea Res.* **26**, 775–787.

SHERMAN, F. S., IMBERGER, J. & CORCOS, G. M. 1978 Turbulence and mixing in stably stratified waters. *Ann. Rev. Fluid Mech.* **10**, 267–288.

SHIN, J. O., DALZIEL, S. B. & LINDEN, P. F. 2004 Gravity currents produced by lock exchange. *J. Fluid Mech.* **521**, 1–34.

SIMPSON, J. E. 1997 *Gravity currents in the environment and the laboratory*. Cambridge University Press.

SMEED, D. A. 2000 Hydraulic control of three-layer exchange flows: application to Bab al Mandab. *J. Phys. Oceanogr.* **30**, 2574–2588.

SMEED, D. A. 2004 Exchange through the Bab el Mandab. *Deep-Sea Res. II* **51**, 455–474.

SMYTH, W. D., CARPENTER, J. R. & LAWRENCE, G. A. 2007 Mixing in symmetric Holmboe waves. *J. Phys. Oceanogr.* **37**, 1566–1583.

ST. LAURENT, L. & SIMMONS, H. 2006 Estimates of power consumed by mixing in the ocean interior. *J. Climate* **19**, 4877–4890.

STAQUET, C. 2000 Mixing in a stably stratified shear layer: two- and three dimensional numerical experiments. *Fluid Dyn. Res.* **27**, 367–404.

STENSTRÖM, P. 2003 Mixing and recirculation in two-layer exchange flows. *J. Geophys. Res.* **108**, 10.1029/2002JC001696.

STIGEBRAND, A. & AURE, J. 1989 On vertical mixing in the basin waters of fjords. *J. Phys. Oceanogr.* **19**, 917–926.

STOMMEL, H. & FARMER, H. 1953 Control of salinity in an estuary by a transition. *J. Mar. Res.* **12**, 13–20.

STRANG, E. J. & FERNANDO, H. J. S. 2001*a* Entrainment and mixing in stratified shear flows. *J. Fluid Mech.* **428**, 349–386.

STRANG, E. J. & FERNANDO, H. J. S. 2001*b* Vertical mixing and transports through a stratified shear layer. *J. Phys. Oceanogr.* **31**, 2026–2048.

TEDFORD, E. W. 1999 Exchange flow through the Burlington Ship Canal. Master's thesis, University of British Columbia.

TENNEKES, H. & LUMLEY, J. L. 1972 *A First Course in Turbulence*. The MIT Press.

THORPE, S. A. 1968 A method of producing a shear flow in a stratified fluid. *J. Fluid Mech.* **32**, 693–704.

THORPE, S. A. 1973 Experiments on instability and turbulence in a stratified shear flow. *J. Fluid Mech.* **61**, 731–751.

TSIMPLIS, M. N. & BRYDEN, H. L. 2000 Estimation of the transports through the Strait of Gibraltar. *Deep-Sea Res. I* **47**, 2219–2242.

TURNER, J. S. 1973 *Buoyancy Effects in Fluids*. Cambridge University Press.

VRANES, K., GORDON, A. L. & FIELD, A. 2002 The heat transport of the Indonesian Throughflow and implications for the Indian Ocean heat budget. *Deep-Sea Res. II* **49**, 1391–1410.

WANG, D.-P. 1984 Mutual intrusion of a gravity current and density front. *J. Phys. Oceanogr.* **14**, 1191–1199.

WEBB, D. J. & SUGINOHARA, N. 2001 Vertical mixing in the ocean. *Nature* **409**, 37.

WHITEHEAD, J. A. 1998 Topographic control of oceanic flows in deep passages and straits. *Rev. Geophys.* **36**, 423–440.

WHITEHEAD, J. A., LEETMAA, A. & KNOX, R. A. 1974 Rotating hydraulics of strait and sill flows. *Geophys. Fluid Dyn.* **6**, 101–125.

WHITEHEAD, J. A. & WORTHINGTON, L. V. 1982 The flux and mixing rates of Antarctic Bottom Water within the North Atlantic. *J. Geophys. Res.* **87**, 7903–7924.

WINTERS, K. B., LOMBARD, P. N., RILEY, J. J. & D'ASARO, E. A. 1995 Available potential energy and mixing in density-stratified fluis. *J. Fluid Mech.* **289**, 115–128.

WINTERS, K. B. & SEIM, H. E. 2000 The role of dissipation and mixing in exchange flow through a contracting channel. *J. Fluid Mech.* **407**, 265–290.

WOOD, I. R. 1970 A lock exchange flow. *J. Fluid Mech.* **42**, 671–687.

WUNSCH, C. 2002 What is the thermohaline circulation? *Science* **298**, 1179–1181.

WUNSCH, C. & FERRARI, R. 2004 Vertical mixing, energy, and the general circulation of the oceans. *Ann. Rev. Fluid Mech.* **36**, 281–314.

ZHU, D. Z. & LAWRENCE, G. A. 2000 Hydraulics of exchange flows. *J. Hydr. Eng.* **126**, 921–928.

ZHU, Z. & LAWRENCE, G. A. 1998 Non-hydrostatic effects in layered shallow water flows. *J. Fluid Mech.* **355**, 1–16.